Spectroscopic and Spectropolarimetric Insights into Reconnection Dynamics in Solar Flares

Ryan James French

A dissertation submitted in partial fulfillment

of the requirements for the degree of

Doctor of Philosophy

of

University College London.

Department of Space & Climate Physics

University College London

July 7, 2022

I, Ryan James French, confirm that the work presented in this thesis is my own. Where information has been derived from other sources, I confirm that this has been indicated in the work.

Abstract

Solar flares are one of the most energetic events in the solar system, created by the explosive conversion of magnetic free energy into particle acceleration, plasma heating and EM radiation through the process of magnetic reconnection. It is believed that in solar flares, magnetic reconnection occurs within a current sheet between converging oppositely-orientated magnetic fields – but the nature of reconnection and exact mechanisms behind the release and transport of energy within flares are still uncertain.

Current sheets are notoriously difficult to observe, primarily due to their small thickness (below current observable limits of instrumentation). Sometimes, hot plasma sheets can be seen along suspected current sheet regions during off-limb flares, but such events are uncommon and rarely caught in spectroscopic observations. One such X-class flare occurred on the 10th September 2017. In the first two science chapters of this thesis, a range of space and ground-based instrumentation are used to study the nature of reconnection dynamics in this 10th September 2017 event. Primarily, we compare infrared linear polarisation data from the Coronal Multi-channel Polarimeter instrument with simple empirical models, to find evidence for magnetic structure on sub-pixel scales. The results are compatible with the 'tearing mode instability' model of reconnection. Taking this analysis further, we use extreme-ultraviolet spectroscopy with the Hinode Extreme-Ultraviolet Imaging Spectrometer (and other supporting instruments) to explore the long duration over which reconnection and energy release persists in this event.

However, we cannot always rely on rare off-limb events to further our knowledge of flare reconnection dynamics. In the third science chapter, Fast Fourier

Transforms along flare ribbons of a small flare reveal insight into the growth of spatial scales in the current sheet region. This method reveals further evidence for the tearing mode instability triggering plasma turbulence at the onset of reconnection.

Although reconnecting current sheet regions are elusive, the work in this thesis develops novel techniques to probe the nature of magnetic processes within these crucial regions. The methodology used in this thesis can be pushed further, as observations from next-generation instrumentation start to become available.

Impact Statement

Magnetic reconnection is a fundamental process in plasma physics, occurring within a huge range of exotic astrophysical environments. At the Sun, we have the privilege of remotely observing these explosive high energy events with a far greater spatial resolution than elsewhere in the universe. Therefore, by studying the nature of explosive energy release in the solar environment, we are also revealing insight into this universal plasma process on wider scales.

But at the Sun in particular, understanding the processes leading to the onset of explosive events is particularly important. In 2011, *Space Weather* was added to the UK National Risk Register, as it was formally recognised by government bodies that activity on the Sun could cause economic and technological damage here on Earth. In order to fully mitigate and forecast the largest space weather events, such as those associated with solar flares, we must first understand the processes leading to their formation.

The work in this thesis investigates the nature of this fundamental magnetic reconnection process, the primary driver of explosive energy release in flares. The methodology used within this work is also relevant to studies with the newly-operational Daniel K. Inouye Solar Telescope (DKIST).

List of Publications

- **Ryan J. French**, Roberto Casini, Philip Judge, Thomas Bogdan, Alfred de Wijn. First Observation of Chromospheric Waves in a Sunspot by DKIST/ViSP. *In Prep*
- **Ryan J. French**, Sarah A. Matthews, I. Jonathan Rae, Andrew W. Smith. Probing Current Sheet Instabilities from Flare Ribbon Dynamics. *Astrophys. J.*, 922:117, Nov 2021. doi: 10.3847/1538-4357/ac256f
- D. Stansby, L. Berčič, L. Matteini, C. J. Owen, **R. French**, D. Baker and S. Badman. Sensitivity of solar wind mass flux to coronal temperature. *Astron. Astrophys.*, 650:L2, June 2021. doi: 10.1051/0004-6361/202039789
- **Ryan J. French**, Sarah A. Matthews, Lidia van Driel-Gesztelyi, David M. Long, and Philip G. Judge. Dynamics of Late-stage Reconnection in the 2017 Sept 10 Solar Flare. *Astrophys. J.*, 900(2):192, September 2020. doi: 10.3847/1538-4357/aba94b
- **Ryan J. French**, Philip G. Judge, Sarah A. Matthews, and Lidia van Driel-Gesztelyi. Spectropolarimetric Insight into Plasma Sheet Dynamics of a Solar Flare. *Astrophys. J. Lett.*, 887(2):L34, Dec 2019. doi: 10.3847/2041-8213/ab5d34

Additional unrefereed articles

- **Ryan French**, Alexander James, Deborah Baker, Sarah Matthews, William Dunn & St Wilfrid's Catholic School students. Opening Pupil's Eyes to the Sun. *A&G*. Dec 2020. doi: 10.1093/astrogeo/ataa085

Acknowledgements

Thank you to my PhD examiners, Prof. Graziella Branduardi-Raymont and Dr. Natasha Jeffrey, for taking the time to read this thesis.

I thank the STFC for support via funding from my PhD Studentship, ST/S50578X/1. Furthermore, I thank the NCAR High Altitude Observatory for supporting two productive trips to Boulder, Colorado, through my Newkirk Fellowship.

Firstly, I would like to thank my PhD supervisors Prof. Sarah Matthews and Prof. Lidia van Driel-Gesztelyi for their support, encouragement, and wisdom of the Sun. No matter how last-minute I left things – you were always there to help. Thanks too to Dr. Philip Judge at the High Altitude Observatory for your belief in me, and for the stream of advice on what makes a good scientist. In addition to Phil, I'd also like to thank Dr. Roberto Casini and Dr. Thomas Bogdan for their scientific support during my recent trip to Boulder – I look forward to the world seeing our exciting science. I'd also like to thank the rest of my scientific collaborators: Dr. David Stansby, Dr. David Long, Prof. Jonathan Rae and Dr. Andy Smith.

Back at MSSL, I'd like to thank ex-fellow students Dr. Alex James, Dr. Jack Jenkins and Dr. Jennifer O'kane, for welcoming me so warmly into the G01 student office. Although our time together in G01 (pre-lockdown) was relatively short, I feel I have made some friends for life. I also need to thank the rest of the MSSL Solar Group (past and present) for all the valuable advice and scientific discussion, including Dr. Deborah Baker, Dr. Hamish Reid, Dr. Stephanie Yardley and Dr. Gherardo Valori. And to Prof. Lucie Green - who convinced me to apply for a PhD at UCL, whilst on a train down to Exeter (we missed our stop). Thanks to the newer

members of G01 too, it's a shame we couldn't spend more time in G01 together. Thank you also to my good friend and ex-housemate Richard Haythornthwaite, for all the science and sanity-saving chats during the first 2020 lockdowns.

Before the start of my PhD, my interest in the Sun was first heightened during a Summer Placement at the Met Office Space Weather Operations Centre. Thank you to Mark Gibbs, Catherine Burnett and Caroline Patterson for first sparking the start of my solar journey during that time.

And finally, a massive thank you to my fiancé Georgie Getley, for your endless support and encouragement across my PhD, and for agreeing so enthusiastically to move across the world with me for my first postdoc. I couldn't have done this without you. I look forward to our wedding, one week after my PhD viva!

Contents

List of Figures

List of Tables

Chapter 1

Introductory Material

1.1 The Sun - an Ordinary Star?

Sitting above our heads on a sunny day, it is easy to consider the Sun as 'ordinary'. But, unbeknownst to the unaided human eye, and despite its seemingly-unchanging appearance in the sky above us, the Sun is incredibly dynamic, with an atmosphere continuously evolving over timescales from seconds to beyond centuries. Despite this, some may argue that these processes fail to make the Sun any less ordinary at all, for the physical processes determining the behaviour of our own Sun, do so also on 250 billion other stars in our galaxy alone. To those who argue this point, I respectfully disagree. Although it is true that the Sun holds an insignificant place in a spiral arm of the Milky Way galaxy, it holds a far more special place for us. For, unlike the thousands of point source stars above us on a clear, dark night - the Sun is *our* star, a beacon of warmth and light across the eons of humanity's evolution. Across the history of human civilisation, ancient cultures have recognised this critical role the Sun plays, often hailing it as a god or deity as a result. In a way, these were the first solar physicists – explaining the observed behaviour of the Sun with the tools and knowledge available to them at the time. Evidently, our collective knowledge of the Sun has evolved significantly over the millennia, and solar physicists today have access to a wide range of telescopes, heliospheric spacecraft and computing power, the likes of which our scientific predecessors could not have imagined even a hundred years ago.

At a mean distance of 149.6 million km from Earth with a radius of 695,500 km ($1R_{\odot}$), we observe the Sun with an angular diameter of $\approx 1900''$, making it the most resolved star in the sky by several orders of magnitude. Therefore, by using the tools available to us to study the behaviour of our own star, our Sun acts as a local astrophysical and plasma-physics laboratory, also contributing to the greater understanding of the universal and fundamental physics of magnetised environments throughout our galaxy and beyond.

In this introduction, I first introduce the relevant plasma and MHD physics, before including these processes in the context of the solar atmosphere and solar flares.

1.2 Some Key Physics Concepts

1.2.1 Plasma

As a child in school (at least in the UK National Curriculum), you are taught about the *Three States of Matter* – solid, liquid and gas. However, these categories exclude some $> 99.9\%$ of the observable universe. For stars, solar/stellar winds and interstellar (even intergalactic) space are made up of the fourth state of matter – **plasma**. Just like the transitions from solid to liquid to gas, plasma is created by energising a neutral gas, to the point where bound electrons escape from the atom. This creates a medium of free electrons and ions, which, despite the charged nature of its components, is neutral on large scales. Hydrogen, with one electron and one proton, becomes fully ionised after one of these transitions. Heavier elements, however, have many more electrons to lose. Take for example, an Fe atom, with 26 bound electrons. This is the neutral, first version of Fe, which we can denote Fe I. As the atom gains energy and loses its first electron, it becomes the singly-ionised Fe II. This is followed by Fe III after the next electron loss, all the way to a fully ionised Fe XXVII ion with no bound electrons. Similarly, if energy were removed from the system, recombination would occur as ions capture free electrons.

Due to the fact that progressively higher ions are formed at increasing energies, an individual ion species can therefore only exist in a specific range of local ther-

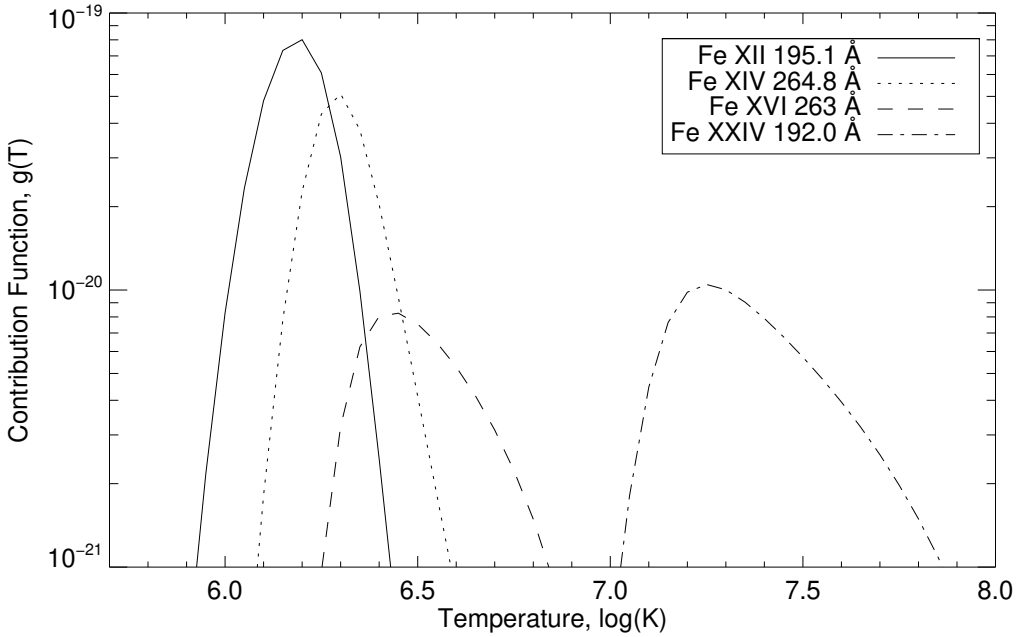

Figure 1.1: Contribution functions of example Fe XII, Fe XIV, Fe XVI and Fe XXIV emission lines. Contribution functions are calculated from the CHIANTI database (Del Zanna et al., 2021).

modynamic conditions. That is, temperatures and densities must be high enough to allow the desired number of electrons to be freed, but not too high that the desired ion cannot exist (as too many electrons have been lost). The range at which adjacent ion populations can exist overlap, and the ionisation levels are determined by the current population of each ion, and the rates of ionisation and recombination. These rates are primarily determined by the temperature and density of the plasma. Ionisation equilibrium occurs when the rate of recombination equals that of ionisation. The probability of a certain ion existing at a given density or temperature is called the *contribution function*. Figure 1.1 shows example temperature contribution functions ($g(T)$) for four Fe ions, calculated from the CHIANTI database (Del Zanna et al., 2021). Similar plots can be made to show change in contribution function with density.

1.2.2 Spectroscopy

Stripping an electron from an atom requires energy, and similarly, recombining an electron to an ion leaves a surplus of energy. An electron requires a specific quan-

tity of energy to separate from its atom, dependent on the element and prior level of ionisation. One way in which the electron can gain this energy to overcome its bond with the atom is through ionisation by collisional excitation (collisional ionisation), the level of which is dependent on the plasma density and temperature described above. Within plasma in ionisation equilibrium, there must be a case of recombination for each case of this collisional ionisation. As an electron is recaptured by an ion, due to the conservation of energy, it must release the energy it initially gained to escape. This energy is released in the form of a photon, with a corresponding frequency $\nu = E/h$, where h is the Planck constant. Due to the fact that the required energy absorbed and released during this process is specific and unique to each ion, the continuous repetition of this process within the plasma produces enough photons to produce an emission spectrum - a spike in intensity of the specific wavelength/frequency of light, above the background continuum. In addition to emission and absorption of ions ejecting and capturing electrons, electrons jumping between specifically-permitted energy levels within the ion (through collisional excitation) also produce emission lines of the corresponding wavelength. Some of these atomic transitions are more common than others, determining the strength of the emission line. As a result of this, a specific ion may produce many emission lines over the solar spectra.

An example spectral emission line of Fe XIII, as observed by the Hinode Extreme-Ultraviolet Imaging Spectrometer (EIS), is shown in Figure 1.2. As emission lines are unique to each ion, their detection in a spectrum indicates the presence of that ion within the emitting plasma. The simplest of spectral emission lines have three fundamental independent properties, which can reveal information about the plasma from which the photons were created.

• **Line centroid -** As discussed in the previous paragraph, the central wavelength (or centroid) of an emission line is determined by the energy required to release/capture an electron for a given ion, and thus occurs at a set wavelength. However, motion of the emitting plasma can cause this centroid to shift through the Doppler effect (Peach, 1981). The Doppler effect occurs as a source of a wave (e.g. light or sound)

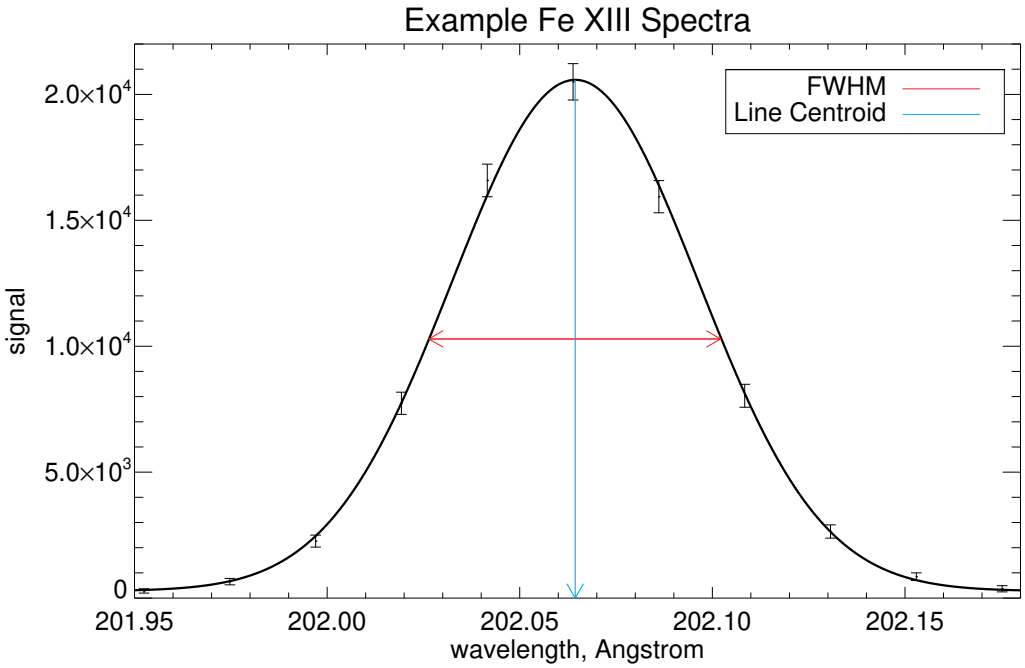

Figure 1.2: Example emission spectra for Fe XIII from Hinode-EIS, with a Gaussian fit of the data (black curve). The red and cyan arrows visualise the FWHM and line centroid respectively.

is moving towards or away from the observer, causing the emitted wave to become compressed or extended. In the case of a spectral emission line, this compression or extension of the wave shortens or lengthens the wavelength – producing blue or red shift of the line. By measuring the deviation of a measured centroid (emitted from plasma in motion) to the theoretically predicted centroid of plasma at rest, one can determine the plasma velocity via the equation

$$\frac{\lambda - \lambda_0}{\lambda_0} = \frac{\mathbf{v}}{c}, \tag{1.1}$$

where λ is the observed wavelength, λ_0 the rest wavelength, c the speed of light and $\mathbf{v}$ the Doppler velocity. This Doppler velocity measures only the bulk motion plasma in the line-of-sight (LOS), and cannot provide insight to motion within the plane-of-sky (POS). In order to extract the true LOS bulk plasma velocity, one must also be careful to take into account instrumental causes of red and blue shift, such as the orbital motion of the spacecraft or the Earth.

• **Line width -** Spectral emission lines are not infinitely thin, as plasma in the LOS

will experience motion in addition to the bulk flow of the plasma (Peach, 1981). Plasma does not have a temperature of absolute zero, and thus has a random thermal motion associated with the temperature of the plasma. This thermal velocity v_t is given by

$$v_t = \sqrt{\frac{2k_B T_i}{m_i}}, \tag{1.2}$$

where T_i is the ion temperature, m_i the ion mass and k_B the Boltzmann constant. The random nature of this thermal motion means plasma within the LOS will be moving in all directions – towards the observer, away from the observer, directly in the POS, and everywhere in between. The superposition of these blue and red shifts within the LOS broadens the emission line. Due to the Maxwellian distribution of the thermal velocity, the broadened emission line can be approximated by a Gaussian function. The width of this curve is often defined by the Full-Width-Half-Maximum (FWHM). A Gaussian fit to the observed Fe XIII line is plotted in Figure 1.2. The horizontal red line in this figure shows a visual definition of the FWHM – literally the (*full*) *width* of the emission line at the location where emission is at *half* the *maximum* value.

Beyond thermal processes, further motion within the plasma, such as turbulence, also cause a variety of velocities along the LOS – and thus also contribute to line broadening. Given that an emission line originates from a specific ion species, which can only exist at a certain temperature range determined by its contribution function (Figure 1.1), we can estimate the expected broadening of the line from thermal broadening alone. Any excess broadening beyond this thermal process (and any other known instrumental broadening effects) is called 'non-thermal broadening' ($FWHM_{non-thermal}$). Like thermal broadening, this can be characterised by a corresponding 'non-thermal velocity'. This can be thought of as

$$FWHM^2_{non-thermal} = FWHM^2_{total} - FWHM^2_{thermal}(-FWHM^2_{instrumental}), \tag{1.3}$$

where $FWHM_{total}$ is the observed width, and $FWHM_{thermal}$ and $FWHM_{instrumental}$ the thermal and instrumental widths respectively (Harra et al., 2013). Sources of non-thermal broadening include opacity broadening, Stark broadening, and unresolved plasma flows such as waves or turbulence. Opacity broadening occurs as emitted photons are reabsorbed again before they reach the observer. Photons near line-centre have a higher probability of being absorbed, resulting in a broader FWHM. In optically thin plasma, such as the solar corona, this process is rare. Stark broadening is the splitting of an emission line due to the presence a strong electric field (Stark, 1914).

• **Intensity -** The intensity of an emission line relates to the total number of photons detected which can confidently be attributed to the emission line. This depends on the temperature and density of the plasma, the ion contribution function, and even the response/sensitivity of the detector. Given that the number of emitted photons is independent of plasma velocities (and thus the line centroid and width), emission line amplitude will fall as the line width increases. The line intensity is therefore calculated via the area under the Gaussian emission curve, such as the one shown in Figure 1.2. In many cases of the solar spectrum, multiple emission lines exist within a small wavelength range, and thus overlap due to the broadening processes. In these cases, multiple Gaussians may be fitted to a single wavelength window, in order to extract the signal from a specific line.

• **Temperature and Density -** Different emission lines for ions of a given element have different dependencies on the local temperature and density (different contribution functions). By carefully selecting line pairs, it is possible to choose a combination of lines which do not vary significantly with density, but do with temperature (and vice versa). For these lines, the ratio of the contribution functions provides a theoretical relationship between the line intensity, and either the temperature or density of the emitting plasma. From the theoretical ratio, the ratio of the observed line intensities can be used to calculate these plasma diagnostics. Note: this can only be achieved with confidence of how the observing instrument's sensitivity changes with wavelength. For the solar corona, the strength and temperature/density depen-

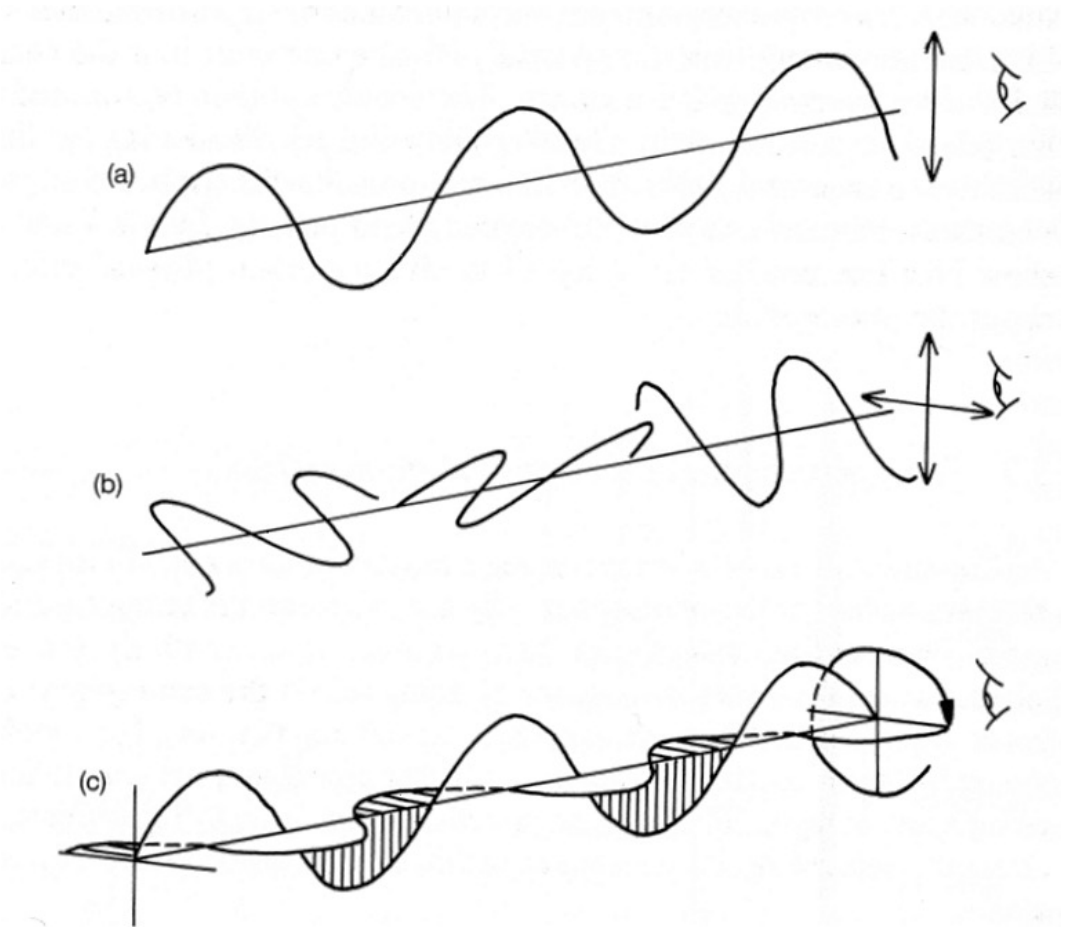

Figure 1.3: A simple cartoon to visualise the polarisation of light. (a) Linear polarisation. (b) Unpolarised light. (c) Circular polarisation. Source: Unknown.

dence of emission lines can be found in databases such as CHIANTI (Del Zanna et al., 2021).

To summarise, by fitting a Gaussian function to a carefully selected combination of spectral emission lines, we are able to determine the intensity, Doppler bulk LOS velocity, non-thermal velocity, and even temperature and density of the source plasma. Spectroscopy is a powerful tool! It is worth noting that fitting a Gaussian function is not always suitable in reality, as extreme non-thermal processes and superposition of processes within the LOS can cause an emission curve to deviate away from a Gaussian profile.

1.2.3 Spectropolarisation

Picture a beam of photons travelling as a transverse light wave. A transverse wave-particle oscillates perpendicular to the direction of travel, but this can be at any angle. E.g. if a wave travelled out of this page, it could be oscillating in the up-down, left-right, or any diagonal plane. Unpolarised light has no preferential direction for this oscillation, with light waves oscillating in every plane. If you were to pass this unpolarised light through a series of thin vertical slits, only the photons oscillating in the up-down plane would be able to pass through, blocking the majority of the unpolarised light. The remaining light waves, which only travel in a single plane, are now polarised. Outside of astronomy, this is the principle idea behind polarised sunglasses, which use polarising slits to only allow a fraction of light to pass. This is in contrast to 'regular' sunglasses, which reduce the intensity of all the light passing through.

Light can be linearly or circularly polarised. Linear polarisation is similar to that described above, with light oscillating in a single plane. Circular polarisation is harder to visualise, but can be thought of as the superposition of two plane-polarised rays, a quarter of wavelength out of phase, so that the vector sum of the wave motions rotate as the wave propagates. Such a circular polarisation signature would be created by rotating the vertical slit described above. Figure 1.3 shows a cartoon of linear and circular polarisation.

The polarisation of light $\overrightarrow{S}$ can be fully described by four parameters, S_0, S_1, S_2 and S_3 (Landi Degl'Innocenti & Landolfi, 2004). These are often referred to as the 'Stokes' parameters, I, Q, U and V. That is,

$$\overrightarrow{S} = \begin{pmatrix} S_0 \\ S_1 \\ S_2 \\ S_3 \end{pmatrix} = \begin{pmatrix} I \\ Q \\ U \\ V \end{pmatrix} \tag{1.4}$$

Stokes I is the intensity of the light, Stokes Q and U are the two components of linear polarisation, and Stokes V the measure of circular polarisation. A polarisation

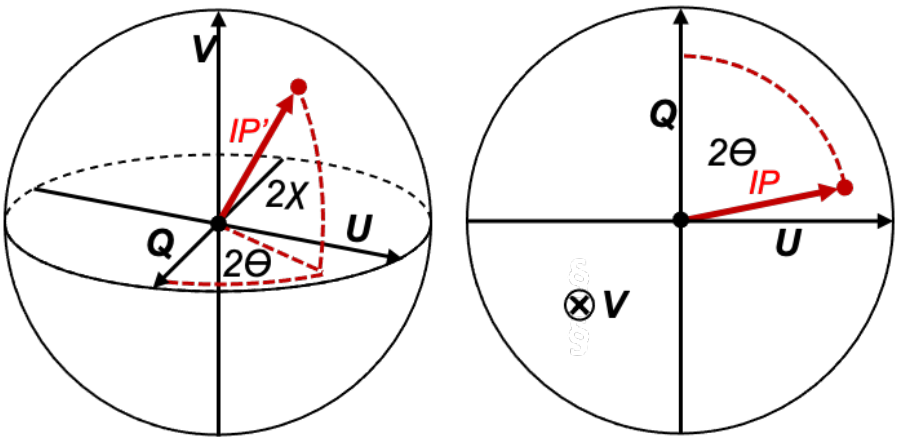

Figure 1.4: Left: Definition of a polarisation vector in spherical coordinates, with vector length IP'. Right: Rotated polarisation sphere to centre of linear polarisation frame, with vector length $IP = IP' \cos 2\chi$.

state can be shown graphically on a sphere, as shown in an example in Figure 1.4 (left). The visualisation of polarisation in this way is sometimes referred to as the Poincaré Sphere (Collett, 2005). In spherical coordinates, this polarisation space can be defined as:

$$Q = IP' \cos(2\theta)\cos(2\chi) = IP\cos(2\theta), \tag{1.5}$$

$$U = IP' \sin(2\theta)\cos(2\chi) = IP\sin(2\theta), \tag{1.6}$$

$$V = IP' \sin(2\chi). \tag{1.7}$$

The measurements of Q, U and V can therefore be either positive or negative, and dependent on the reference frame of the observer. Stokes I is total intensity, and thus equal in Cartesian and Spherical frames. In astronomy, it is standard for the POS to define $\chi = 0$. Therefore, θ is the angle within the POS (often defined as 0° pointing north), and χ the angle out of the POS. P' is the fraction of polarised light (and thus IP' represents the total intensity of polarised light), and P is the fraction of linearly polarised light (equal to $P' \cos(2\chi)$). Because polarisation vectors have no preferred direction (and so not *truly* a vector in the mathematical sense), the factor

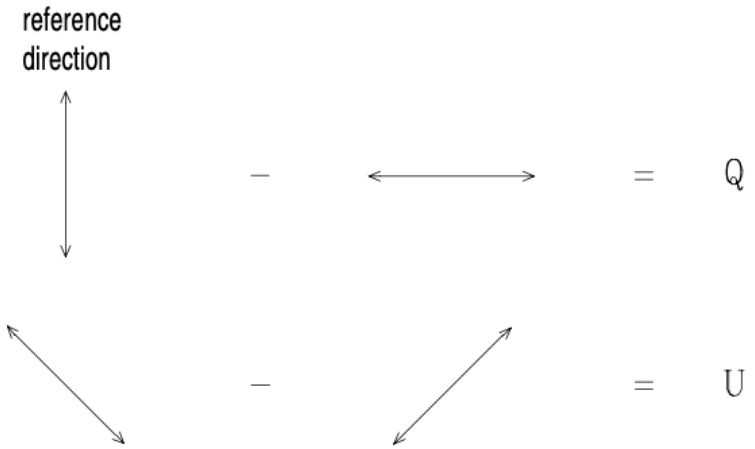

Figure 1.5: Schematic definitions of Stokes Q and U, amended from Landi Degl'Innocenti & Landolfi (2004)

of two before θ and χ is required so that each position on the polarisation sphere is a uniquely defined polarisation vector. That is, unique solutions only exist from $-180^\circ < \theta < 180^\circ$ and $-90^\circ < \chi < 90^\circ$.

A measurement of Q can be attained by observing light after it passes through two perpendicular slits. That is, Stokes Q is related to the count of photons oscillating N-S subtracted by the count of photons oscillating E-W. Stokes U is observed the same way, but in a slit configuration 45° to the Stokes Q reference frame. A simple cartoon of this is shown in Figure 1.3, amended from Landi Degl'Innocenti & Landolfi (2004).

Measuring the polarisation of a spectral line reveals properties of the source plasma. Stokes I is the total intensity of the emission/absorption line, no different to the intensity measured by regular spectroscopy (i.e. no polarisation measurements). Stokes V, circular polarisation, is created by plasma ions gyrating around a magnetic field line. The level of gyration, and thus the observed Stokes V parameter, is dependent on the LOS component of the local magnetic field within the plasma (Landi Degl'Innocenti & Landolfi, 2004). The sign of Stokes V is determined by whether the magnetic field is directed towards or away from the observer.

Linear polarisation (Stokes Q and U) can reveal the projected direction of the magnetic field in the POS (Landi Degl'Innocenti & Landolfi, 2004). This projection is shown in the right panel of Figure 1.4. Stokes Q and U are dependent on the

observing reference frame, and are often converted into normalised linear polarisation P and azimuth – two measures of linear polarisation independent of the initial reference frames used to measure Stokes Q and U. Normalised linear polarisation is the fraction of incident radiation which is linearly polarised, given by:

$$P = \sqrt{U^2 + Q^2}/I. \tag{1.8}$$

The azimuth is the projected angle of linear polarisation onto the POS (θ in Figure 1.4), with a 90° of ambiguity to the true magnetic field direction. This is given by:

$$\theta = \frac{1}{2}\arctan\left(\frac{U}{Q}\right). \tag{1.9}$$

The origin of the ambiguity can be seen by again examining the right panel of Figure 1.4. A polarisation state rotated into the opposite quadrant will yield the same value of $\arctan(U/Q)$. This rotation of 2θ by 180° corresponds to an azimuth ambiguity of 90°.

The instrumentation used to measure polarisation is discussed in the instrumentation section of this thesis. Furthermore, the mechanisms leading to the formation and destruction of linear polarisation in coronal plasmas are explored in the relevant science chapter, Chapter 3.

1.2.4 Electromagnetism

Electromagnetism is one of the four fundamental forces in physics - the origin of all known forces in nature. The foundations of classical electromagnetism can be represented by the Maxwell equations, which are as follows:

• **Gauss' Law –** *Conservation of electric flux.* That is, the electric flux through a closed surface is equal to the total charge within in. This can be written as

$$\nabla \cdot \mathbf{E} = -\frac{\rho}{\varepsilon_0}, \tag{1.10}$$

where $\nabla \cdot \mathbf{E}$ is the divergence of the electric field $\mathbf{E}$, ρ the charge density and ε the

vacuum permittivity.

• **Gauss' Law for magnetism –** *No magnetic monopoles*. The total flux ($\nabla \cdot \mathbf{B}$) of magnetic field $\mathbf{B}$ through a closed surface is zero – the flux of north and south polarity field lines are balanced. That is,

$$\nabla \cdot \mathbf{B} = 0. \tag{1.11}$$

• **Maxwell-Faraday's Law –** *Law of induction*. A time varying magnetic field ($\frac{\partial \mathbf{B}}{\partial t}$) will generate a spatially-varying electric field ($\nabla \times \mathbf{E}$), or vice versa. The variation of electric and magnetic fields are perpendicular to one other. As in,

$$\nabla \times \mathbf{E} = -\frac{\partial \mathbf{B}}{\partial t}. \tag{1.12}$$

• **Ampère's Law –** *Magnetic field generation*. A magnetic field is created by either a flowing current (determined by current density $\mathbf{j}$), or a time varying electric field ($\frac{\partial E}{\partial t}$).

$$\nabla \times \mathbf{B} = \mu_0 \mathbf{j} + \mu_0 \varepsilon_0 \frac{\partial \mathbf{E}}{\partial t}. \tag{1.13}$$

In the case of a static electric field, $\frac{\partial \mathbf{E}}{\partial t} = 0$ and $\nabla \times \mathbf{B} = \mu_0 \mathbf{j}$, where μ_0 is the permeability of free space. The force exerted on a particle by the magnetic and electric fields, $\mathbf{j} \times \mathbf{B}$, is known as the Lorentz force.

1.2.5 Magnetohydrodynamics

In the neutral atmosphere of the Earth, the behaviour of gases can be explained by hydrodynamics - the mechanics of a neutral fluid. However, hydrodynamics cannot accurately represent the physics of magnetised fluids, such as plasma. Instead, we use magnetohydrodynamics (MHD) – the combination of electromagnetism and plasma fluid mechanics. It is important to note that MHD treats plasma as a neutral fluid, and does not consider any particle-like properties of plasma on very small scales.

• **Lorentz Force –** The Lorentz force, $\mathbf{j} \times \mathbf{B}$, can be derived by rearranging Ampère's law (Equation 1.13) and taking the cross product with $\mathbf{B}$. Using the vector

identity

$$\nabla(\mathbf{A}\cdot\mathbf{A}) = 2\mathbf{A}\times(\nabla\times\mathbf{A}) + 2(\mathbf{A}\cdot\nabla)\mathbf{A},$$

it can be shown that the Lorentz force can written as:

$$\mathbf{j}\times\mathbf{B} = -\nabla\frac{\mathbf{B}^2}{2\mu_0} + \frac{(\mathbf{B}\cdot\nabla)\mathbf{B}}{\mu_0}, \tag{1.14}$$

where the first term on the right hand side is the magnetic pressure force $-\nabla(B^2/2\mu_0)$, and the second term the magnetic tension $(\mathbf{B}\cdot\nabla)\mathbf{B}/\mu_0$. The magnetic pressure force acts isotropically to distribute magnetic pressure differences along the field lines evenly, whereas the magnetic tension force acts to 'straighten' the magnetic field line, by exerting a transverse force towards the centre of curvature.

• **Induction equation –** The change of a magnetic field in a plasma environment can be determined by the induction equation. To derive the induction equation, we first introduce Ohm's law for the reference frame of a conductive fluid –

$$\mathbf{E} + \mathbf{v}\times\mathbf{B} = \frac{\mathbf{j}}{\sigma}, \tag{1.15}$$

where $\mathbf{v}$ is the plasma velocity and σ the electric conductivity. Ohm's law states that a plasma travelling through a magnetic field $(\mathbf{v}\times\mathbf{B})$ induces an electric current $\mathbf{E}$ to create a current density $\mathbf{j}$. Combining Ohm's law with the Maxwell-Faraday law (eq. 1.12), we derive the Induction equation

$$\frac{\partial\mathbf{B}}{\partial t} = \nabla\times(\mathbf{v}\times\mathbf{B}) + \eta\nabla^2\mathbf{B}, \tag{1.16}$$

where $\mathbf{v}$ is the plasma velocity and η the ohmic magnetic diffusivity $\eta = \frac{1}{\mu_0\sigma}$ (units m^2/s).

The magnetic Induction equation shows that the change of magnetic field can be determined by both advection (first term of the equation) and diffusion (second term of equation).

• **Magnetic Reynolds Number and 'Frozen-in' Theorem –** To determine whether

advection or diffusion dominates in a plasma, we can take the ratio of the two components of the Induction equation. The ratio of these terms is called the magnetic Reynolds number. By using dimensional analysis, where v and l are characteristic values for velocity and length scale, we derive the Reynolds number as

$$R_m = \frac{\nabla \times (\mathbf{v} \times \mathbf{B})}{\eta \nabla^2 \mathbf{B}} = \frac{vB/l}{\eta B/l^2} = \frac{vl}{\eta} = \mu_0 \sigma v l. \tag{1.17}$$

On length-scales where $R_m >> 1$, advection dominates over diffusion in the plasma. If this criterion is satisfied, plasma motion is determined by the advection of magnetic fields. That is, the plasma and magnetic field flow together, rather than the plasma diffusing through the magnetic field. This condition is referred to as the 'frozen-in' theorem, where plasma can be considered bound to the magnetic field – free to flow along magnetic field lines, but not between or across them.

• **Plasma β –** Plasma frozen in to the magnetic field is subject to both magnetic and plasma forces. In order to determine which of these processes dominate in a plasma, we can define Plasma β as the ratio of plasma pressure nk_BT to magnetic pressure $B^2/2\mu_0$. This becomes

$$\beta = \frac{p_{plasma}}{p_{mag}} = \frac{nk_BT}{B^2/2\mu_0}, \tag{1.18}$$

where n is number density, T temperature, and k_B the Boltzman constant. Therefore, magnetic forces dominate in $\beta << 1$ plasma, and plasma forces in $\beta >> 1$ plasma regimes. In these scenarios, one can consider only the dominant process. For regions where $\beta \sim 1$, both magnetic and plasma forces must be considered.

• **Alfvén waves –** Disturbances along a magnetic field can travel faster than the plasma population within it, via Alfvén waves (Alfvén, 1942), which propagate via the tension force (second term in Equation 1.14). Alfvén waves are incompressible transverse waves, travelling along the magnetic field at the Alfvén speed – the fastest speed at which information can travel through a magnetic field. Due to their incompressible nature, Alfvén waves do not affect the plasma density along the field, instead causing a inversely proportional variation in magnetic field and

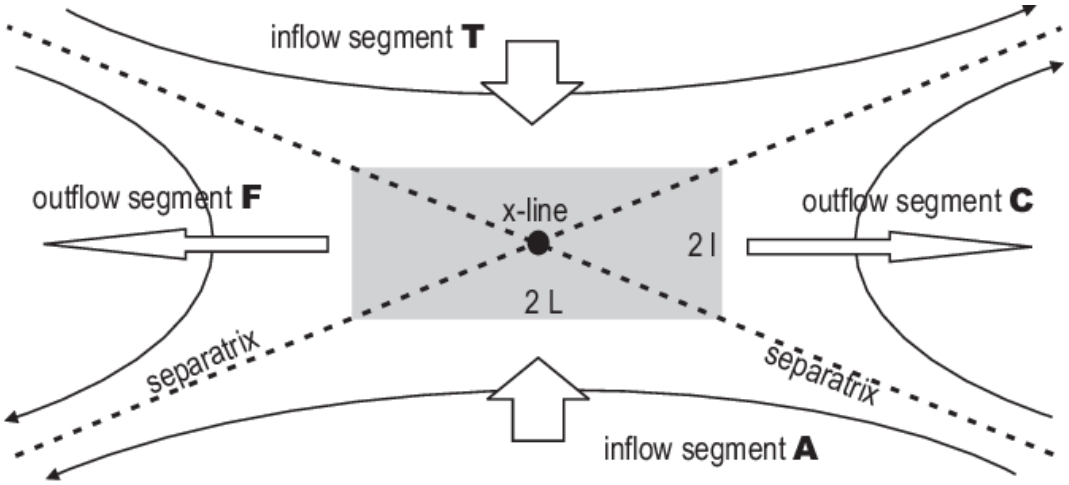

Figure 1.6: Magnetic reconnection cartoon, Laitinen et al. (2006)

plasma velocity. The Alfvén speed is determined by the magnetic field magnitude B and mass density ρ, through the equation

$$V_A = \frac{B}{(\mu_0 \rho)^{1/2}}. \tag{1.19}$$

This work earned Hannes Alfvén the 1970 Nobel Prize in Physics – the only time the award was given for work in solar/plasma physics (so far).

1.2.6 Magnetic Reconnection

Across magnetic field lines with an anti-parallel component in their field directions, magnetic 'free' energy can exist within the field. Under certain conditions, over sufficiently small length scales where $R_m \lesssim 1$, diffusion can occur between magnetic fields (Equation 1.17). Free energy must exist within the field lines for this diffusion to occur, as (with the absence of an external force/driver) the magnetic fields will only evolve into a lower energy configuration. This applies for both diffusion and advection of the fields.

The diffusion of oppositely orientated magnetic field lines induces an electric current between them, flowing perpendicular to both the directions of the magnetic field and field inflow to the diffusion region (v_{inflow}) (Maxwell-Faraday's Law of induction, Equation 1.16). In the cartoon shown in Figure 1.6, this induced current flows into the page. This current layer is known as a 'current sheet', both within

MHD and solar physics. The plasma is not 'frozen-in' within this region, and the plasma becomes decoupled from the magnetic field. Out of the diffusion region, there is an outflow $v_{outflow}$ of magnetic field lines reconfigured into a lower energy configuration. Newly-reconnected field lines will be evacuated from the region at the Alfvén speed. The regions of inflow and outflow do not mix, and are separated by the suitably named 'separatrix' region. This configuration is shown in Figure 1.6 by Laitinen et al. (2006).

This reconfiguration of the magnetic topology through diffusion is known as magnetic reconnection, and will continue for as long there is a suitable inflow of magnetic field. The rate of reconnection relates to the Lundquist number S – the ratio of the Alfvén wave crossing to the diffusion timescale. That is,

$$S = \frac{LV_A}{\eta}, \tag{1.20}$$

where L is the half length of the current sheet, and η the magnetic diffusivity of the plasma. Specific models relevant to magnetic reconnection in solar flares, and their dependency on the Lundquist number are explored in section 1.4.4.

The free energy released through the reconnection process must be conserved, and thus can be converted into heating, particle acceleration or EM radiation within the reconnected plasma.

1.3 The Solar Atmosphere

The surface of the Sun is called the photosphere. This is the highest optically-thick layer of the Sun, and is therefore the source of the sunlight seen on a sunny day. The photosphere has a temperature of around 5760 K and, just like the rest of the Sun, consists of mostly Hydrogen H ($\approx 80\%$), some Helium He ($\approx 19\%$) with a trace mix of heavier elements including Si, Ca, Mg and Fe ($< 1\%$).

Immediately above the photosphere is the chromosphere. Here densities rapidly decrease, whilst temperatures slowly increase between 5000 and 12000 K. Above the chromosphere is the tenuous and optically-thin corona, separated by a thin transition region. Temperatures dramatically increase through this region, up

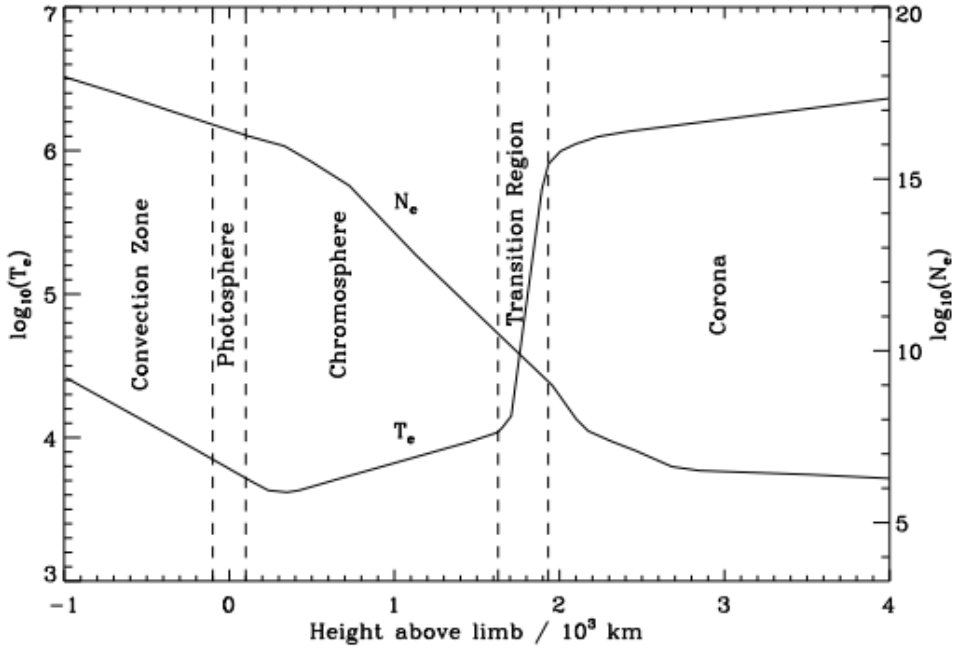

Figure 1.7: Temperature and density variation throughout the Sun and its atmosphere, Gabriel & Mason (1982).

to 10^6 K in the corona. The exact mechanism causing this jump in average temperature between the photosphere and corona is not certain. The temperature and density profiles through the layers of the solar atmosphere are shown in Figure 1.7 (Gabriel & Mason, 1982). Example images of the photosphere, chromosphere and corona are shown in Figure 1.9.

Far away from the nuclear forces acting in the Sun's core, the solar atmosphere is dominated by electromagnetic forces. In the corona, with low densities ($\sim 10^8 cm^{-3}$) and magnetic field strengths of order 10 G, we find plasma $\beta << 1$. Plasma forces therefore have little influence over this region of the atmosphere. This is in contrast to the photosphere, where convective plasma forces play the dominant role, dragging the magnetic field. In the chromosphere, between the high β photosphere and low β corona – β is of order unity, meaning both plasma and magnetic processes play a role in determining the physics of this region. A plot showing the variation of plasma β through the atmosphere is shown in Figure 1.8 (Gary, 2001).

For most of the Sun, in quiet Sun conditions, the Magnetic Reynolds Number (R_m, Equation 1.17) is high, meaning advection dominates over diffusion. A

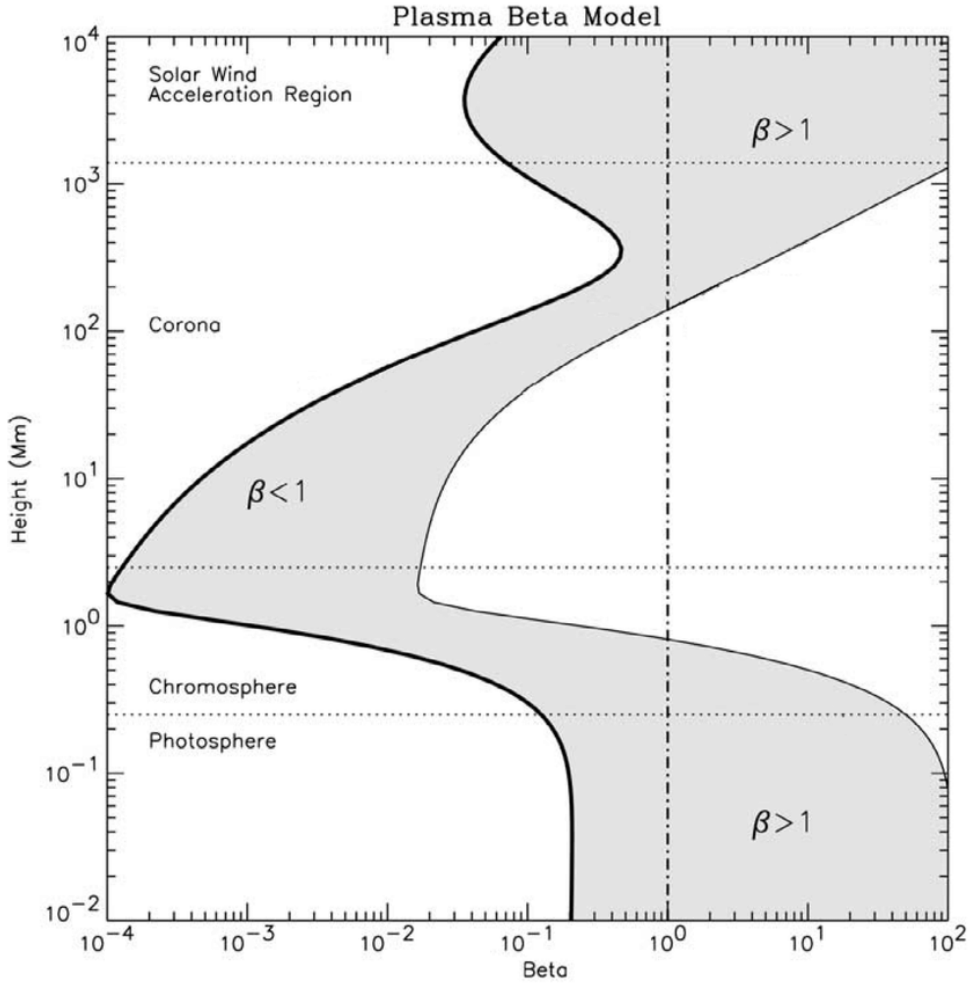

Figure 1.8: Plasma beta variation through the atmosphere, Gary (2001).

consequence of this is that the plasma and magnetic fields are thus 'frozen-in' to one-another, meaning that regardless of whether plasma or magnetic processes are dominating, plasma is bound to the magnetic field (and vice versa). Plasma can therefore flow easily along field lines, but not easily between or across them. The same applies to processes within the plasma, such as thermal conduction.

1.3.1 Solar Spectra

With a surface (photospheric) temperature of 5760 K, the solar continuum lays close to a blackbody curve with a peak of 480 nm. This is what gives the Sun its yellowish glow. Example continuum images of the photospheric (617.3 nm) and chromospheric (170 nm) continuum are shown in Figure 1.9. (The instruments used to take the data within this figure are introduced in depth in Chapter 2). However, beyond

the blackbody continuum, absorption and emission above the Sun's surface give cause to a vast range of spectral emission and absorption lines in the quiet Sun.

• **Absorption spectra –** Absorption lines within the solar spectra primarily originate from plasma in the photosphere and chromosphere. Continuum photons pass through these layers, interacting with ions and neutral atoms to excite electrons within them. These particles absorb this radiation, at a wavelength corresponding to the energy level change of the electrons. As a result, the intensity at these wavelengths is reduced within the solar continuum - creating an absorption line.

• **Emission spectra –** In the optically thin corona, the majority of photons from the Sun's continuum pass straight through without interacting with coronal plasma. Excitation of material at these densities come instead from ion-electron collisions via collisional excitation. As described in section 1.2.2, in ionisation equilibrium, rates of ionisation and recombination must equal each other. Ionisation occurring due to collisional excitation (the rate of which is determined by temperature and density) must therefore be balanced with recombination. Recombination of an ion results in the release of a photon, corresponding to the energy gained from the re-captured electron. These emitted photons from the corona produce emission spectra, most common within the EUV region of the solar spectrum. The rate of collisional excitation is dependent on the square of the electron density (n_e^2), and thus the intensity of these emission lines drop off rapidly as density falls through the corona. An example broadband image containing emission from the extreme-ultraviolet (EUV) Fe XII 192 Å line is shown in Figure 1.9.

• **Coronal Forbidden Lines –** As described in section 1.2.2, some atomic transitions between electron levels are more common than others. Coronal forbidden lines are emission lines arising from some of the least common of these transitions within the corona. These are often found in the lower-energy infrared part of the spectrum, produced primarily via photoionisation from photospheric photons (Del Zanna & Mason, 2018). Due to their low intensity (resulting from the low probability of the transition), they can only be observed off-limb, against the dark background of space, and not on disk (unlike the higher-intensity EUV emission line

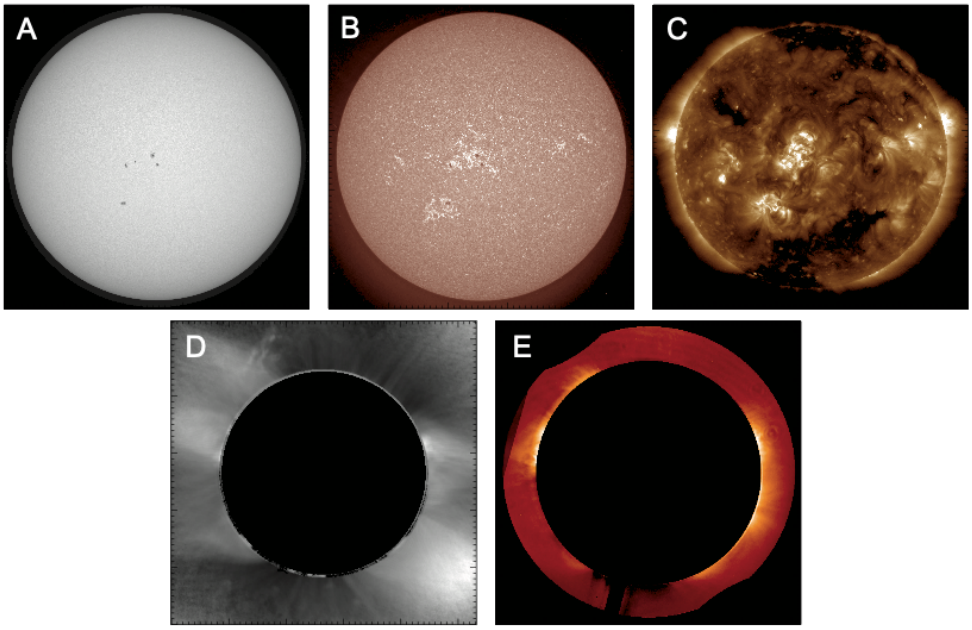

Figure 1.9: A: HMI intensity, B: AIA 1700 Å C: AIA 193 Å D: K-Cor White Light (NRGF-processed), E: CoMP 1074.9 nm intensity. Images are from the same time period on 13th August 2016.

counterparts). One prominent example is the infrared Fe XIII line pair (Chevalier & Lambert, 1969), which feature heavily in this thesis. An example intensity image of one of these Fe XIII lines is shown in Figure 1.9.

• **Scattering –** Interactions between photons and electrons are common in the corona. Photons travelling radially away from the Sun can be scattered by a coronal electron, accelerating the photon 'randomly' away from the radial direction through Thomson Scattering. As a result of this, we observe scattered photons above the solar limb, where we do not normally see radially-travelling photons. It is these scattered photons that we observe during a total solar eclipse, or with white-light coronagraph instruments (section 2.4.2). This white light scattering corona has a brightness that falls off with (n_e), rather than the (n_e^2) factor for the collisionally-excited emission line corona. Due to this difference in density dependence, we therefore see this 'electron-scattered' corona at much higher altitudes than the 'collisionally-excited' corona. An example image of the white-light corona is given in Figure 1.9.

1.3.2 Active Regions

Active regions are areas of concentrated magnetic field in the solar atmosphere. In the photosphere, the high magnetic field strength can suppress convection from below (and associated heat inflow) – acting to thermally isolate the photospheric plasma and allowing it to cool to temperatures lower than the surrounding photosphere. This cool plasma has a darker appearance in white-light – creating a sunspot. In the corona, plasma traces the strong magnetic fields, clearly visible by instruments observing a suitable temperature range, as 'active region loops'. Active regions emerge over the timescales of hours to days, and can live for several solar rotations – on the timescales of weeks to months. As the photospheric footpoints of active regions evolve, or as new magnetic flux emerges – coronal magnetic fields are subjected to an increase in magnetic free energy. This can cause active region coronal magnetic fields to evolve on much shorter timescales than their photospheric counterparts (van Driel-Gesztelyi & Green, 2015). Like many other things in nature, active region magnetic fields prefer to be in the lowest energy state possible. Thus, as photospheric evolution increases magnetic free energy – it has to go somewhere.

1.4 Solar Flares

Solar flares are the rapid release of free magnetic energy in the solar atmosphere (Benz, 2016). Active region magnetic loops, which cannot pass through one-another in a frozen-in plasma, experience an increase of magnetic free energy as active region footpoint motion and flux emergence evolve. Should conditions be right, magnetic diffusion can begin to dominate over advection on small scales (final term of the induction equation), and the magnetic topology is able to reconfigure itself into a lower-energy configuration via magnetic reconnection. This magnetic free energy must go somewhere, and thus gets converted into plasma heating, electromagnetic radiation, MHD waves, and particle acceleration. It is these forms of energy that make up a solar flare. Flares are sometimes accompanied by the eruption of plasma and magnetic field from the solar atmosphere, known as a Coronal

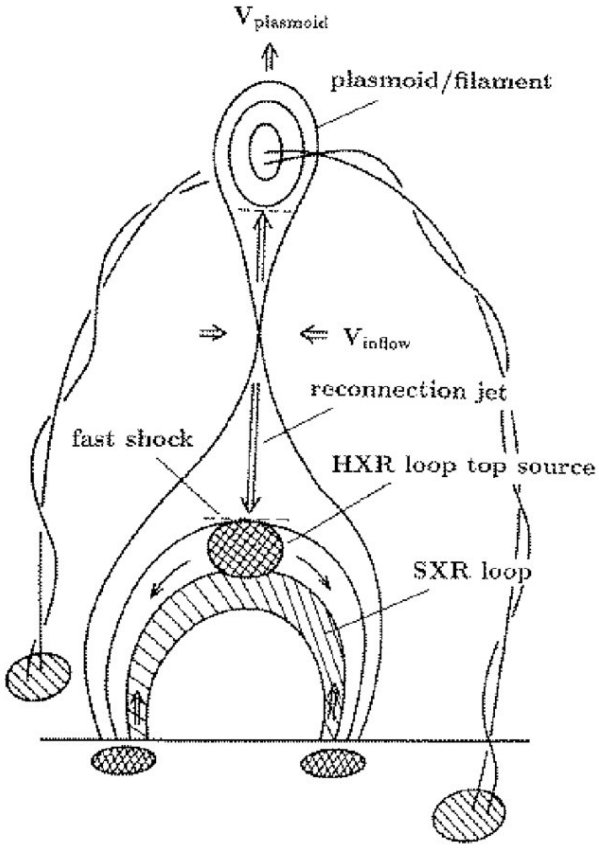

Figure 1.10: Simple cartoon of the CSHKP flare model, (Shibata et al., 1995).

Mass Ejection (CME).

Not all flares are created equal. The largest solar flares release up to 10^{25} Joules of energy, making them one of the most energetic events in the solar system. Flares are classified by a class system, dependent on the observed level of soft X-rays (and therefore related to total energy release). From lowest to highest, on a base-10 logarithmic scale, the solar flare classes are B, C, M and X. Using observed soft X-ray levels to define and compare flare energies is not a perfect system, as a partially occulted flare at the solar limb will measure as a lower class than the same event measured at centre-disk.

1.4.1 Standard Eruptive Flare Model

The Standard Eruptive Flare Model is able to account for many observed phenomena in solar flares. First introduced in 2D by Carmichael (1964), Sturrock (1968), Hirayama (1974) and Kopp & Pneuman (1976), it is sometimes also referred to as

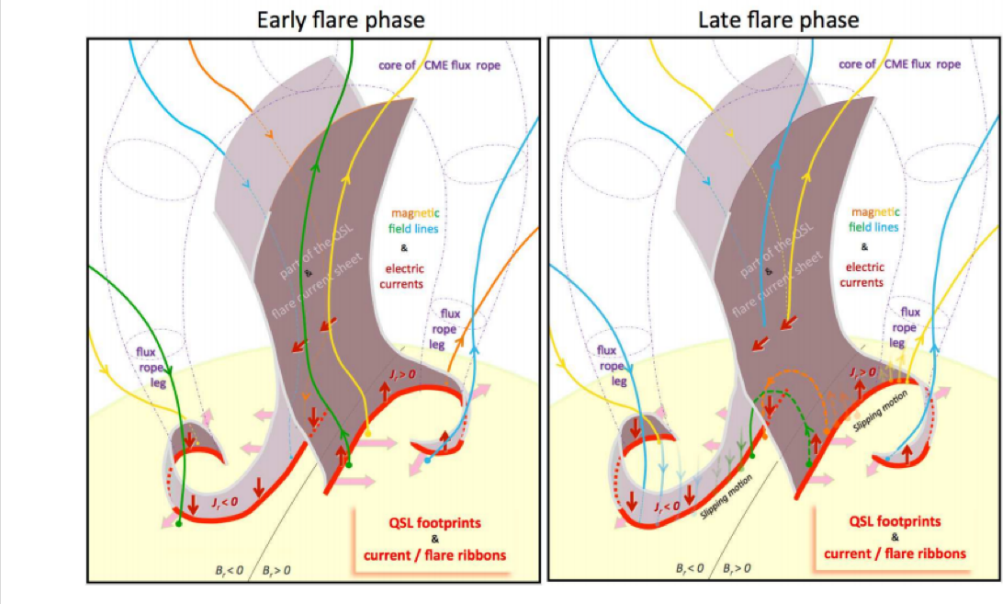

Figure 1.11: 3D cartoon of the standard eruptive flare model, (Janvier et al., 2013). Left and right panel show the field configuration before and after reconnection.

the CSHKP eruptive flare model. A classic cartoon of this model by Shibata et al. (1995) is shown in Figure 1.10. This cartoon is often criticised within the solar flare community for its simplicity, but is successful at portraying some of the key features in a flare. For 3D, Janvier et al. (2014) provide an excellent cartoon, presented in Figure 1.11.

In the CSHKP model, a magnetic flux rope sits in the solar atmosphere, beneath an overlying magnetic field. As the flux rope rises, oppositely orientated field lines beneath it are drawn together at velocity v_{inflow}. Between the oppositely orientated field lines, diffusion can begin to dominate over advection in the plasma and a current sheet forms (Section 1.2.6). In the cartoon in Figure 1.10, the reconnection site is portrayed as an X-point, with the induced current flowing within the LOS of the diagram. In the corona, this region of current, referred to from hereon as a 'current sheet', can only form over regions as small as 10m (Litvinenko, 1996). Figure 1.11 shows the full extent of the current layer, analogous to the quasi-separatric layer (QSL). These scales are below the current limit of observation, and cannot be observed directly. However, sheets of hot and turbulent plasma can form around these current sheets, which have been observed infrequently, and form the bulk of

analysis in Chapters 3 and 4. We refer to these heated sheets of plasma as plasma sheets.

The newly reconnected field lines are ejected above and below the current sheet region. Above the current sheet, the field lines reconnect to form a 'plasmoid' feature, wrapped around and contributing to the flux rope Janvier et al. (2013). As the magnetic arcade field lines initially overlying the flux rope are reconnected in this way, the magnetic tension forces keeping the flux rope from erupting are slowly removed. This causes the flux rope and newly reconnected field lines to erupt away from the Sun as a CME. As the CME erupts, remaining overlying fields above the flux rope are tightened, and pulled inwards beneath the erupting structure. This continued inflow of field lines continue to power reconnection within the current sheet region, which in turn continues to accelerate the CME.

Beneath the reconnection point, field lines are evacuated from the reconnection site, travelling at the local Alfvén velocity. These newly-reconnected field lines are then able to relax into a lower energy configuration to form the 'flare loops'. Fast moving high energy protons and electrons are also produced, energised from the energy output from the reconnection process. These high energy particles spiral down the flare loops to the cooler chromosphere, causing enhanced collisional excitation. This results in an enhancement of UV and EUV emission at the footpoints of the newly reconnected loops. The associated rapid heating also leads to the onset of radiative instability and subsequent sublimation of high temperature plasma – manifesting itself as 'chromospheric evaporation' (Mihalas & Winkler, 1986). This heating of the chromospheric plasma causes it to rise and fill the flare loops, creating higher temperatures and densities than surrounding active region loops – causing enhanced EUV and soft X-ray emission.

Oftentimes within the community, these flare loops are referred to as 'post-flare loops'. However, because the loop formation and decay is a part of the solar flare process, we stick to the naming convention of 'flare loops' within this thesis. The pre/post field line configuration above and below the reconnection site are easily seen in the 3D cartoon of Figure 1.11 from Janvier et al. (2013).

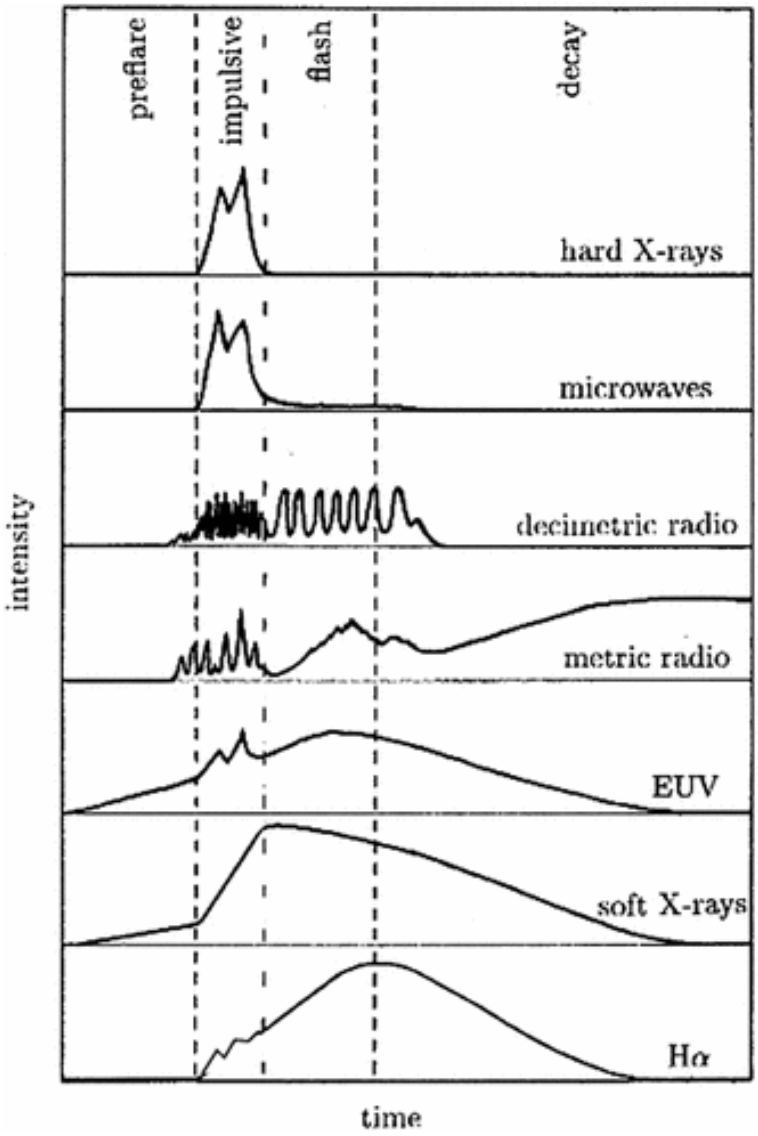

Figure 1.12: Stages of a generic solar flare, categorised by emission across the EM spectrum, (Benz, 2017).

As new field lines reconnect, and the intersection location between reconnected field lines and the chromosphere changes, the bright ribbon areas evolve spatially and temporally. Due to the direct connection between these flare ribbons and the reconnection site, the evolution of the ribbon substructure must directly relate to coronal processes up in the flare and reconnection site (Forbes & Lin, 2000). This is the fundamental premise which the work in Chapter 5 explores.

1.4.2 Flare Timeline

Each solar flare is unique, and thus there is not 'generalised timeline' that can be applied to *every* flare. However, many flares do show consistent behaviour in emission across the EM spectrum, allowing the breakdown of the flare timeline into 3 or 4 main categories (Benz, 2017). The impulsive phase of the flare is the 'main event', named after the impulsive release of energy through the main magnetic reconnection process. The phase is primarily defined by hard X-rays (HXR), bright EUV loops and ribbons. This HXR emission can be either thermal or non-thermal. Thermal HXRs are found at high temperatures in the corona (e.g. at flare looptops), whereas non-thermal HXRs are usually observed within a subset of the flare ribbon footpoints of the reconnected field lines, generated as a result of non-thermal Bremsstrahlung emission as accelerated electrons interact with protons in the background plasma (Kontar et al., 2011; Benz, 2017). Models of solar flares also predict additional non-thermal HXR emission from the collision of accelerated particles at the flare looptops, but these are not observed in every flare. This 'termination shock' is predicted to arise as high energy particles collide with the top of pre-reconnected flare loops (Masuda et al., 1994).

Before the impulsive phase is the 'pre-flare' phase. The search for pre-flare signatures has been a community priority for decades (Woods, 2019), especially due to its relevance to space weather forecasting. Despite this search, pre-flare signatures are subtle, and not reliably detected across all flares. These signals could include EUV enhancements, or an increase in observed velocity within the plasma.

Beyond the impulsive phase, as reconnection ceases, the HXR signal ends soon after. However, the hot EUV loops take much longer to cool down, and so the decay of this EUV emission aptly defines the 'decay' phase of a solar flare. This phase, as we will discover in Chapter 4, is not so easily defined, as reconnection can continue to a lesser degree beyond the impulsive phase of the flare, whilst pre-reconnected loops begin to cool. In fact, flare loops start to cool as soon as they are formed, as they are thermally isolated from newly reconnected loops evacuating the reconnection site above them.

The evolution of expected EM emission across the flare timeline is shown in Figure 1.12 from Benz (2017). This figure shows an additional phase not mentioned here – the 'flash' phase. This flash phase mainly overlaps with the impulsive phase, defined by the peak in Hα emission. This can take place a few minutes later than the peak of the impulsive phase.

These general flare timeline categories exhibit slightly different behaviour for each unique flaring event. Relevant particularly to this thesis is the behaviour of the decay phase. Distinctions have been made in the past between events where this phase is powered solely by the cooling loops (i.e. energy release is no longer ongoing), verses other events where some energy release persists for many hours, albeit at a much slower rate than the initial flare onset (Svestka, 1989). Such events are sometimes referred to as 'dynamic' or 'long-decay' events, and the ongoing energy release is believed to originate from continuing reconnection at much higher altitudes than during the flare's impulsive phase Kahler (1977).

1.4.3 Non-eruptive Flare Models

Not all solar flares are eruptive, and flares/CMEs can be mutually exclusive to one another. The CSHKP model described above is one model in which flares can trigger an eruption, but similarly there are many other models of eruption-less solar flares. We introduce the general concept of one of these models here – due to its relevance later in Chapter 5.

• **Quadrapolar Reconnection -** As is implied in its name, quadrapolar reconnection can occur within active regions containing two positive-negative pairs of strong photospheric magnetic field. In the pre-reconnection state, free energy exists between a pair of active region loops, separately connecting two dipole regions. Current layers can form between these loops, allowing the onset of reconnection. Following this reconfiguration of magnetic topology, a new pair of loops have formed in a lower-energy configuration. Figure 1.13 provides a visualisation of the pre/post reconnection loop configuration, introduced in Melrose (1997).

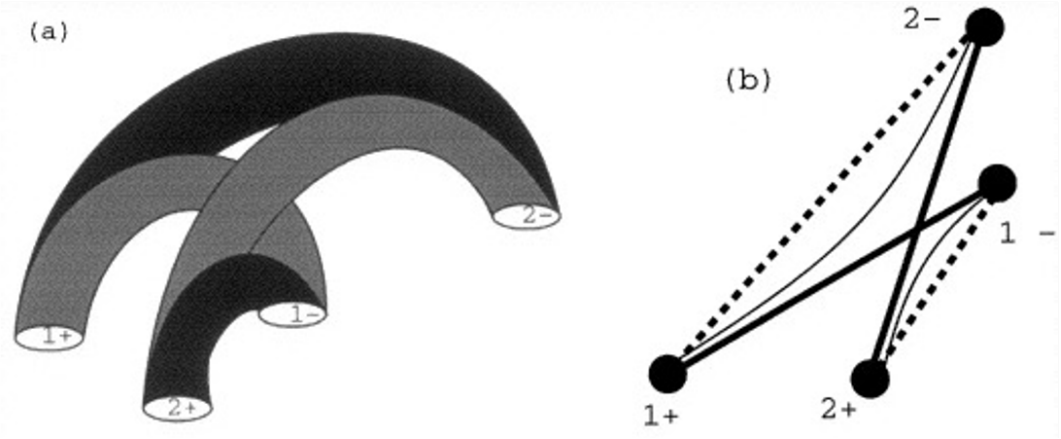

Figure 1.13: Cartoon showing the quadrapolar reconnection model of solar flares (Melrose, 1997). On the left panel, grey and black tubes demonstrate the loop connection before/after reconnection respectively. On the right, this same configuration is shown by the thick and regular solid lines. The numbers label the photospheric regions of positive and negative flux.

1.4.4 Magnetic Reconnection in Flares

The Standard Model is able to account for the majority of observed phenomena in solar flares, but does not directly address the fundamental process of magnetic reconnection itself. Magnetic reconnection has long been thought to be the primary driver of energy release in flares, but its exact nature within the impulsive flare phase is still unclear.

The earliest model of solar reconnection invokes a planar current sheet, in which reconnection takes place along it concurrently (Figure 1.14A). This model, named the 'Sweet-Parker' model after Sweet (1958); Parker (1957), predicts slow reconnection rates that depend on the magnetic Lundquist Number S (Equation 1.20) according to the relation $1/\sqrt{S}$. In the corona, this value is $S \approx 10^{12}$, and so the reconnection rate is far slower than observed energy release in solar flares.

To explain the discrepancy between observed and theoretical energy release rates, the Petschek model of reconnection was introduced in Petschek (1964) (Figure 1.14B). This alternative MHD model invokes fast, steady-state reconnection along a small fraction of the current sheet length, made possible by the inclusion of a slow shock. Petschek's model remains of interest as it was the first to yield reconnection rates fast enough to account for the rapid energy release observed in

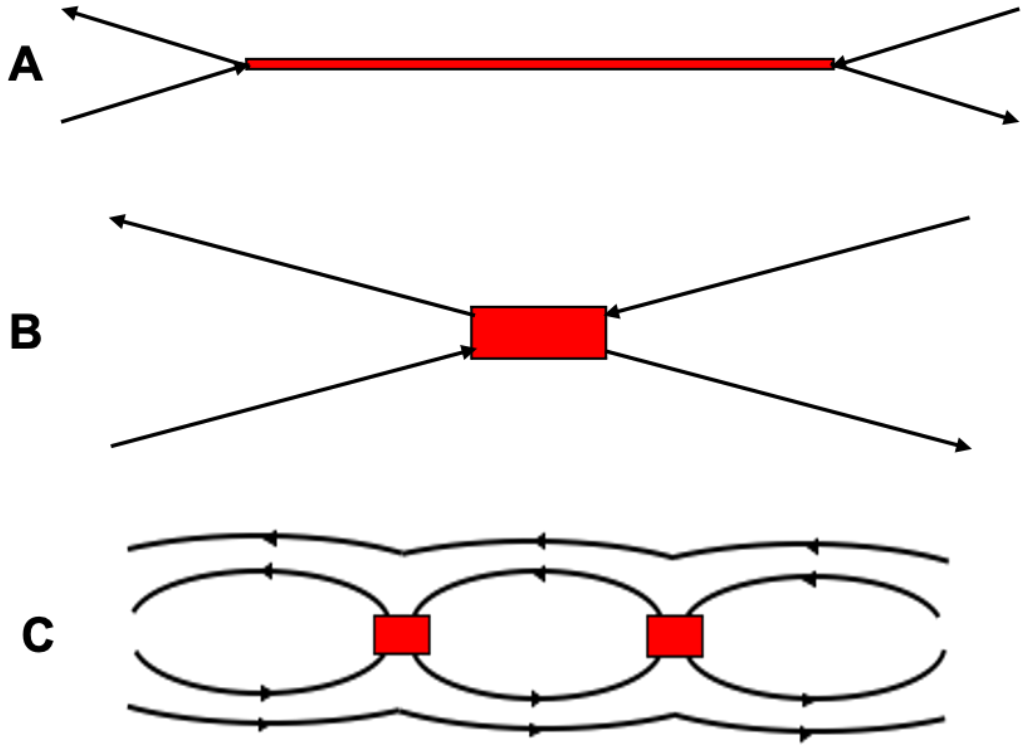

Figure 1.14: Over-simplified cartoon showing the region of reconnection within the current sheet (red) for A: Sweet-Parker Reconnection, B: Petschek reconnection, C: Tearing-mode / plasmoid reconnection.

flares, varying instead as $1/\ln(S)$. Petschek's mechanism assumes a certain large-scale steady configuration, but questions surround how such a configuration might occur, and how/if it is sustained during solar flares (e.g. Kulsrud, 2011). Furthermore, additional physics must be introduced to explain how the plasma is heated, and how electric fields capable of accelerating particles to above MeV energies are generated (e.g. Benz, 2016).

In recent years, attention has been drawn to the possible role of a tearing mode instability, first analysed in Furth et al. (1963). In MHD, if the current sheet length to (MHD) thickness ratio passes a critical threshold (Carbone et al., 1990; Loureiro et al., 2007), the current sheet will 'collapse' or 'tear', forming multiple reconnection X points along the sheet (Figure 1.14C). In 2D, these reconnection sites break the current sheet up into 'plasmoids' or 'magnetic islands', which themselves can continue to collapse under the same tearing instability – creating a cascade down to progressively smaller and smaller spatial and energy scales. Such a configuration

is able to explain the onset of 'fast' reconnection, i.e. at a rate independent of S, in various regimes, and such current sheets were found to be intrinsically unstable to high-wavenumber perturbations, with growth rates greatly in excess of Alfvén crossing times. The tearing mode instability also has a complex relationship with plasma turbulence. Picturing the 2D magnetic island scenario (such as the cartoon in Figure 1.14C), plasma outflows from the cannot flow unobstructed from each of the multiple reconnection sites, as would be possible in a Sweet-Parker or Petschek reconnection scenario. Instead, the plasma outflows from the multiple X points will collide, churning up the plasma and associated frozen-in field. The resulting plasma turbulence can cause further reconnection sites to form, accelerating the further breakdown of the magnetic islands. Island coalescence can also occur, as reconnection occurs at the edge between different magnetic structures within the current sheet (Tenerani & Velli, 2020). Numerical 2D simulations with $S = 10^6$ have supported this general picture of the disruption of reconnecting current sheets through the plasmoid instability (Dong et al., 2018), creating a turbulent cascade with a power spectrum consistent with in-situ observations of plasma turbulence (Shaikh & Zank, 2010).

In 3D, it is harder to visualise the tearing of the current sheet into magnetic island structures at the onset of reconnection. However, simulation work finds 3D 'rope'-like structures, slices along which resemble islands in 2D. An example is presented in Figure 1.15, adapted from Daughton et al. (2011). Just as in 2D, 3-dimensional modelling work of the tearing mode instability have shown the formation of plasma turbulence, reaching an end state with a power law of 2.2 in the spatial domain (Dong et al., 2018; Tenerani & Velli, 2020).

There are many MHD instabilities in plasma physics, but many are not applicable to the plasma conditions in a solar flare. For example, the instabilities causing the breakdown of magnetic field in the Earth's magnetotail (Rae et al., 2010) are not the same processes dominating at equivalent reconnection site's on the Sun. One further instability of interest during flares however, is the Kelvin-Helmholtz instability (Chandrasekhar, 1961; Michalke, 1964; Fejer, 1964). The Kelvin-Helmholtz

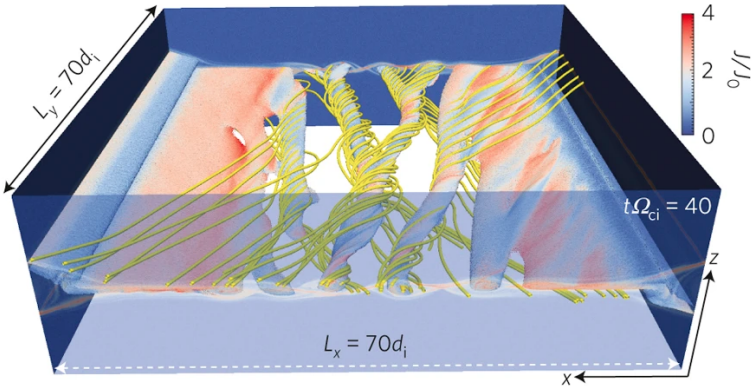

Figure 1.15: MHD simulation of the tearing mode instability in 3D, adapted from Daughton et al. (2011).

instability occurs at the intersection between two fluids layers of different velocities. It is a hydrodynamic instability, and thus can also take place in neutral fluids with no magnetic field (such as in the Earth's atmosphere). In solar flares, the presence of the tearing mode and Kelvin-Helmholtz instabilities are not mutually exclusive. Some studies suggest that the turbulence created by the plasma outflows from the (tearing mode-induced) magnetic island X points is created via the Kelvin-Helmholtz instability (Kowal et al., 2020). This relationship between the tearing mode instability, plasma turbulence and other-related instabilities (such as Kelvin-Helmholtz) during energy release in a solar flare, is an ongoing area of research within the solar physics community.

1.5 Thesis Outline

Magnetic reconnection is the primary driver of energy release in solar flares, predicted to occur within a current sheet of size beneath that of observable limits of modern instrumentation. In the standard eruptive model of flares, this current sheet occurs between the erupting CME and newly-reconnected flare loops, but other flare models contain sheets or layers of current in various configurations. Despite our relative certainty that these current sheets exist, the nature of reconnection within them remains uncertain.

In this thesis, we investigate two solar flares of contrasting sizes, aiming to provide observational evidence of the nature of magnetic reconnection within them.

In particular, we are drawn to the role of the tearing-mode instability within these flares of vastly different magnitudes. The first flare, an X-class event and the second largest of solar cycle 24, is examined in the first two science chapters of this thesis. The second flare, a small B-class event, is examined in the third science chapter. To do this, we use novel methods employing a range of instrumentation, which observe these flares across the EM spectrum. The instruments used in these studies are outlined in the following chapter.

Chapter 2

Instrumentation and Techniques

The work in this thesis uses a wide range of data from a variety of space and ground-based observatories. Some of these instruments, such as the Mauna Loa Solar Observatory (MLSO) Coronal Multi-channel Polarimeter (CoMP), Hinode Extreme-Ultraviolet Imaging Spectrometer (EIS), Solar Dynamics Observatory (SDO) Atmospheric Imaging Assembly (AIA) and Interface Region Imaging Spectrometer (IRIS), form the bulk of the analysis within the three science chapters. Other instruments, such as the Hinode X-Ray Telescope (XRT), SDO Helioseismic and Magnetic Imager (HMI), MLSO K-Cor telescope and Reuven Ramaty High Energy Solar Spectroscopic Imager (RHESSI), provide complementary or supporting analysis. Finally, the Geostationary Operational Environmental Satellite (GOES) is used for context only of a solar flare event. This combination of instruments allows us to sample a range of coronal plasma processes, across large temperature ranges, during solar flares.

This section provides an overview to these instruments, the detail of which will reflect the use of the instrument within this thesis.

2.1 Hinode

The Hinode spacecraft, formally named *Solar-B* prior to its launch in September 2006, orbits the Earth in a Sun-Synchronous Orbit. Hinode is a JAXA mission (in collaboration with the United Kingdom and USA), designed to explore the solar atmosphere and investigate the drivers of solar eruptions. Due to its orbit, Hinode

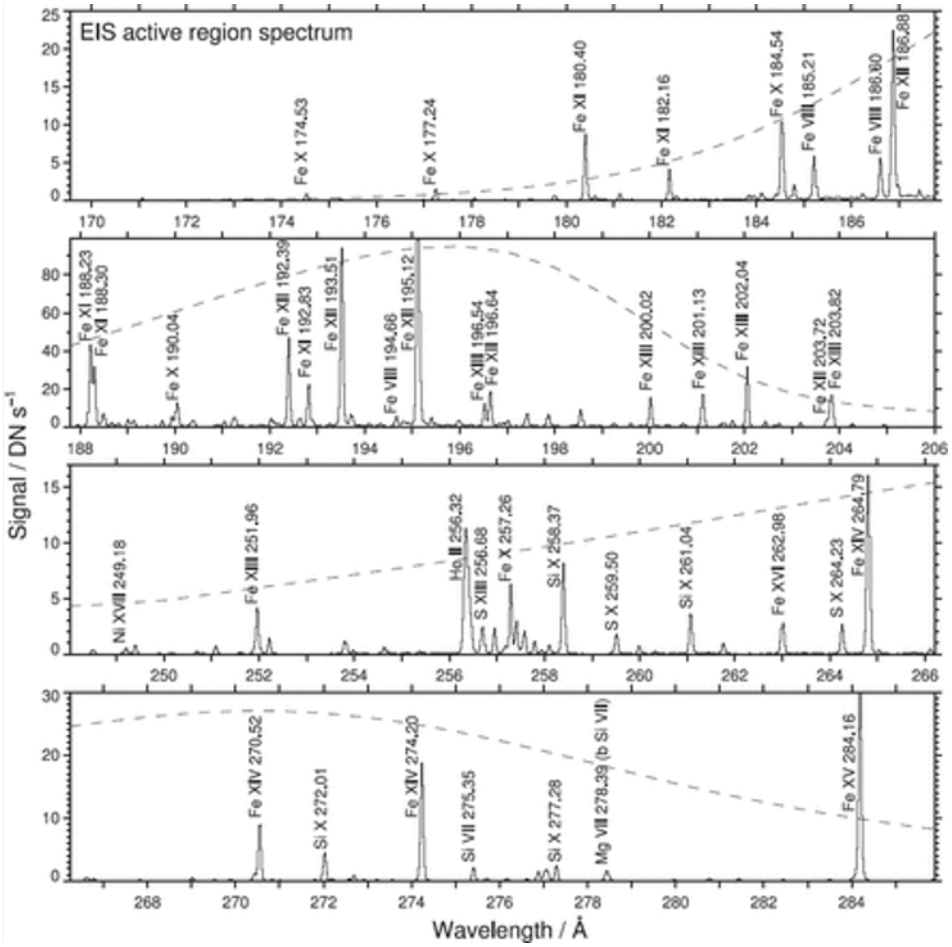

Figure 2.1: Example of a full EIS spectrum for an active region observation, featured in Young et al. (2007).

experiences an 'eclipse season' for three months of the year, where it periodically passes behind the Earth for up to 10 minutes of its 98 minute orbit. The spacecraft consists of three instruments, the Solar Optical Telescope (SOT), X-Ray Telescope (XRT) and Extreme-Ultraviolet Imagine Spectrometer (EIS). The latter two of which are used in this thesis and outlined below.

2.1.1 Extreme-Ultraviolet Imaging Spectrometer (EIS)

Hinode EIS (Culhane et al., 2007) is an imaging slit spectrometer, observing the solar corona and upper transition region over two wavelength regions – 170 Å – 210 Å and 250 Å – 290 Å. The two wavelength windows are observed by two separate detectors - the Short Wavelength and Long Wavelength detectors respectively. Both channels have a maximum spectral resolution of 22 mÅ. An example active re-

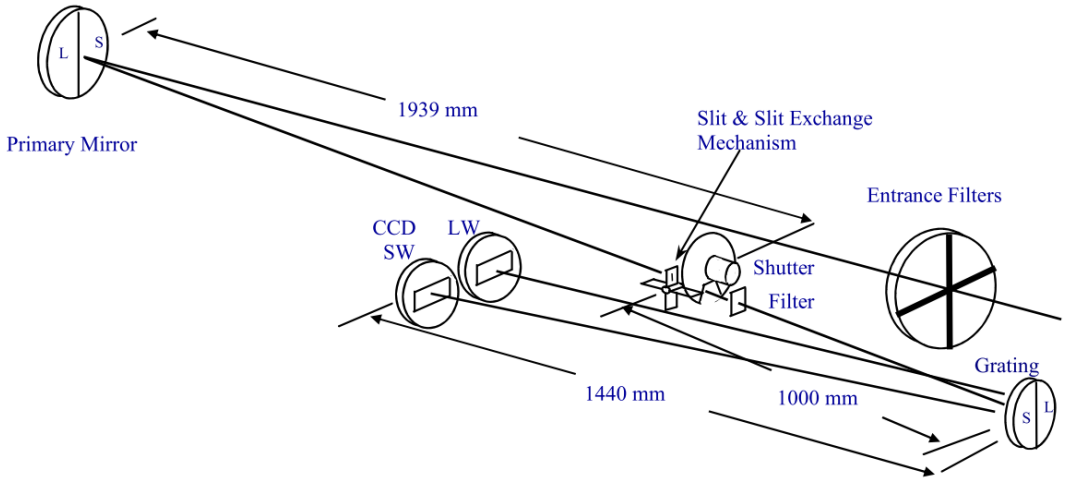

Figure 2.2: Optical layout of the spectrometer, from Culhane et al. (2007). Components are labelled and dimensions are given in mm. S/SW and L/LW refer to short and long wavelength bands.

gion spectrum across the instrument's full wavelength range is shown in Figure 2.1 (Young et al., 2007). The dashed lines show the effective area across the wavelength range.

The slit is orientated to the north-south direction of the Sun, and cannot be rotated. A single exposure will therefore collect spectral data along this vertical slit position. The light enters the entrance window and reflects off the primary mirror before passing through the slit. The light then hits the diffraction grating, reflecting the spectra onto the Short and Long Wavelength detectors. The optical layout of EIS is presented in Figure 2.2. The physical separation between the two CCD detectors produces a slight vertical spatial offset between measurements in the two wavelength ranges (of $\sim 16-20$ pixels). EIS can operate with four slit sizes. Most commonly, the shorter slit sizes of 1 Å or 2 Å are used, but EIS can also observe with larger slit sizes of 40 Å or 266 Å. These larger slit sizes are often referred to as 'slot' observations. To produce an image, EIS systematically rasters the slit horizontally, pausing for each exposure through the vertical slit. The corresponding rastered image contains spectral information for the full FOV, but can be limited in spatial/temporal information. Due to the nature of the rastering slit, there is a time delay from one edge of the image to the other. This requires a careful selection of observing programme, depending on the desired target. If quiescent

features are of interest, then long, large FOV rasters, with total cadence of order an hour, may be suitable. For dynamic structures such as solar flares however, smaller FOV (and limited spectral range) observations are used to reach close to the minimum cadence of ~ 5 minutes. To summarise, there is a trade off between cadence, FOV and sampled wavelength range.

As discussed in the introduction of this thesis, measurements of sufficiently-resolved spectral lines allow the derivation of plasma Doppler velocity, non-thermal velocity, temperature and density. Given the instrument's spectral resolution is several times smaller than the typical width of optically-thin EUV emission lines in the corona, EIS is well suited for this task. Temperature and density can however only be calculated using line ratios from the same detector. The detector sensitivity varies with wavelength (even across a single detector), and the relative degradation of this sensitivity for each detector is not known. There have been calibration attempts to account for this, the most prominent of which are Del Zanna (2013) and Warren et al. (2014).

Before calculating the Doppler and non-thermal velocity of the emitting plasma from the centroid and width of the emission line respectively, we must first account for instrumental effects. The emission line may be artificially broadened, due to the slight scattering of light within the spectrograph and diffraction from the slit. The excess line width is between $0.053 - 0.059$ Å depending on wavelength detector and slit size. The velocity of the spacecraft in its orbit will also induce an instrumental Doppler effect of the spectral line positions. This blue/red shift of the spectral line can be up to the equivalent shift ~ 35 km/s, depending on the location in its orbit relative to the Sun. Both this instrumental line shift and broadening can be accounted for and subtracted during data calibration and preparation.

Previous studies of EIS data have identified an asymmetric point spread function (PSF) of the instrument (Young et al., 2012). This can cause the spill over of photons along the inclination axis of the slit, causing an excess in detected photons on either side of the emission line. This effect is small for regions with low intensity gradients, but far more prominent in observations with sharp intensity boundaries

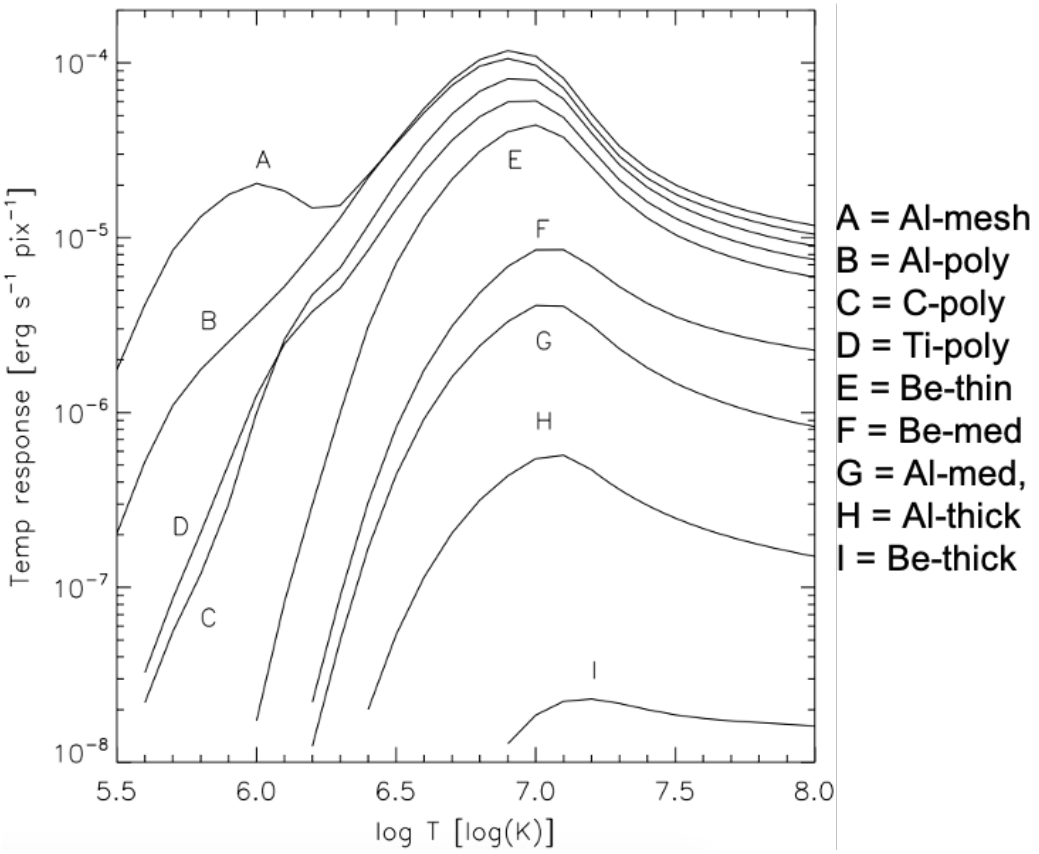

Figure 2.3: Temperature response functions of filters used in the Hinode X-Ray Telescope (XRT), adapted from Golub et al. (2007).

(e.g. objects at the limb). This is because the spill over from bright pixels can significantly increase the blue or red wing of lower intensity pixels – artificially shifting the observed line centroid. A major result of this is then systematic artefacts may exist in Doppler Velocity maps of bright off-limb structures (Warren et al., 2018).

2.1.2 X-Ray Telescope (XRT)

The Hinode X-Ray Telescope (XRT, Golub et al., 2007) is a grazing-incidence X-ray telescope, sensitive to plasma in the 1 – 20 MK range. As light passes the entrance filter, grazing-incidence optics focus the soft X-rays onto the CCD array, through the two filter wheels. The entrance filter is to block unwanted visible light from entering the telescope, but allow soft X-rays to pass. The second two filter wheels are positioned in series within the optical path, and vary in thickness to provide multiple X-ray passbands, sensitive to varying temperature ranges. Thin filters are used for quiet Sun targets, whereas thick filters are used to observe flaring

regions. The list of XRT passbands (produced by the combination of two filters), and their temperature response, are shown in Figure 2.3. Since Hinode's launch, damage to the entrance filter has left some of these filter combinations unusable for science observations, due to visible-light contamination (Hinode Review Team et al., 2019).

2.2 SDO

The NASA Solar Dynamics Observatory (SDO) was launched on February 11th 2010, with the primary goal of studying solar activity. The spacecraft sits in a geostationary orbit above its ground station in New Mexico, to allow continuous and uninterrupted observations of the Sun. SDO has three instruments onboard, the Atmospheric Imaging Assembly (AIA), Helioseismic and Magnetic Imager (HMI) and EUV Variability Experiment. AIA is used throughout this thesis, and HMI is used briefly in Chapter 5. These are introduced below.

2.2.1 Atmospheric Imaging Assembly (AIA)

Channel	Primary ion(s)	Region of atmosphere	Char. log(T)
4500 Å	continuum	photosphere	3.7
1700 Å	continuum	temperature minimum, photosphere	3.7
304 Å	He II	chromosphere, transition region	4.7
1600 Å	C IV + cont.	transition region, upper photosphere	5.0
171 Å	Fe IX	quiet corona, upper transition region	5.8
193 Å	Fe XII, XXIV	corona and hot flare plasma	6.2, 7.3
211 Å	Fe XIV	active-region corona	6.3
335 Å	Fe XVI	active-region corona	6.4
94 Å	Fe XVIII	flaring corona	6.8
131 Å	Fe VIII, XXI	transition region, flaring corona	5.6, 7.0

Table 2.1: Table from Lemen et al. (2012), showing ion and temperature sampling range of each AIA passband.

The Atmospheric Imaging Assembly (AIA, Lemen et al., 2012) is a broadband imager, observing the Sun through ten different broadband filters. These include seven EUV passbands (94 Å, 131 Å, 171 Å, 193 Å, 211 Å, 304 Å and 335 Å), centred around prominent spectral emission lines in the solar corona, two UV passbands (1600 Å and 1700 Å), primarily observing the chromospheric continuum,

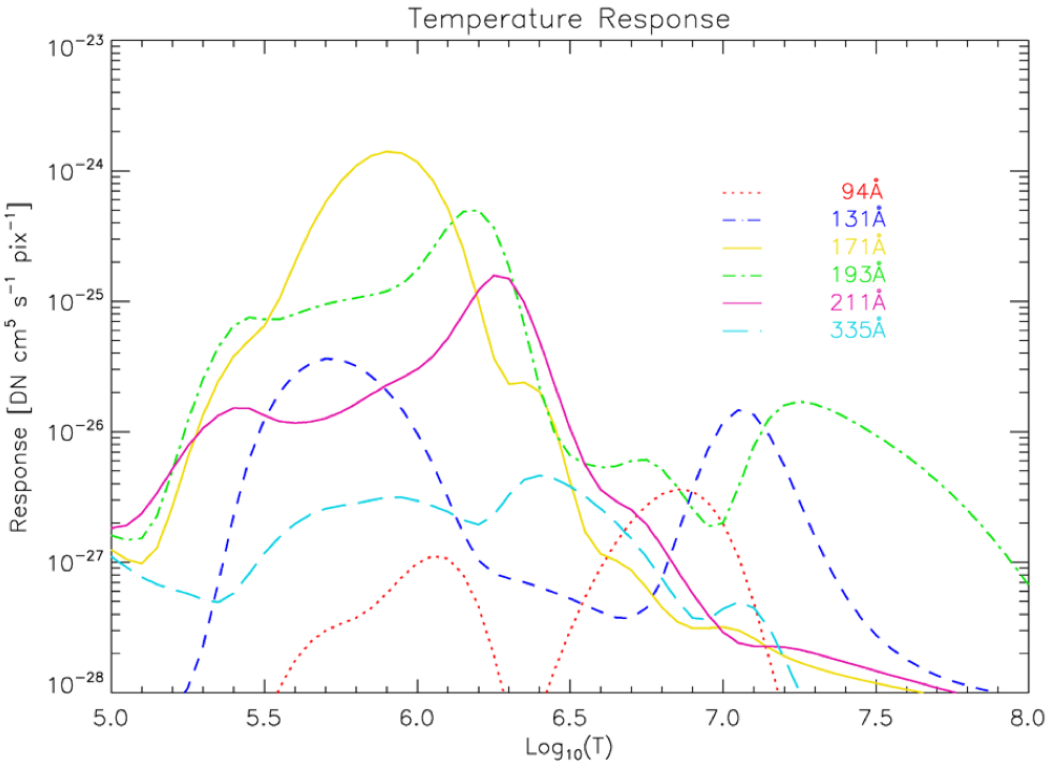

Figure 2.4: Temperature response of each Fe-dominated AIA passband, from Boerner et al. (2012).

and one visible light passband (4500 Å), observing the photospheric continuum. The seven EUV passbands were chosen to sample a range of atmospheric temperatures, providing a measurement of coronal plasmas from quiet Sun to X-class flares. Table 2.1 provides a list of AIA passbands, their primary ion (or continuum) observed, with the characteristic temperature of this ion/continuum wavelength and corresponding region of the atmosphere. However, this table does not reveal the full picture. Due to the nature of a broadband imager, there will be additional emission contributions beyond that of the primary observed ions, meaning the plasma temperatures observed by a specific passband will not have as clear a single peak as the contribution function from a single ion. The temperature response of the six EUV passbands, which have a primary contribution from Fe ions, are shown in Figure 2.4.

Unlike EUV spectrometers (such as Hinode EIS), EUV imagers are unable to reveal information on LOS velocity or line width. However, a major advantage of an

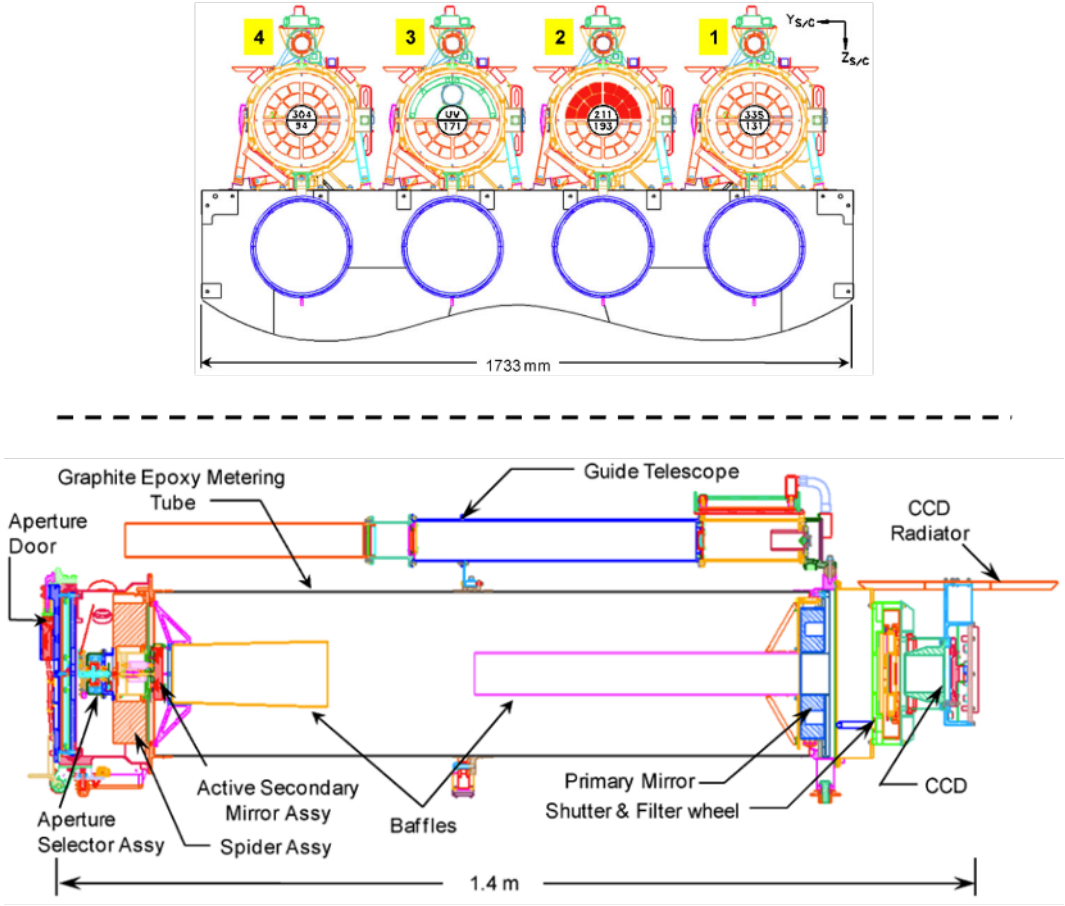

Figure 2.5: Schematic of the AIA instrument, from Lemen et al. (2012).

imager is the ability to take cotemporal images over a large FOV with high cadence. AIA does this effectively, capturing 4096 $\times$ 4096 resolution images of the full solar disk (up to 1228.8 $''$), every 12 seconds, in each of its UV and EUV passbands.

AIA achieves such high cadences by observing with four Cassegrain telescopes simultaneously. The top panel of Figure 2.5 shows the relative position of these four telescopes, each with a filter wheel rotating between its share of the broadband filters. As with a standard Cassegrain telescope, after entering through the filter wheel, the filtered light bounces off the primary mirror at the base of the telescope, reflecting again off the secondary mirror, before reaching the CCD. This optical path is shown in the bottom panel of Figure 2.5.

2.2.2 Helioseismic and Magnetic Imager (HMI)

The Helioseismic and Magnetic Imager (HMI, Schou et al., 2012) measures the intensity, Doppler velocity and vector magnetic field of the photospheric Fe I 6173 absorption line, with 4096 $\times$ 4096 resolution. The refracting telescope sits behind a filter (to block the majority of sunlight), where the primary and secondary lens refract the light through focus and calibration mechanisms to the polariser. The polariser rotates between the polarisation states, and the polarised light passes through further tuning steps before being split onto two detectors. One detector observes the Doppler shift of the line, whereas the other measures the polarisation information to determine the vector magnetic field. In this thesis, we use only HMI LOS magnetic field measurements, which are determined from the observed circular polarisation (Stokes V). HMI can observe these LOS magnetic field measurements with a high cadence of 15 seconds.

2.3 Interface Region Imaging Spectrometer (IRIS)

The Interface Region Imaging Spectrometer (IRIS, De Pontieu et al., 2014) is a single instrument NASA Small Explorer Mission, launched in June 2013, and designed/operated by the Lockheed Martin Solar and Astrophysics Laboratory. Similar to Hinode, IRIS sits in a Sun-Synchronous orbit, and thus experiences eclipses for four months of the year, making observations impossible for up to 37 minutes of each $\approx$ 97 minute orbit.

IRIS consists of a UV spectrograph with a slit-jaw imager (SJI), designed to study the chromosphere and transition region. IRIS collects spectra in two far UV (FUV) and one near UV (NUV) wavelength ranges. The FUV 1 range spans 1332 Å – 1358 Å, containing the bright C II 1334.5 Å and 1335.7 Å lines. FUV 2 spans a wavelength range of 1389 Å – 1407 Å, including the Si IV 1394 Å and 1403 Å lines. Finally, the 2783 Å – 2834 Å NUV range includes the Mg II h/k lines at 2803 Å and 2796 Å respectively. The spectral slit is 175$''$ high, which, unlike the slit in Hinode-EIS, is able to rotate away $\pm$90° from the N-S direction of the Sun. For the FUV wavelength ranges, the IRIS slit has a 0.33$''$ spatial resolution and 26

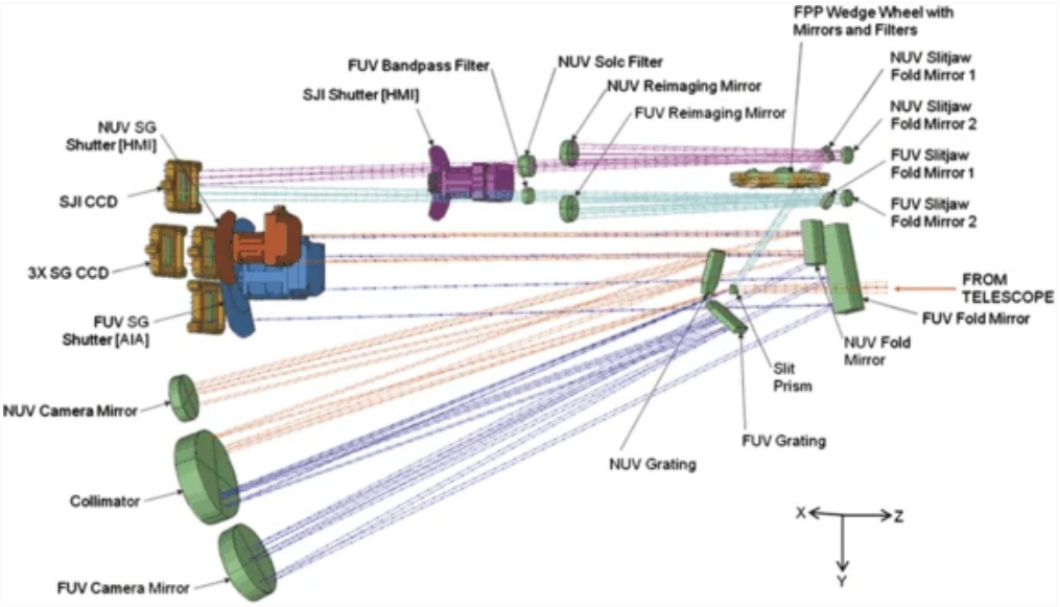

Figure 2.6: Optical path of the IRIS instrument, from De Pontieu et al. (2014).

mÅ spectral resolution. For the NUV wavelength range, these values are $0.4''$ and 0.53 mÅ respectively. The slit can observe with either a sit-and-stare routine, or raster with various step sizes to create a rastered image. As with all spectrographs, there is a trade off between cadence and spectral/spatial range and resolution. By heavily restricting the wavelength range, a sit-and-stare routine can be pushed to a maximum cadence of ≈ 1.6 seconds.

The SJI provides context for the spectral data, imaging up to a 175 Å $\times$ 175 Å FOV, centred on the slit position. The SJI includes four broadband passbands, centred on a single spectral line from the FUV and NUV detectors. These are C II 1335 Å, Si IV 1400 Å (both sampling the transition region), Mg II k 2796 Å (sampling the chromosphere) and Mg II wing 2830 Å (sampling the photosphere).

The optical path of IRIS is shown in Figure 2.6 (De Pontieu et al., 2014). As light enters the 19 cm Cassegrain telescope, it reaches the slit. Light passing through the slit is dispersed by either the NUV or FUV grating, and collected by the three CCDs covering the FUV 1, FUV 2 and NUV wavelength ranges. Light that does not pass through the slit is reflected by a reflective area around the slit (the slit-jaw imager), which then passes through the broadband filters onto the SJI CCD. The filters are rotated on a filter wheel.

2.4 Mauna Loa Solar Observatory (MLSO)

The Mauna Loa Solar Observatory (MLSO) is situated on the mountain of Mauna Loa in Hawaii, as a part of a wider research site. The Observatory is operated by the NCAR (National Center for Atmospheric Research) High Altitude Observatory (HAO). The goal of the MLSO telescopes are to study the formation and dynamics of CMEs and density structures in the low corona. MLSO currently has two telescopes operational – K-Cor and UCoMP. UCoMP has only been operational since 2021, and is an upgrade of its predecessor, CoMP, which ceased observations in 2018. In this thesis we use data from both CoMP and K-Cor, both of which are outlined below.

2.4.1 Coronal Multi-channel Polarimeter (CoMP)

The High Altitude Observatory's Coronal Multi-channel Polarimeter (CoMP, Tomczyk et al., 2008) was a 20 cm coronagraph located at the Mauna Loa Solar Observatory. CoMP measured the corona in the infrared from 1.03 - 1.5 solar radii ($R_{\odot}$). CoMP was fitted with a spectrograph, measuring 3-7 wavepoints around the 1074.7 nm and 1079.9 nm Fe XIII coronal forbidden lines, and He I 1083.0 nm chromospheric line, each through a filter of roughly Gaussian shape (FWHM of 1.3 Å). CoMP sacrificed spectroscopic resolution in order to take spectropolarimetric measurements of linear (Stokes U & Q) and circular polarisation (Stokes V), as well as intensity (Stokes I). Although there were daily observing programmes attempting to measure Stokes V, the signal-to-noise ratio was just too low to obtain usable data, with the added problem of cross-talk from other polarisation channels. CoMP observed with a spatial pixel size of $4.35''$ and maximum cadence of 30 s. Maximum cadence occurs when only 3 wavepoints are measured for each spectral line. Similarly to EUV spectrometers such as EIS and IRIS, the spectral line profile can provide insight into the Doppler velocity and non-thermal velocity. As expected, the associated uncertainty of these velocity measurements are far larger for the 3 wavepoint measurements, compared with the full 7 wavepoints (even this is low compared to dedicated spectrometers). The benefit of CoMP was instead the polarisation measurements of the corona. As discussed in section 1.2.3, linear

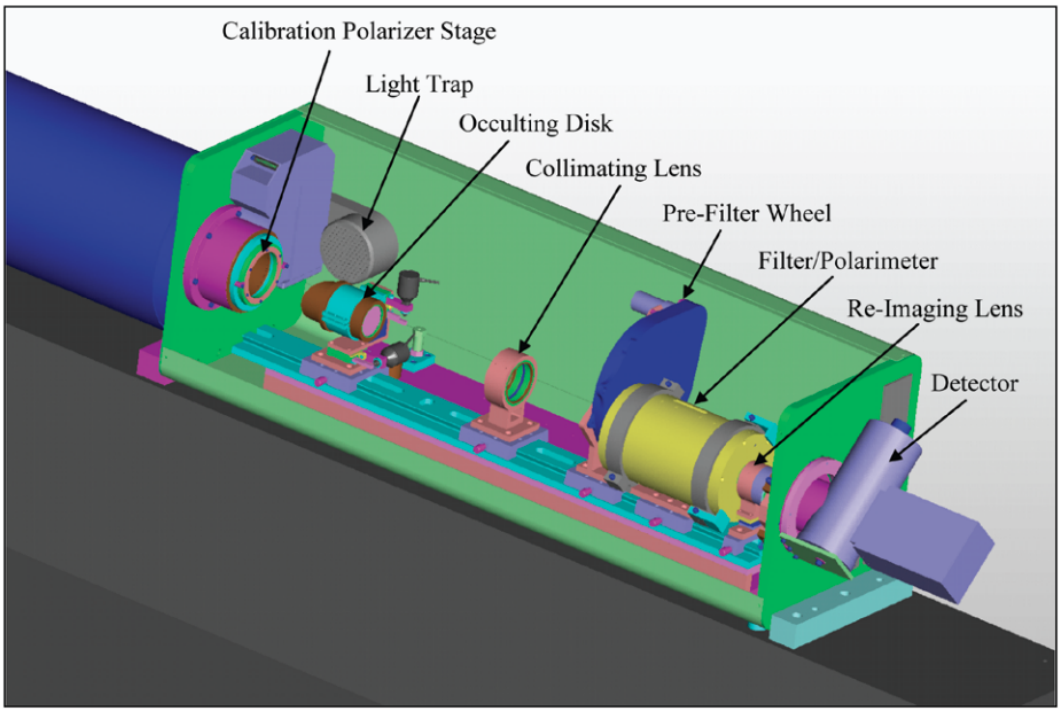

Figure 2.7: Diagram of the CoMP instrument, with light entering from the blue tube on the left, (Tomczyk et al., 2008).

polarisation depends on the orientation of coronal magnetic fields, allowing the investigation of magnetic fields within the coronal structures. Coronal densities can also be calculated, as the observed Fe XIII lines form a density-sensitive pair.

Figure 2.7 shows the components of the instrument within the optical path. Light passes through the 20cm aperture and reaches the occulting disk, a solid disk with a height of 1.03 $R_\odot$ (determining the inner FOV). The occulting disk blocks light from the Sun's surface, allowing only coronal emission to pass through. The light then passes through a collimating lens to a pre-filter wheel, with three filters for the three target emission lines. The pre-filtered light then passes through the filter and polarimeter. The tunable filter shifts to the different wavelengths, to measure emission at the desired wavepoints across the emission line (minimum of three). For light at a given wavepoint, it passes through the polarising beam splitter, which splits the polarised and unpolarised light to observe the continuum and line polarisation simultaneously. In an observing routine to measure linear polarisation, the polariser switches between angles of 0°, 90°, 45° and 135°, to measure the po-

larisation states of $I+Q$, $I-Q$, $I+U$ and $I-U$ respectively. An observation of unpolarised light I is also measured without the polariser.

2.4.2 K-Cor

K-Cor is a white-light coronagraph, consisting of a refracting telescope with a 20 cm aperture. Light enters the telescope, and is focused by the objective lens. As light travels towards the focus, it reaches the occulting disk, allowing only photons from the edge of the FOV to pass. The occulting disk has a height of 1.15 $R_{\odot}$, with a maximum FOV of 3 $R_{\odot}$. Light from around the occulting disk is focused through a bandpass filter, past a Lyot stop (an optical component designed to limit stray light, Lyot, 1939) to the polarising beam splitter. The split light reaches two independent, 'off-the-shelf' cameras. One measures the polarised light (polarised brightness, pB), and the other the unpolarised white light. Blocking out the white light from the photosphere itself, the observed polarised brightness photons originate from the scattering of photospheric light from free electrons in the corona. This scattering process is described in the introduction to this thesis. K-Cor has a spatial pixel size of 5.5″ and standard 15 s cadence.

2.5 Reuven Ramaty High Energy Solar Spectroscopic Imager (RHESSI)

RHESSI was a NASA Small Explorer mission, with a primary objective to study particle acceleration and energy release in solar flares. The spacecraft launched in February 2002, and lived far beyond the initial mission timeline until observations finally ended in April 2018. RHESSI observed hard X-rays and gamma rays on the Sun from 3 keV to 17 MeV, performing both imaging and spectroscopy with high resolution. RHESSI measured these high energy wavelengths using germanium detectors behind a Rotating Modulating Collimator. The Collimator consists of two vertical grids in parallel. As off-axis photons pass through the grid, they cast a shadow on the detector. The collimators rotated (enabled by the rotation of the entire spacecraft) once every four seconds, causing the photon source to pass in

and out of the shadow at various points in the detector. The detector is made up of 9 cryogenically-cooled co-axial germanium detectors (which can be much thicker than their silicon counterparts) – thick enough to totally absorb gamma rays of a few MeV.

In this thesis, we use imaging from the RHESSI instrument. There are several automated algorithms available to reconstruct the data into an image. The routine used in this work is 'Clean', which reconstructs an image from photons passing through the Rotating Modulating Collimator under the assumption that the image consists of a superposition of point sources.

2.6 GOES X-Ray Sensor (XRS)

The Geostationary Operational Environmental Satellite (GOES) system is a network of satellites in geostationary orbit, primarily designed for Earth observation. GOES satellites also include a solar X-Ray Sensor (XRS) to monitor solar soft X-Ray (SXR) emission for space weather forecasting purposes. These SXR measurements that determine the classification of solar flares. SXRs are measured in the 0.5 Å – 4.0 Å and 1.0 Å – 8.0 Å wavelength ranges, but it is the latter used for flare classification. Table 2.2 below lists the SXR flux thresholds for each flare class.

Flare Class	SXR Flux (W m^{-1})
B	10^{-7} – 10^{-6}
C	10^{-6} – 10^{-5}
M	10^{-5} – 10^{-4}
X	$> 10^{-4}$

Table 2.2: GOES SXR definitions of solar flare classes

2.7 Techniques

Throughout the following three science chapters, a variety of methodologies and techniques are used to analyse datasets from the above instruments. The majority of these techniques are described within the relevant chapters as they arise. Below, we introduce the methodology behind Differential Emission Measures, the output from which are utilised in Chapter 4.

2.7.1 Differential Emission Measures

As explored in section 1.2.2, the ratio of emission lines can be used to calculate the temperature of the emitting plasma. This method does, however, come with limitations. Because the observed emission is integrated along the LOS, by calculating a single temperature we are assuming the received radiation in the LOS is coming from an isothermal source. This assumption may seem like an unjustifiable one at first, especially for observations on the solar disk, where our LOS contains emitting plasma with temperatures and densities spanning orders of magnitude. However, emission lines themselves have a temperature dependency (based on their contribution function), and so may only emit strongly over narrow temperature ranges. The assumption of an isothermal source dominating the emission within this narrow temperature range is no longer such a leap, especially when observing isolated higher altitude structures (e.g. active region loops), or features off the limb. But it is worth remembering that such assumptions still exist.

However, with instruments such as AIA sampling such vast temperature ranges with multiple broadband channels, further methods exist to disentangle the emission contribution from different temperature plasmas within the LOS. For a given AIA passband i, the measured intensity y_i can be considered as:

$$y_i = \int_0^\infty K_i(T) DEM(T) dT, \tag{2.1}$$

where K_i is the passband temperature response function, as presented in Figure 2.4, and DEM(T) the differential emission measure of plasma sitting in the LOS (with units of $\mathrm{cm}^{-5}\mathrm{K}^{-1}$). For EUV emission created from collisional excitation within the plasma, the differential emission measure is determined by:

$$DEM(T)dT = \int_0^\infty n_e^2(T) dz, \tag{2.2}$$

i.e. it is dependent on the electron density squared at a given temperature, integrated along the LOS. By breaking down the integral from Equation 2.1 into discrete temperature bins (e.g. of size 0.5 log(K)), it is possible to invert the signal y_i from each

AIA passband to determine the relative emission of plasma at different temperatures. DEMs can be constrained even further by including Hinode EIS and XRT intensities with the AIA passband data. Computing the DEM inversion, especially from AIA data alone, is an ill-posed problem. Different methods have been made available within the community to calculate the DEMs of the solar corona, but in this thesis we use output from the 'regularised inversion' method described in Hannah & Kontar (2013).

Chapter 3

Spectropolarimetric Insight into plasma sheet Dynamics of a Solar Flare

This chapter primarily includes work from French et al. (2019), as well as some additional introductory material and unpublished work from an ongoing study.

3.1 Introduction

Magnetic reconnection is believed to lie at the heart of energy release in solar flares. However, the precise mechanisms through which reconnection occurs in flares are still uncertain. In order to explain the breakdown of ideal magnetohydrodynamics (on small spatial scales) needed to enable fast magnetic reconnection in the current sheet (leading to solar flare onset), recent attention has turned to the role of the tearing-mode instability (Biskamp, 1986, section 1.4.4). In the tearing-mode instability, a classic Sweet-Parker current sheet reaches an unstable aspect ratio, collapsing and reconnecting at multiple points along the sheet to form magnetic islands, or plasmoids. These magnetic islands form at a preferred spatial scale, and continue to collapse further to produce islands at progressively smaller scales. Larger islands are also produced via the reconnection and coalescence at island boundaries (Tenerani & Velli, 2020). This critical aspect ratio and spatial scales are dependent on the local magnetic conditions, in particular the Lunduist number. The cascade to

smaller island scales is predicted to produce plasma turbulence, with a power-law similar to those observed in in-situ plasmas (Shaikh & Zank, 2010). The exact relationship between the tearing-mode instability and turbulence within a reconnecting current sheet is still a prominent area of ongoing research.

In the corona, current sheets are predicted to occur with a width of order 10 m (Litvinenko, 1996), far below the observable limit of even the best coronal instruments ($\approx$ 200 km). However, rare sheet-like regions of hot plasma have been observed, associated with eruptive flares and appearing to be related to reconnection within a current sheet (e.g. Liu, 2013). These '*plasma* sheets' are elusive and notoriously difficult to identify, most readily seen above the solar limb.

In this chapter, we examine spectropolarimetric data from the CoMP instrument (section 2.4.1), acquired during the evolution of the 10th September 2017 X8.2 solar flare on the western solar limb – which featured one of the brightest and longest-lived plasma sheet structures observed to date. Using CoMP, we present observational evidence for the presence of unresolvable magnetic structure, consistent with the plasmoid-fragmentation picture within a dynamically evolving current sheet in the wake of a coronal mass ejection. We show that the magnitude of linear polarisation is sensitive to these unresolvable small-scale magnetic structures.

3.2 The 10th September 2017 flare

The 10th September 2017 flare has become one of the most studied solar flares of all time. At the time of its eruption, Solar Cycle 24 was plummeting towards solar minimum, and the flare's source region AR 12673 was the only region of interest on the solar disk. As a result of this, the majority of limited-FOV solar instruments were pointing at the active region during some phase of the flare's long evolution. The flare was thus observed across the entire EM spectrum by multiple space-based and ground-based instruments, and has resulted in 78 publications to date.

The X8.2-class flare erupted on the western solar limb at 15:44 UT, with its footpoints partially occulted as it rotated off disk. Figure 3.1 shows snapshots of the flare's evolution within the first few hours, as seen by the broadband AIA 193

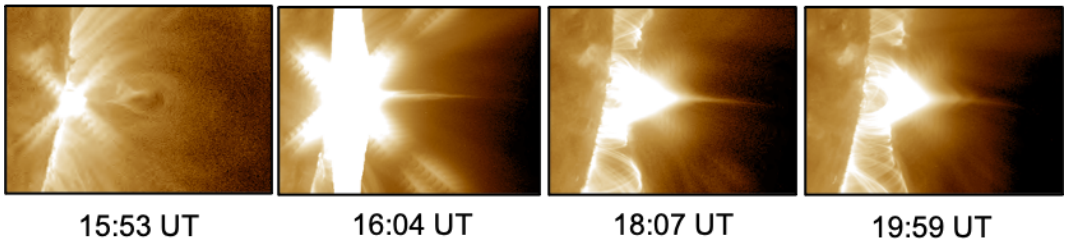

Figure 3.1: Snapshots of the 10th September 2017 flare evolution, as seen by the AIA 193 Å channel.

Å channel. As the flare erupts, we see a clear profile-view of cavity associated with the flare's CME (Long et al., 2018; Morosan et al., 2019). The edge-on vantage point of the eruption shows clear similarities to the classic CSHKP 2D model of solar flares, e.g. that in Figure 1.10. As the CME and associated flux rope erupt, behind it we observe a laminar sheet of hot plasma, which stretches all the way into the LASCO FOV. This plasma sheet is particularly striking in EUV, as seen in panels 2-4 of Figure 3.1. Behind the plasma sheet we see the formation of a large flare loop (Kuridze et al., 2019), with smaller loops to the north and south. Despite its similar appearance to the 2D model, the flare is of course three dimensional. It is the orientation of the eruption that simply gives us the edge-on view of the eruptive cavity – creating its likeness to 2D models. Chen et al. (2020) found that the event also fits nicely to the classic 3D model of eruptive flares (Aulanier et al., 2012, 2013; Janvier et al., 2013, 2014), such as in the cartoon in Figure 1.11. Chen et al. (2020) determined that the plasma sheet is sitting above the underlying arcade along (and arching over) the east-west inversion line in the LOS. The plasma sheet extends to lower altitudes in the foreground, and is briefly visible above the continuation of the arcade in the north-south direction (at the footpoints of the erupting flux rope), to the south of the primary flare arcade (Cai et al., 2019). The bright plasma sheet we see in EUV is thus not a thin structure, but a view of integrated emission along our LOS above the main flare arcade.

With a plethora of interesting phenomena observed within the flare, it is the plasma sheet in particular that we investigate during this chapter. Due to high temperatures and enhanced line widths in the region (Warren et al., 2018), the plasma

sheet has been interpreted as hot, turbulent plasma, enclosing the current sheet at the site of magnetic reconnection. Warren et al. (2018) used EIS and AIA data to study the spectroscopic evolution and structure of the plasma sheet. Using temperature sensitive EIS lines, they calculated a mean plasma sheet temperature of 15-20 MK. Li et al. (2018) and Warren et al. (2018) investigated non-thermal broadening of spectral lines within the plasma sheet, finding non-thermal velocities as high as 200 km s^{-1}. The highest line widths (measuring velocities of plasma superposed along the LOS) were seen first at the base of the plasma sheet, later they shifted to higher altitudes. The broad lines were hypothesised to indicate small-scale turbulent velocity fluctuations from plasmoid fragmentation during reconnection. In support of this idea, Cheng et al. (2018) analysed the plasma sheet POS outflows, finding a power-law spectrum of fluctuations in wavenumber space consistent with a turbulent cascade of energy toward smaller scales. Quasi-periodic pulsations have also been reported (Longcope et al., 2018; Cheng et al., 2018; Hayes et al., 2019) within the plasma sheet structure. Many of these observations, in particular the high non-thermal velocities and evidence of plasmoid fragmentation, are interpreted as evidence for the presence of the tearing mode instability within the plasma sheet.

However, although EUV observations can provide indirect evidence for the presence of plasma instabilities, they cannot provide clear insight into the nature of the sheet's magnetic field structure, which ultimately is the key driver of reconnection and corresponding onset of turbulence. More direct observations of the magnetic field may be a crucial clue to the understanding of magnetic reconnection in this and similar events. Fortuitously, the CoMP instrument obtained polarisation data of the plasma sheet, albeit late into the flare's evolution. It is the striking and coherent (and surprisingly-low) polarisation structure of the plasma sheet that we investigate in this chapter.

3.3 Observations

The 10th September 2017 flare peaked at 16:06 UT on the western limb. Here we introduce observations from the Coronal Multi-channel Polarimeter (CoMP, section

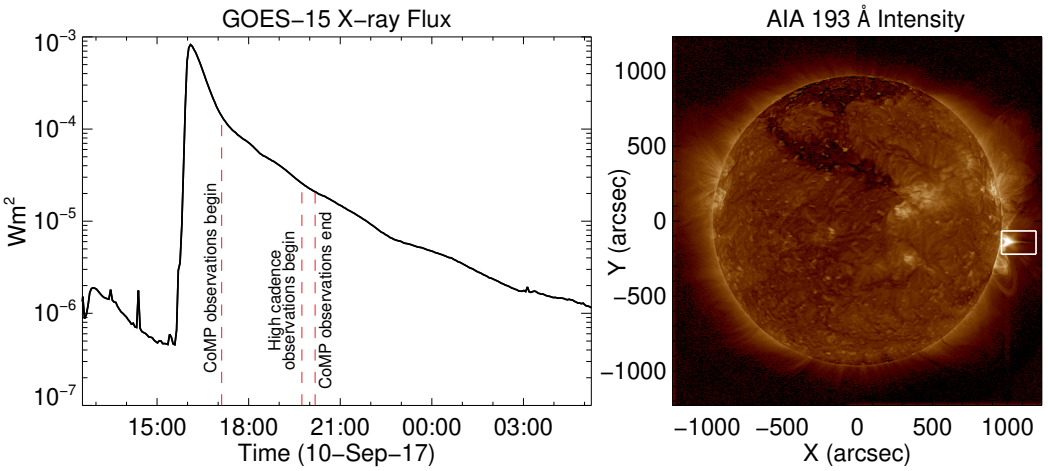

Figure 3.2: Left: GOES-15 X-ray flux for the flare, displaying CoMP observing times. Right: Location of the plasma sheet FOV used in this study.

2.4.1), which observed on 10th Sept 2017 between 17:07:50 and 20:10:36 UT. The CoMP instrument has an aperture of 20 cm and uses a coronagraph to observe the low corona from ∼1.03 to 1.5 $R_\odot$. CoMP measures the intensity and linear polarisation (Stokes I,Q,U) of infrared Fe XIII 1074.7 nm and 1079.8 nm lines, with a formation temperature of ∼1.5 MK. As described in the instrumentation section, CoMP has multiple observing modes – in which it can sample the two Fe XIII lines with either 3-7 wave points each. 48 of the 62 observations from 10th Sept 2017 occurred between 19:44:36 and 20:10:36 UT with the higher-cadence 3-wavepoint scan, producing observations with a 30 second cadence and 4.35″ spatial sampling. CoMP observing times are shown in the left panel of Figure 3.2.

The K-Cor instrument at the Mauna Loa Solar Observatory also observed the event, measuring white light polarisation (pB) from 1.05 to 3 $R_\odot$ over the same full observing duration as CoMP. K-Cor has a lower resolution than CoMP (spatial sampling of 5.64″) but a higher cadence of 15 s.

EUV observations by AIA onboard the Solar Dynamics Observatory (SDO) provide context imagery, with a higher cadence (∼ 12 seconds) and considerably higher spatial resolution (0.6″). The plasma sheet is most visible in the 193 Å passband, primarily sensitive to emission from both Fe XXIV and Fe XII. Given the plasma sheet's high temperature, the observed emission likely contains signifi-

cant contribution from the 20 MK Fe XXIV line. Despite its high temperature, the plasma sheet is also seen in cooler AIA passbands, such as 211 Å (Warren et al., 2018), dominated by plasma closer to 2 MK. In unprocessed AIA 193 Å observations, the plasma sheet is clearly visible from 16:06 to beyond 20:30 UT. Therefore, although the higher cadence CoMP observations start 3 h 38 m after the flare peak, the plasma sheet is still visible in EUV observations during this time. This is much longer than the Alfvén crossing time, which is just a few minutes for a magnetic field strength of 10 G. The full lifetime of the plasma sheet is explored in the next chapter, Chapter 4.

Figure 3.3A shows AIA 193 Å observations of the plasma sheet, averaged over a later portion of the total CoMP observing period (18:00 - 20:00 UT), and processed using the Multi-Gaussian Normalisation (MGN) technique (Morgan & Druckmüller, 2014). In this image, the plasma sheet is seen as the bright horizontal structure, located above the saturated flare loop. A diffraction pattern from saturated intensities is also visible, as a faint cross emanating from the flaring region. The location of this field of view (FOV) is shown in Figure 3.2B.

3.4 Spectropolarimetry

Linearly polarised radiation is created by the scattering of anisotropic radiation from the solar surface by coronal plasma. The anisotropic radiation generates unequal populations of magnetic sub-states, (*atomic* polarisation), dependent on the local thermal and magnetic conditions of the plasma (Charvin, 1965). The atomic polarisation of Fe XIII is, to within a few percent, proportional to the factor $3\cos^2\theta_B - 1$, where θ_B is the angle between the magnetic field vector and direction of the centre of the incident radiation (equation 45 of Casini & Judge (1999), Judge (2007)). The level of atomic polarisation therefore depends on the local magnetic field orientation and radiation field. This atomic polarisation can be destroyed by isotropic processes, including collisions by a sufficiently high density of thermal electrons and protons. This adds a further density dependence to the level of polarisation.

The emitted radiation is linearly polarised by a factor proportional to the

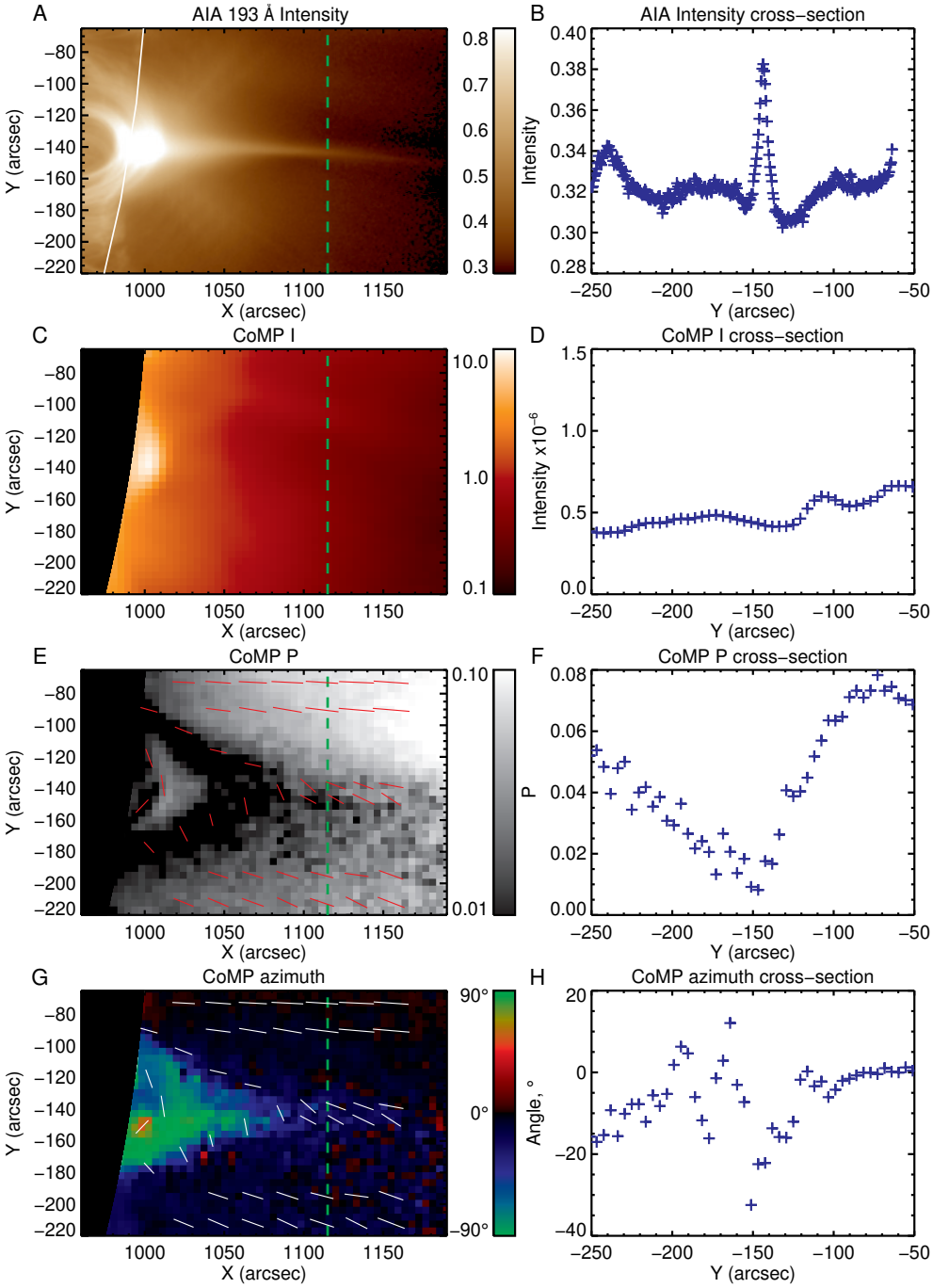

Figure 3.3: A) Normalised AIA 193 Å intensity. Curved white line marks position of the CoMP occulting disk. B) AIA 193Å cross-section of intensity along the dashed green line in adjacent panel. C) CoMP 1074.7 nm I D) CoMP 1074.7 nm cross-section of I, along the dashed green line in adjacent panel. E) CoMP 1074.7 nm P. Red lines are polarisation vectors, with length proportional to $-1/\log(P)$. F) CoMP 1074.7 nm cross-section of P, along the dashed green line in adjacent panel. G) CoMP 1074.7 nm azimuth angle θ, relative to the radial direction. White lines show the corresponding polarisation vectors. H) CoMP 1074.7 nm cross-section of θ, along the dashed green lines in adjacent panel. CoMP images have an overlaid artificial-occulter to increase sharpness at image edge.

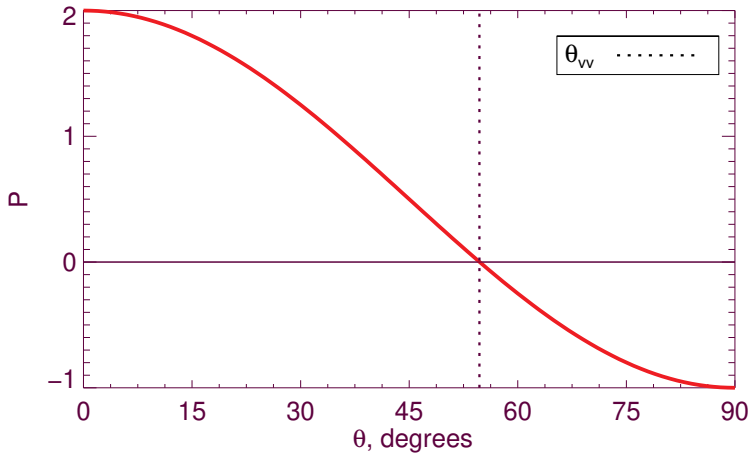

Figure 3.4: Plot of Equation 3.1 from 0 to 90°, marking the location of the 'Van Vleck' angle, $\theta_B = \theta_{VV} = 54.74°$.

amount of atomic polarisation, and is thus imprinted by the local thermal and magnetic conditions of the emission source plasma. Plasma temperature will affect the strength of the emission line, but does not change the fraction of linear polarisation. The observed polarisation therefore also varies as

$$P \propto 3\cos^2\theta_B - 1. \tag{3.1}$$

For a radial magnetic field, the magnetic field vector is parallel to incident radiation ($\theta_B = 0$) and linear polarisation is at a maximum. This maximum value is dependent on the line properties, radiation field and local density. For a tangential magnetic field, atomic polarisation becomes negative. The atomic polarisation passes through zero as $3\cos^2\theta_B = 1$, at the 'Van Vleck' angle $\theta_B = \theta_{VV} = 54.74°$. Because we have no prior knowledge of θ_B relative to θ_{VV}, the change in sign of atomic polarisation leads to a well-known 90° ambiguity in determining the POS projection of magnetic field direction. This can be visualised by the plot of Equation 3.1 in Figure 3.4. Beyond θ_{VV}, the equation yields a negative solution for P, which is not physical. Beyond this value, we instead detect a polarisation vector azimuth perpendicular to the true angle of the local magnetic field.

CoMP measures the two components of linear polarisation relative to a fixed reference direction (north), as well as total unpolarised intensity (Stokes U, Q and I

respectively). Combining these, we calculate fractional linear polarisation through,

$$P = \sqrt{U^2 + Q^2}/I. \tag{3.2}$$

We can also use Stokes U and Q to calculate the azimuth angle of the polarisation vector in the POS,

$$\theta = \frac{1}{2}\arctan\left(\frac{U}{Q}\right). \tag{3.3}$$

While θ is determined by U and Q measurements, the corresponding polarisation vector has the 90° ambiguity to magnetic field lines, either parallel, perpendicular, or undetermined depending on whether the actual (unknown) angle θ_B is greater than, smaller than or equal to θ_{VV}. The polarisation vector is not a physical 'vector' but a line with a magnitude and azimuth.

The corona is optically thin to infrared radiation. Therefore, every observation involves integration over the LOS. Variations in θ_B along the LOS lead to a superposition of different polarisation vectors (weighted by the local plasma density), causing a reduction of P.

3.5 Analysis

Figure 3.3A shows the time-averaged intensity of AIA 193 Å emission, sampling hot Fe XXIV emission, from 18:00 - 20:00 UT. During this period, the plasma sheet dimmed, but with no significant variation to its shape. The plasma sheet appears as a near-horizontal structure, stretching out from the top of the flare loop arcade (X $\approx 1020''$). A cross-section through the plasma sheet places the plasma sheet centroid at $Y \approx -145''$ (Figure 3.3B).

In comparison, Figures 3.3 C&E respectively show intensity I and linear polarisation P of cooler Fe XIII 1074.7 nm emission. All CoMP data shown are "level 2" data products from an improved pipeline from early October 2019. These data are now available on the MLSO website.

The images were calculated using the mean of 46 CoMP I, Q and U measurements from 19:44:36 to 20:03:06 UT (later images were excluded due to poorer see-

ing from passing cloud). Fe XIII 1074.7 nm emission comes from plasma around ∼1.5 MK, in contrast to AIA 193 Å at ∼1.2 and 20 MK. With clear emission in the post-flare loop-top, the absence of strong Fe XIII intensity in the plasma sheet is striking. The AIA 211 Å and 193 Å channels do show the plasma sheet at the later times CoMP observed, but emission is weaker and more diffuse than at earlier phases.

Cheng et al. (2018) examined the structure in white-light with the K-Cor instrument, measuring the plasma sheet to be 2.5 times larger in polarised brightness (pB) than seen in AIA 193 Å. This difference may be related to the dependencies of EUV and pB intensities on plasma density n as n^2 and n^1 respectively. Fe XIII emission theoretically depends on n^α, where α is closer to 1 than 2 owing to radiative excitation and some collisional depopulation.

The fractional linear polarisation P reveals a prominent dark triangular structure with a yet smaller dark structure underneath, just above the limb. The latter feature aligns with the bright flare looptop in the AIA image. The triangular feature however, overlies the faint triangular region seen in EUV over the looptops. (We suspect this faint structure may be related to the current sheet seperatrix, although we do not investigate that here). These two regions both have $P < 0.01$. Above the dark triangular structure, aligned roughly along the AIA plasma sheet emission, there is a broad, dark region, positioned radially from the top of the overlying structure to the west-most edge of the CoMP FOV. A cross-section through the region shows a significant drop in polarisation (Figure 3.3F), despite no clear I signature at the same location (Figure 3.3D). Here, we see a broad gradual drop in polarisation down to $P < 0.01$, from values of $P \approx 0.055$ and 0.075 either side of the feature. Despite being ~ 10 times broader than the structure observed in AIA 193 Å, minimum P occurs at approximately the same location as peak AIA 193 Å emission.

Polarisation azimuth angles θ are shown in Figure 3.3G. The colour map shows angle θ relative to the local radial, and white lines plot the vectors associated with this angle. Plotted vector length is proportional to $-1/\log(P)$. Polarisation vectors are also shown in Figure 3.3E. The polarisation vectors are close to radial above

and below the plasma sheet, and apparently trace the outline of the flare loops and overlaying magnetic field. Beneath this region, azimuth angles are near tangential to the solar surface. Such behaviour is unusual, as azimuth angles normally flip by 90° after crossing $\theta_{VV} \approx 54.7°$. It can occur under conditions where there is a particular symmetry along the LOS.

Taking a cross-section of polarisation azimuths across the sheet, we see the angles moving from $-20°$ to 0°, interrupted by a large dip to $-30°$. The peak of the azimuth drop is at the same location as maximum AIA 193 Å emission and minimum Fe XIII polarisation. This is a measurement artefact, as noise in U and Q increase as P decreases. Conclusions in this chapter are therefore based on the magnitude of normalised linear polarisation measurements alone.

3.6 Interpretation

Linear polarisation is created throughout the solar corona. There are only two mechanisms by which linear polarisation can be reduced. Firstly, collisions by thermal particles can locally destroy atomic polarisation. Secondly, integrations along the LOS and across the POS can both reduce the net polarisation observed, dependent on θ_B. At least one of these processes must be responsible for the significant and broad drop in polarisation observed across the plasma sheet.

3.6.1 Depolarisation via Collisions

To determine if collisions are responsible for removing polarisation in the plasma sheet, we must estimate the density of the region. The CoMP Fe XIII 1074.7 nm and 1079.8 nm lines are a density sensitive pair. We used the Coronal Line Emission (CLE) program (Judge & Casini, 2001) to determine the relationship between the line intensity ratio and electron density (at 1.5 MK). The 1079.8 nm emission is weak, extending only to the base of the plasma sheet at $\sim 1050''$. At this height, we calculate an electron density at 1.5 MK of 2.8×10^8 cm^{-3}, based on an intensity ratio of 0.27 (Figure 3.5).

At higher altitudes, this density is likely even lower. We can demonstrate this by measuring the change in total electron density with height, as it is proportional

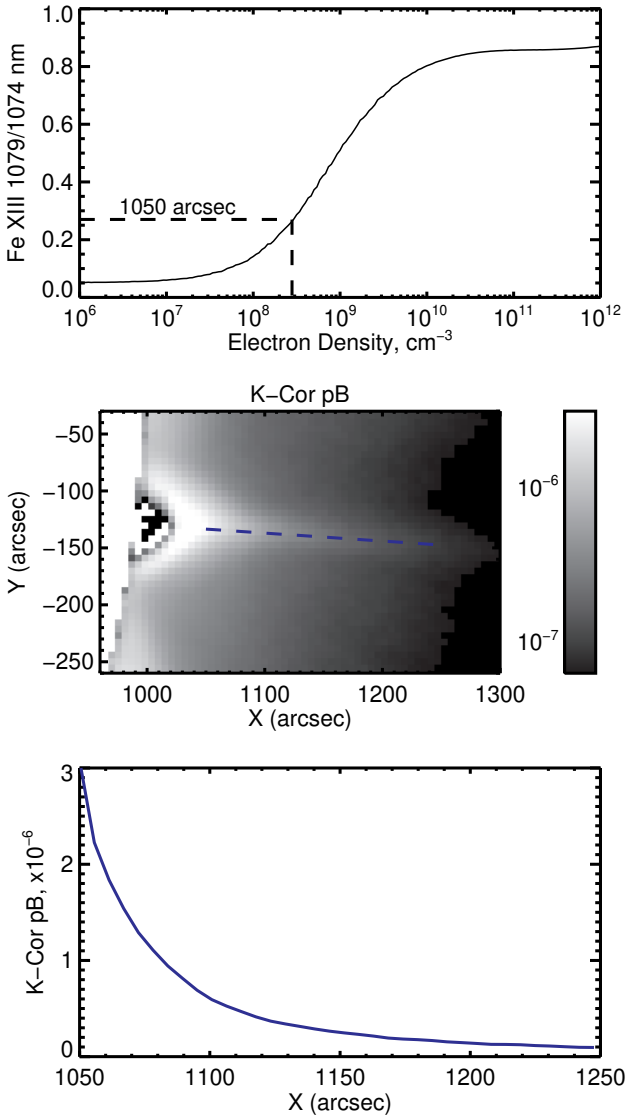

Figure 3.5: Top) Theoretical density curve for Fe XIII 1074.7 to 1079.8 nm intensity ratio. The dashed lines mark the measured ratio at 1050″ above the limb, with corresponding density at this location. Middle) Time averaged K-Cor polarised brightness (*pB*) observations from 18:00 - 19:30 UT, with units B/Bsun. Blue dashed line marks the location of the cross-section in the panel below. Bottom) Variation in *pB* along the plasma sheet.

to the polarised brightness pB measured by K-Cor (Figure 3.5). n_e varies as

$$n_e \approx \frac{pB}{6.65 \times 10^{-25} 0.11 \ell}, \tag{3.4}$$

where ℓ is the integration length along the LOS (Orrall et al., 1990).

At an altitude of $1115''$, $pB = 0.5 \times 10^{-6}$. Therefore, if ℓ is greater than the observed plasma sheet width $w \approx 5$ Mm, $n_e < 1.4 \times 10^{10}$ cm^{-3}. Assuming $\ell \approx 30$ Mm (Cheng et al., 2018), $n_e \approx 2 \times 10^9$ cm^{-3}. These densities are not high enough to destroy atomic polarisation via collisions. We therefore conclude that this is unlikely the cause of low linear polarisation in the plasma sheet. However, the dark polarisation signal aligned with the top of the flare loops (peaking over the occulter), is likely a result of depolarisation via collisions in the denser flare loops.

3.6.2 Depolarisation via Magnetic Field Structure

Levels of linear polarisation are dependent on magnetic field structure and orientation. The approach of P to zero for angles near $\theta_{VV} \approx 54.7^\circ$ suggests that the small values of P can be accounted for either by a large-scale field close to this angle, or by a more structured field in the POS and/or LOS that contains a mix of angles θ_B. The cartoon in Figure 3.6 visualises how this variation of POS field can affect polarisation via equation 3.1. In case A) we have a magnetic field close to radial, similar to what you would expect from a laminar Sweet-Parker current sheet. In this instance, $\theta_B \sim 0$, and thus P is at a maximum (which is dependent on density and line properties). In case B), if a large scale magnetic field traces close to 55.7°, we are at θ_{VV} and $P = 0$. If, in the third case C), we have structured θ_B within a given pixel, the value of P will lay somewhere between 0 and the maximum value – depending on what the magnetic structure within the pixel contains.

The morphology of the dark triangular structure in P (Figure 3.3E) strongly suggests that the Van Vleck effect is operating at the edge of the arcade field, as magnetic field lines wrap around the large-scale current systems producing them (case B in cartoon of Figure 3.6). Such magnetic null lines are commonly seen in calculations and data (e.g. Judge et al., 2006; Gibson et al., 2017). However,

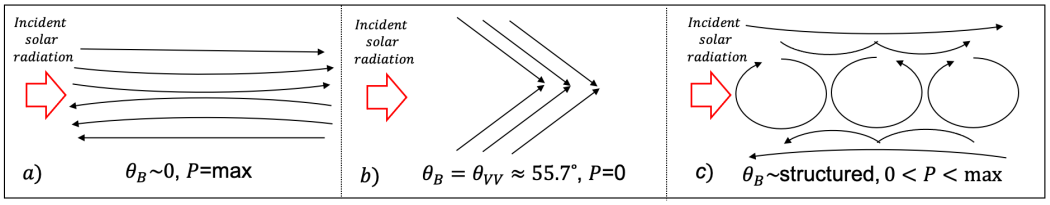

Figure 3.6: Simple cartoon demonstrating the polarisation level expected for different magnetic configurations, with black arrows representing the magnetic field orientation/direction, and red arrows the radial direction from the Sun. The configurations are: a) Laminar, anti-parallel field, similar to that expected from a Sweet-Parker current sheet. b) Field lines pulled tight to an angle of 55.7°. c) Magnetic island structures within an anti-parallel field structure.

the geometry of a Sweet-Parker plasma sheet, with a magnetic field direction close to radial, is incompatible with continuous Van Vleck nulls produced in this fashion. We can simulate the emission from such configurations using simple empirical models in CLE. CLE can be used to synthesise the Stokes profiles of coronal forbidden lines such as Fe XIII. In Figure 3.7A we model an infinitely long laminar current sheet, similar to that expected from Sweet-Parker reconnection. Here, we see almost no drop in polarisation (Figure 3.7B). Therefore, the levels of P measured by CoMP are inconsistent with a laminar Sweet-Parker current sheet in the standard eruptive flare model.

Small-scale magnetic structures, such as plasmoids or a turbulent magnetic field (formed perhaps as a result of current sheet instabilities), naturally lead to variations in θ_B. These structures would therefore cause an overall reduction in P, especially if unresolved. To explore such an effect we create simple numerical models of these structures using CLE, to compare again with observations. These simple calculations (Figure 3.7) show polarisation levels P and corresponding polarisation vectors. Each case utilises a similar geometry to CoMP observations, with the plasma sheet centred around the line $y = -0.073''x - 67.53''$. Sample polarisation cross-section profiles are also shown. The models assume that the plasma contributing mostly to the emission is confined to a narrow region within $10^{-2}R_{\odot}$ of the POS, to avoid LOS cancellations, and thus to highlight effects of POS magnetic structure.

The 'plasmoid' models (Figures 3.7 C&E) consist of infinite LOS line cur-

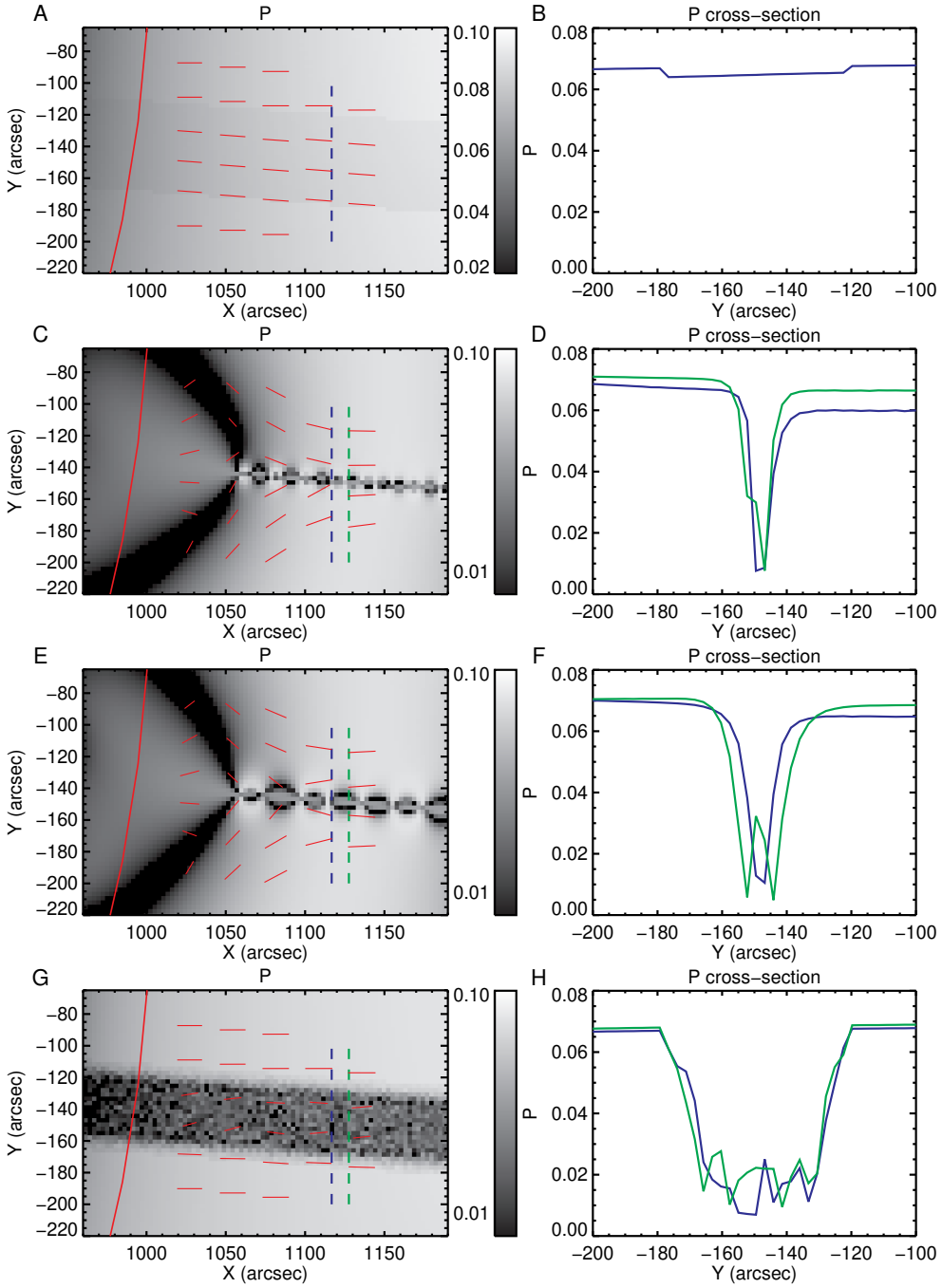

Figure 3.7: Maps of linear polarisation P for plasma sheet models, with associated cross-sections. CoMP occulting disk position is marked by the red curved line, and polarisation vectors as red dashes. Cross-section locations are marked by the blue and green dashed lines, corresponding to the plot colour of the cross-section. Models show: AB) Laminar plasma sheet, with magnetic field parallel to the sheet direction. CD) Potential field model generated from infinite LOS line currents placed at *unresolvable* intervals along the plasma sheet, combined with a sub-surface dipole. This represents plasmoid reconnection within the current sheet. EF) The same potential field model as above, but with currents placed at resolvable distances. GH) Nonphysical plasma sheet with a randomly orientated field, analogous to plasma turbulence.

rents (placed at intervals along the plasma sheet), combined with the potential field generated from a sub-surface dipole. This 2D configuration is the simplest representation of what might constitute a series of magnetic islands formed by the plasmoid instability in the POS.

Figures 3.7 C&E show calculations of plasmoids with sizes below and above the resolvable limit respectively. In both cases, the interaction between the plasma sheet edge and surface dipole form a black 'V-shaped' structure, where field lines trace an angle close to the Van Vleck angle. The V-shapes occur here as magnetic field lines wrap around the line currents placed along the LOS within the plasma sheet. This is unlikely the cause of the similar structure in CoMP observations however, as the model relies on the infinite line currents to form this feature. The primary region of interest is the plasma sheet above this region.

In the unresolvable plasmoid model (Figure 3.3C), polarisation drops to a minimum of $P \approx 0.01$ (Figure 3.3D). The resolved plasmoid case (Figure 3.3E) has much more variation in P along the plasma sheet however, varying greatly between the plasmoid edge and centre. In this resolvable case, minimum polarisation is calculated as $P \approx 0.005$.

In addition to the plasmoid models, we calculated an un-physical model of a randomly orientated field configuration running along the plasma sheet, again with plasma within $10^{-2} R_{\odot}$ of the POS (Figure 3.7G). Across this structure, we calculate a drop in polarisation of to $P \approx 0.015$. In this case, using a random field structure imitates the signal of physical fields which, when integrated over finite volumes, contain the same distribution of vector magnetic fields.

Although these models are relatively simple, they provide an analogue for the polarisation levels CoMP might observe for representative magnetic topologies. In both the plasmoid and random field cases, magnetic field orientation is shown to be capable of reducing polarisation to that observed in this event. With future observations (given an adequate signal-to-noise and integration time), spectropolarimetric measurements can provide observational constraints for the theoretical nature and scale of magnetic substructure in the corona.

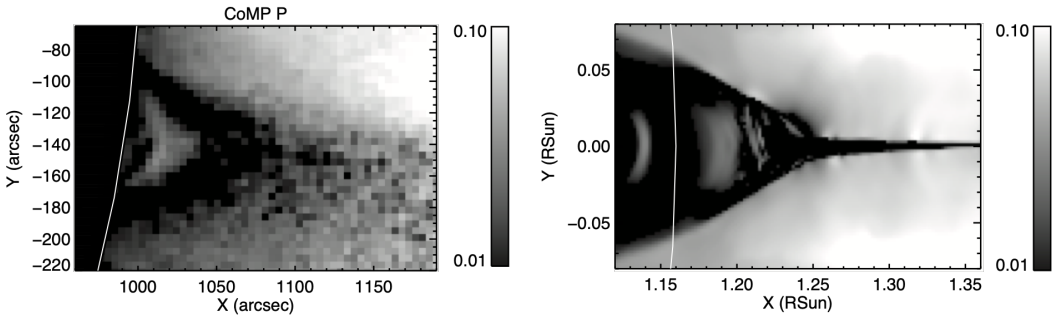

Figure 3.8: Comparison of 10th September 2017 CoMP *P* data (left), with synthesised *P* emission from the 2.5D ARMS model (right) of an eruptive flare.

3.6.3 Preliminary MHD Model Comparison

Although the simple empirical models are successful in providing insight into the plasma sheet dynamics, greater insight could come from a comparison to more advanced MHD models. Figure 3.8 shows a preliminary comparison between the CoMP *P* observations and forward modelled *P* from the 2.5D ARMS model (Karpen et al., 2012) using the IDL FORWARD tool set (Gibson et al., 2016). This 2.5D model is of a generic off-limb flare (not the 10th September event in particular), and thus has not been modified to match the event's length scale, for example.

The 2.5D ARMS model features a variable-mesh method, which models different aspects of the flare with different spatial resolutions, selected based on the physical scales of interest in each region. The current sheet is modelled with the highest resolution, and features the turbulence and plasmoid structures we suspect are present in the 10th September 2017 flare – making the model a suitable comparison to the CoMP data.

From this qualitative comparison, we immediately see the three primary polarisation features captured by the MHD model. We see low polarisation in the flare loops due to high densities (depolarisation via collisions), as well as the low polarisation 'van-vleck triangle' aligned with magnetic field lines tracing the current sheet seperartix. Above these regions, we see a low-polarisation feature aligned with the current sheet, in which plasmoid reconnection is taking place. A deeper comparison between observations and MHD models is an area of future work (Chapter 6.2), but we feature the preliminary comparison here to support the arguments of

depolarisation sources listed in this chapter.

3.7 Discussion

In summary, polarisation data from CoMP seem to demonstrate three properties:

1. A broad and gradual reduction of linear polarisation across the plasma sheet, with lowest amplitudes at the sheet centre. This polarisation structure may be long-lived – longer than the EUV-visibility duration of the same structure.

2. No clear increase in IR intensity, in contrast with EUV emission.

3. Coherent and large 'V-shaped' structures of low polarisation below the plasma sheet, reminiscent of the Van Vleck nulls clear in earlier calculations (Judge & Casini, 2001).

4. Near-tangential polarisation vectors beneath the plasma sheet, roughly aligned with the aforementioned dark 'V-shaped' structures.

The near-tangential polarisation seen under the plasma sheet is certainly unusual, as near-radial polarisation is found far more frequently (e.g. Arnaud & Newkirk, 1987). This is potentially a LOS integration effect through the plasma, cancelling out only radial components of polarisation. This could perhaps provide information on the large-scale field structure under the plasma sheet, but is an area of future study and does not affect the conclusions drawn in this paper.

Although the simple plasmoid models can produce the minimum polarisation levels observed by CoMP in the 10th September 2017 flare, they do not replicate the gradual and wide drop in the polarisation structure, significantly broader than EUV observations of the plasma sheet. Recent sophisticated calculations suggest a natural explanation, consistent with the observed behaviour of P across the sheet (Stanier et al., 2019). Cascades of plasmoids caused by fragmentation of finer and finer current sheets diffuse from modelled plasma sheets much faster than the plasma itself. We might expect this to produce a similar polarisation signature to that observed by CoMP in the later phases of this event. It may also explain in part

why the sheet was essentially invisible in the measured Fe XIII intensity, but visible in P. We speculate that if CoMP had started observing at the start of the flare, we would have observed a polarisation structure of similar width to observed intensity, broadening as the process calculated by Stanier et al. (2019) evolves.

3.8 Conclusions

We find that the drop of linear polarisation measured by CoMP in the 10th September 2017 flare is consistent with the presence of plasmoids and turbulent fluctuations in the magnetic field, similar to those expected from the tearing-mode instability. While previous work has focused upon spatially resolvable features in images of the dynamic corona, we have shown that linear polarisation can serve as measure for random magnetic structure on sub-resolution scales. The method provides a diagnostic to analyse the fragmentation of current sheets through the tearing-mode or plasmoid instability, which creates a cascade of energy associated with magnetic-field fluctuations toward smaller scales, well below observable limits.

The work is consistent with theoretical work suggesting the links between current sheet dynamics, plasmoid fragmentation, and a turbulent cascade of energy associated with magnetic-field fluctuations. The analysis favours the interpretation of a continued presence of unresolvable magnetic structures (such as that formed by magnetic islands), rather than the 'random' magnetic structure created by plasma turbulence.

It is anticipated that the start of observations with DKIST will provide data of the necessary quality to further disentangle the intriguing physics discussed here. In particular, a spectrograph (in contrast to the CoMP filtergraph), could further explore the mystery of why P is clearly related to the plasma sheet but I is not.

3.8.1 11th September 2017 Observations

24 hours after the CoMP observations presented in the chapter, the MLSO telescopes CoMP and K-Cor started daily observations once again. The 10th September 2017 flare was incredibly long-lived, and there is still signal of the flare from these instruments – some 27 hours after flare onset (long beyond any signal of the plasma

sheet in EUV). These observations, and a wider study of the flare's long duration, are included within the next science chapter, Chapter 4.

Chapter 4

Dynamics of Late-Stage Reconnection in the 10th September 2017 Solar Flare

This chapter primarily includes work from French et al. (2020), as well as some unpublished work from an ongoing study. The DEM inversions were calculated by David Long.

4.1 Introduction

In the standard 'CSHKP' solar flare model (Carmichael, 1964; Sturrock, 1968; Hirayama, 1974; Kopp & Pneuman, 1976), reconnection is believed to power the impulsive phases of flares, typically lasting a few minutes to an hour. There has, however, been evidence to suggest that magnetic reconnection within flares can persist for much longer than this, with energy release timescales of tens of hours (Bruzek, 1964), albeit at a more gradual rate than during the impulsive phase. It is believed that these long-duration events can only persist if the magnetic topology of the event allows for this continuation of slower, higher altitude reconnection above the flare loops (Kahler, 1977; Svestka, 1989). The 10th September 2017 flare appears to be particularly long-lived, as evident in Chapter 3 of this thesis with the CoMP polarisation signal (and the ongoing EUV plasma sheet) suggesting that reconnection in some form is still ongoing 4 hours after flare onset.

Observations of the impulsive phase of the 10th September 2017 flare have been thoroughly explored. As discussed in Chapter 3, multiple studies have revealed evidence for turbulence or tearing mode instabilities within the plasma sheet, such as unusually high emission line widths and associated non-thermal velocities, which Warren et al. (2018) interpreted as reconnection-induced turbulence and outflows. Quasi-periodic pulsations have been reported (Longcope et al., 2018; Cheng et al., 2018; Hayes et al., 2019), along with small-scale velocity fluctuations consistent with turbulent plasmoid fragmentation (Cheng et al., 2018). Most of these observations occurred within forty minutes of flare onset. One study by Yu et al. (2020), published in the same month as the work from this chapter (French et al., 2020), explore observations up to 20:00 UT (around the time of CoMP observations) – finding evidence of continuing reconnection outflows at this time.

The previous chapter of this thesis, based on work in French et al. (2019), provided further evidence to suggest the presence of reconnection-induced instabilities, based upon CoMP spectropolarimetric data from coronal forbidden Fe XIII lines. In spite of the strikingly laminar appearance of the plasma sheet in unpolarised measurements (e.g. from AIA), the amplitude of linearly polarised light was found to be anomalously small along the sheet. In a process of elimination, we concluded that the magnetic field could not be laminar, and instead must contain unresolved structure on sub-pixel scales.

These CoMP measurements took place 4 hours after the flare onset, long beyond the impulsive phase of the event. The plasma sheet is still clearly visible in extreme ultraviolet (EUV) images at this time, (similar to the duration of previously observed EUV plasma sheets, Savage et al., 2010; Seaton et al., 2017). The presence of sustained reconnection and instabilities within the plasma sheet at this point in the flare's evolution suggests that the fast reconnection process plays a role throughout the entire dynamic evolution of the flare, and not just during the impulsive phase.

In the multi-instrument study within this chapter, we provide additional evidence for sustained fast reconnection beyond the flare's impulsive phase, and investigate the late-stage evolution of the flare's dynamics and topology by examining

plasma kinematics associated with the standard flare model. Using Hinode/EIS, CoMP, SDO/AIA, K-Cor, Hinode/XRT, RHESSI, and IRIS, we examine Doppler velocities, hard X-ray (HXR) sources, and flare loop growth. We also use previously unpublished EIS data to track the evolution of non-thermal velocity and temperature at the base of the plasma sheet, supporting the interpretation from the 10th September 2017 CoMP data that the low polarisation signature is likely a result of internal magnetic structure expected from the presence of small-scale plasma instabilities. On even longer time scales, we use Differential Emission Measures and polarisation data to study the longevity of the flare's plasma sheet and cusp structure, discovering that the plasma sheet is still visible in CoMP linear polarisation observations on 11th September 2017, long after its last appearance in EUV. We deduce that magnetic reconnection of some form is still ongoing at this time – 27 hours after flare onset.

4.2 Observations

The 10th September 2017 event was observed across the electromagnetic spectrum by multiple instruments. Hinode/EIS (section 2.1.1) captured the flare from its onset at 15:44 UT, past its peak at 16:06 UT, up to 16:52 UT. Observations later continued at 18:39 UT, observing the late evolution of the flare until 19:31 UT. In both observing runs, EIS observed the flare with a $2''$ slit, which provides an approximately $4''$ resolution over a field of view (FOV) of $240 \times 300''$. The slit spectrometer rasters the FOV from west to east with a cadence of 8 minutes 52 seconds. The plasma sheet is most visible in the Fe XXIV 192.04 Å line, which at the peak of the contribution function samples plasma with a typical formation temperature of 20 MK in a thermal plasma. The FOV changed between the two EIS observation sequences. The first sequence observed the full radial extent of the plasma sheet, whereas the second was pointed $120''$ to the east, missing the upper plasma sheet but sampling some of the underlying solar disk. Both FOVs are shown in Figure 4.1.

Spectral maps from EIS are supported by full disk EUV images from SDO/AIA (section 2.2.1). AIA observed the event with a 12 second cadence and $0.6''$ spatial

resolution, with a varying exposure time. The plasma sheet is most visible in the broadband 193 Å filter, which measures plasma from the cooler Fe XII and hotter Fe XXIV lines. It is emission from this hotter line dominating during the early flare, which explains the similarities between AIA 193 Å and EIS 192.04 Å observations (Figure 4.2).

Hinode/XRT (section 2.1.2) captured the duration of the flare in thin Al Poly and thin Be filters. This is a broad band imaging instrument, with temperature sensitivity peaking at 6.9 and 7 MK respectively for each filter (Narukage et al., 2011). Observations continued for the days succeeding the flare and imaged the post-flare loops as they rotated off the limb.

Observations from IRIS (section 2.3) are also available for this event. IRIS observed from 12:00 UT to 19:22 UT with a *large* ($119 \times 119''$) slit jaw FOV orientated at 60 deg, capturing the edge of the erupting flare in the top left of the frame. At 19:44, IRIS slit jaw observations switched to a *very large* ($166 \times 175''$) FOV, continuing until 04:13 UT. In this wider FOV, we observe the larger flare loop structure and primary plasma sheet base. In both the *large* and *very large* FOV rasters, IRIS acquired data with the 1330 Å slit-jaw window. The FOV of both rasters are shown in Figure 4.1.

These observations were complemented by HXR measurements from RHESSI (section 2.5). RHESSI had four operational detectors at the time of the flare, and took measurements intermittently across the flare's duration.

Finally, we include observations from the MLSO CoMP (section 2.4.1) and K-Cor (section 2.4.2) coronagraph instruments. The 10th September 2017 data from these instruments have been presented in the previous chapter. Mauna Loa observations continued the next local morning on 11th September 2017, from 17:41 and 17:37 UT for CoMP and K-Cor respectively. As with measurements on the day before, CoMP measured linear spectropolarimetry (Stokes I,Q,U) of infrared coronal forbidden lines in the low corona ($\sim$1.03 to 1.5 $R_\odot$), with the occulting disk location shown in Figure 4.1. Here we focus primarily on Fe XIII 1074.7 nm emission, measured with a $4.35''$ spatial resolution and a varying cadence. The

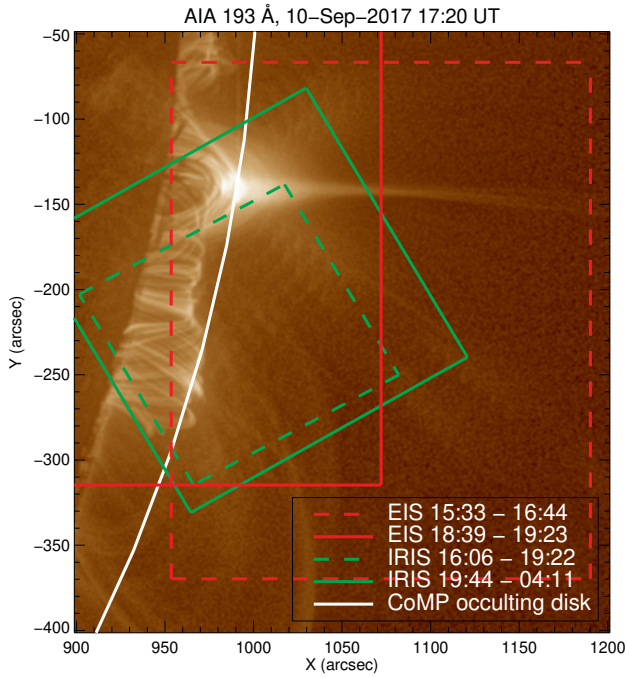

Figure 4.1: IRIS (green) and EIS (red) FOVs overlaid on an AIA 193 Å image. Dashed lines represent earlier observing sequences, and solid lines later. The location of the CoMP occulting disk is shown in white.

Fe XIII 1079.4 nm is also available however, forming the density sensitive pair with Fe XIII 1074.7 nm. K-Cor complements this with measurements of white light polarisation (pB) from $\sim$1.03 to 1.5 $R_{\odot}$, with a 5.64″ spatial sampling and 15s cadence.

4.3 EIS Spectroscopy

Hinode EIS observations of the impulsive flare phase are studied in Warren et al. (2018) and Cheng et al. (2018), which look at the early EIS data up to 16:44 UT. Analysis of the later EIS observations, from 18:39 - 19:23 UT, had not been published before the work in this chapter. Although the alignment of the earlier EIS observations are optimal for studying the visible plasma sheet, saturation of the detectors by bright features under the plasma sheet makes spectral analysis of this region, including post-flare loops, impossible. In the later observations however, the flare loops have cooled enough for EIS to measure reliable spectral data during the late flare evolution. Unfortunately, pointing for the latter observations only captures

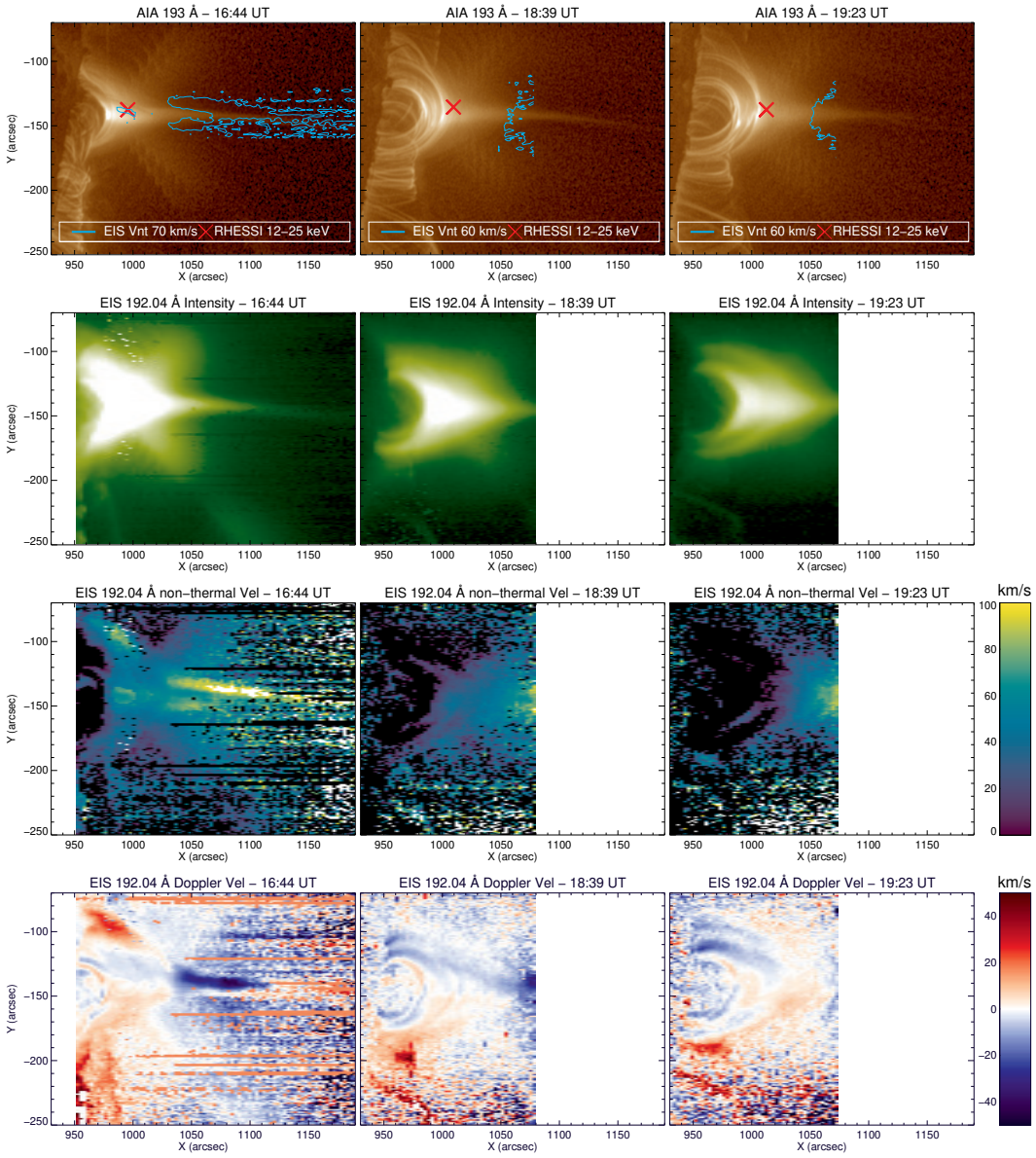

Figure 4.2: From left to right, the three columns show data at 2017 September 10 16:44, 18:39 and 19:23 UT. Top: MGN sharpened (Morgan & Druckmüller, 2014) AIA 193 Å observations. Blue contours show regions of highest EIS non-thermal velocities from row 3. The red X marks the location of highest 12–25 keV RHESSI emission. Second row: EIS 192.04 Å intensity measurements. Third row: EIS 192.04 Å non-thermal velocity measurements (km/s). Bottom row: EIS 192.04 Å Doppler velocity measurements (km/s). A diffraction pattern is visible in earlier frames, seen as a cross emanating from the brightest region.

the base of the plasma sheet on the western edge of the frame.

In Figure 4.2, we examine the evolution of the flare region across three EIS Fe XXIV 192.04 Å rasters, with accompanying broadband AIA 193 Å observations. We present the last EIS raster of the earlier observing sequence (16:44 UT) and the first and last raster of the later observing sequence (18:39 and 19:23 UT). It is worth noting therefore that the three frames are not evenly spaced temporally. The EIS data were prepped using the SolarSoftWare *eis_prep.pro* routine, with saturated data points removed using *eis_sat_windata* (this only has an effect in rasters at the start of the flare), and lines fitted using *eis_auto_fit*. Wavelength correction due to spacecraft orbital variation is also applied. AIA observations around corresponding EIS times were chosen with an exposure time under 1.5 seconds, to minimise effects of saturation in the flare loops. The AIA 193 Å images are sharpened using the the Multi-Scale Gaussian Normalisation (MGN) technique (Morgan & Druckmüller, 2014).

The EIS Fe XXIV 192.04 Å line has a formation temperature of 17 MK, whereas the broadband AIA 193 Å channel samples both the higher temperature Fe XXIV and cooler temperature Fe XII lines (with formation temperature at 1.2 MK). At 16:44 UT, there is a clear similarity between the EIS and AIA measurements, with both instruments measuring hot plasma in the bright primary flare loops, the prominent horizontal plasma sheet structure, and dimmer flare loops to the south of the frame. The primary flare loops are still significantly saturated in the EIS observations, causing the visible 'X'-shape diffraction pattern. This diffraction pattern is still noticeable at 18:39 UT, but gone by 19:23 UT. A slight diffraction pattern of similar shape is also visible in AIA.

Later in the flare, differences between EIS and AIA observations of the region become more apparent. In AIA, the plasma sheet is still clearly present at 18:39 UT, with the dimmer cusp-like separatrix structure visible around it. In EIS measurements however, these two structures appear to blend into one, forming the dominant cusp feature. As time passes, the flare loops rise and the cusp structure starts to evolve towards a smoother, perhaps less stressed structure. The southern

flare loops are almost invisible in these later EIS times too, despite still seen in AIA. These loops have cooled enough to be visible in Fe XII lines rather than in Fe XXIV, in contrast to the primary flaring area loops, which still contain significant 17 MK Fe XXIV emitting plasma. Electron temperatures in this region are explored in section 4.3.3.

4.3.1 Doppler velocity

Doppler velocities of the plasma sheet's early evolution were studied in Warren et al. (2018). Unusual red and blue shifts were reported, but these were attributed to an artifact of the instrument's asymmetric point spread function (PSF). These instrumental artifacts are most common where a sudden sharp change in velocity/intensity is observed. A similar pattern in the plasma sheet is seen in the EIS 16:44 UT Doppler data shown in Figure 4.2. Doppler measurements in the flare loops are not available throughout the early EIS observing sequence, due to high levels of saturation in this region.

In the later EIS observations however (from 18:39 UT onwards), the flare loops are no longer saturated. Additionally, the brighter cusp region means there is no longer sudden intensity/velocity variation across the plasma sheet, meaning the PSF effect is less of a concern. Due to this, we are able to present reliable Doppler velocity measurements of the 10th September 2017 event for the first time.

The nominal wavelength scale was determined from average spectral line centroid from a region on the disk. We see in Figure 4.2 (at 18:39 UT onwards) that the smallest loops closest to the limb are blue shifted on the southern half of the loop, and red shifted on the northern half, while the higher flare loops and cusp region display opposite behaviour. The blue shifted regions show areas of plasma with a component flowing towards the observer, consistent with plasma flowing down from the top of the newly reconnected flare loops (see cartoon in Figure 1 of Polito et al., 2018b). This Doppler pattern implies that the blue shifted footpoint is closer to the observer than the red shifted footpoint, giving us an indication of the orientation of the flare loops. The flare loops therefore sit close to the plane of sky (POS), but tilted slightly in either the north or south direction. The low LOS velocities of

10-20 km/s support the fact that the loops lay close to the POS, when compared to downflow velocities of several hundred km/s observed in previous flares (Antonucci et al., 1984).

Fleishman et al. (2020) provide a graphic displaying the orientation of the primary flare loops at reconnection onset. They show the southern footpoint of loops positioned on disk, closer to the observer, determined by the absence of an on-disk hard X-ray signature at the northern footpoint. This configuration is consistent with the observed EIS Doppler velocities in the lower flare loops. However, as further flare loops form (either at different altitudes and/or locations along the LOS), they do so with a different orientation from our LOS, resulting in a northern footpoint closer to the observer. Such an effect could be due to either a slight curve in the east-west polarity inversion line, or to higher altitude loops forming with lower shear.

At the edge of the FOV, at the tip of the cusp and base of the plasma sheet, we observe blue shifted plasma with velocities around 32 km/s in the LOS at 18:39 UT. These Doppler velocities align spatially with the regions of high non-thermal velocities. If the plasma sheet were tilted slightly away from the observer in the east-west direction, then blue shifted plasma at this location is likely a result of the downflow of plasma from the plasma sheet. This tilt is likely small, as LOS velocities are low compared to POS downflows of up to 165 km/s measured in a current sheet by Savage et al. (2010).

This is verified by recent work from Yu et al. (2020), who study POS downflows of the same 10th September 2017 flare we study here. Within 30 minutes of the 16:44 UT EIS observation, Yu et al. (2020) detect four clear periods of plasma downflows in the plasma sheet. These range in velocity between 100 – 170 km/s. By comparing the Doppler (LOS velocity) and downflows (POS velocity) for this event with a 2.5D MHD flare model from Chen et al. (2015); Shen et al. (2018), we can experiment with the orientation of the model to gauge an estimate of the plasma sheet tilt out of the POS. This is shown in Figure 4.3. The left panel shows the Doppler velocity signature expected from a 2.5D MHD flare model, tilted out

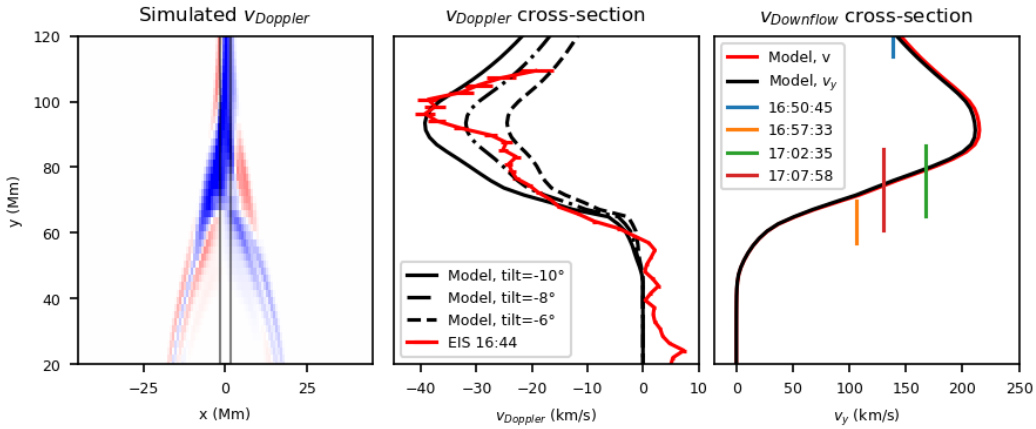

Figure 4.3: Left: Simulated Doppler velocity of Fe XXIV-temperature plasma for a 2.5D MHD flare model, tilted out of the POS. Middle: Black lines show cross-section of Doppler velocity along the plasma sheets, averaged between the solid lines in the left panel. Line styles show Doppler velocity produced by different model tilts. The red line shows the observed EIS Fe XXIV Doppler velocity along the plasma sheet at 16:44 UT during the 10th September 2017 flare. Right: The black solid line shows the MHD flare model POS downflow velocity (v_y), for a tilt of -10°, along the same cross-section shown in left panel. The red line shows the total downflow velocity v. The vertical coloured lines show the downflow velocity and height observed at different times during the 10th September 2017 flare by Yu et al. (2020).

of the POS. Plasma sheet downflows are therefore flowing towards the observer, producing the blue shift. The colour scaling is dependent on the angle of the tilt. A temperature mask has been applied to this Doppler signal, to include regions of the simulation at temperatures sensitive to the Fe XXIV line observed by EIS. Taking a cross-section along the simulated plasma sheet (between the vertical solid lines), we can plot the LOS (Doppler velocity) for angles at -10°, -8° and -6°. We compare these with the Doppler velocity observed in the equivalent region of the observed plasma sheet, during the 16:44 UT EIS observation (Figure 4.2). We can also compare the equivalent simulated POS downflows at these tilts with the height and velocity of the downflows observed by Yu et al. (2020). At these angles, the simulated POS velocity does not differ much from the total velocity. From the comparison, we see that the simulated and observed POS velocity profiles align well. There is more to be learnt from this comparison work between the EIS Doppler flows and MHD simulations (which is an area of ongoing research), but this initial

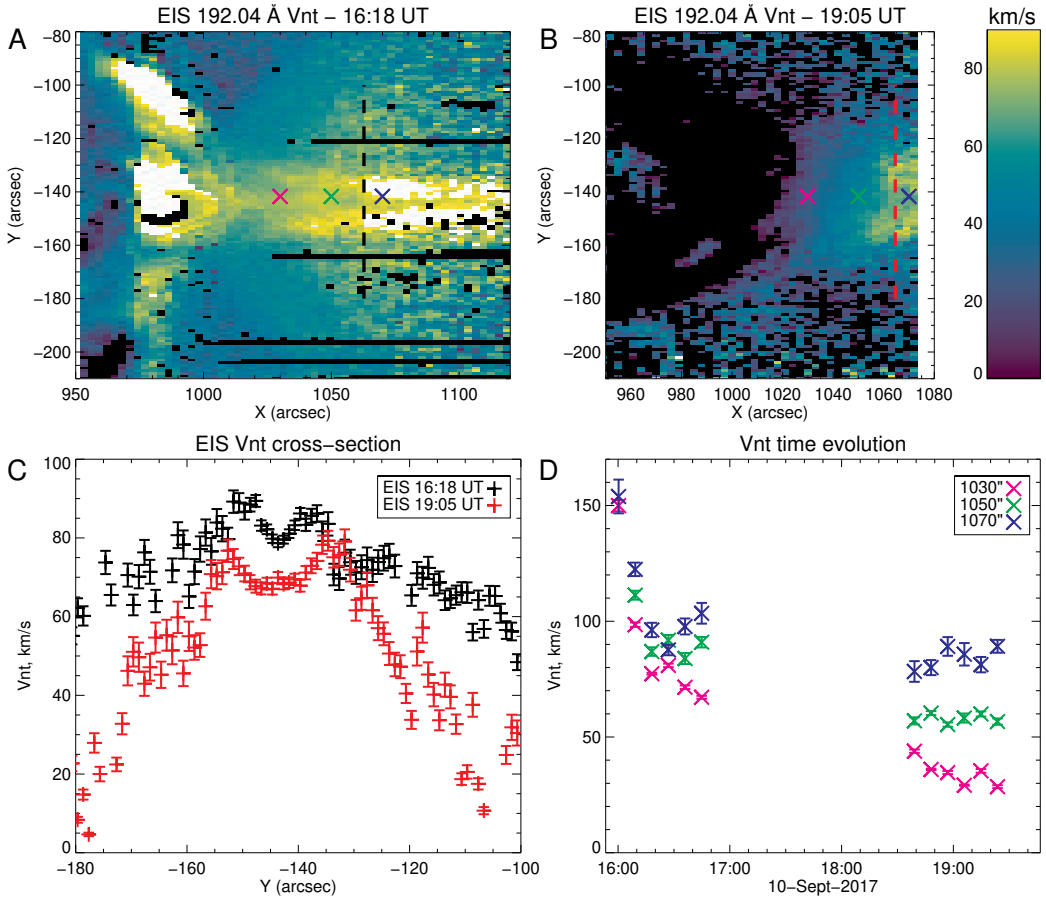

Figure 4.4: A,B: EIS 192.04 Å non-thermal velocity measurements (Vnt) (km/s) for 10th September 2017 16:18 and 19:06 UT respectively. The dashed lines correspond to the cross-sections in panel C, and coloured Xs refer to the locations at which we track velocity variations with time in panel D. C: Variation in non-thermal velocity across the plasma-sheet at 16:18 and 19:06 UT, along the slice marked in top panels. D: Variation of non-thermal velocity with time, at three locations along the plasma sheet (marked in top panels). Black pixels mark where either the Gaussian fit fits a line width smaller than the thermal width, or failed completely.

comparison satisfies our expectation of a plasma sheet structure sitting close to the POS, likely pointed away from us by a small angle of 6-10°.

4.3.2 Non-thermal broadening

Non-thermal broadening is the excess broadening observed in spectral lines after subtracting the instrumental and thermal line-widths. Non-thermal broadening can be caused by several processes, including opacity broadening, Stark broadening, and unresolved plasma flows with no preferential direction in the LOS (e.g. Doschek

et al., 2014). However, it is common in the coronal spectroscopy of flares in particular to associate excess line widths with the presence of non-thermal mass motions (e.g. unresolved flows, Antonucci et al., 1986) and derive an equivalent RMS speed from the excess broadening. The LOS RMS speed is referred to as the non-thermal velocity, given by $V_{nt} = \sqrt{2k(T_D - T_e)/m_i}$, where T_D is the Doppler temperature derived from the total observed line width, T_e the electron temperature given by the peak of the contribution function, and m_i the mass of the ion considered. Since T_e can be verified by line ratios in part of the FOV, and densities during flares are high, the excess line width cannot generally be accounted for by a difference in ion and electron temperatures.

Recent work by Kawate et al. (2016) does find evidence of departures from a Maxwellian distribution and ionisation equilibrium from EIS measurements of highly ionised Fe lines in flares. However, the number of pixels affected in the flares studied were of order 1.4%, leading them to conclude that the isothermal assumption is valid in most cases given the timescale of EIS exposures. We make this assumption in our own analysis, while acknowledging that departures could exist.

Figure 4.2 presents non-thermal velocity maps over the event, with contours of the highest velocities overplotted on the AIA 193 Å images. Both of these show the source of fastest non-thermal velocities rising with time, a continuation of what is seen in the first few EIS rasters of the flare (Warren et al., 2018). The temporal and spatial evolution of the velocities are shown further in Figure 4.4.

Figure 4.4 shows the non-thermal velocity measurements at 16:18 and 19:05 UT. Taking a cross-section of the velocity at a height of $1065''$ (Figure 4.4C), we see clearly the bifurcated velocity structure described by Warren et al. (2018) and Cheng et al. (2018). Although the structure is visible in most EIS rasters, it is most prominent in the two shown here. The origin of this bifurcation is uncertain, as it is not possible to distinguish between a LOS integration effect, or a true double peak structure persisting along the LOS. This velocity structure is long-lived, with these maps showing data 22 and 189 minutes after the flare onset. In the 166 minute

window between these observations, peak velocities only fall from 90 km/s to 80 km/s. As the plot shows however, velocities at the edge of the plasma sheet decrease at a much faster rate. This variation in velocity with time is explored further in Figure 4.4D, where we plot the change in velocity at three different altitudes of 1025, 1050 and 1075″, across the EIS observation times.

We see non-thermal velocity at these altitudes drop dramatically in the first 20 minutes of the flare, from upwards of 150 km/s down to 100 km/s. From here, velocity falls much slower, with its exact rate dependent upon the altitude. At the lower altitude of 1030″, velocities fall much faster to just 30 km/s at 19:23 UT. At 1050″, velocity remains constant at 60 km/s from 18:39 until the end of EIS observations at 19:23 UT. Velocities are highest around 1070″, still as high as 80 - 90 km/s at the end of EIS observations. They even appear to rise slightly towards the end of the observing sequence.

4.3.3 Electron Temperatures

As in Warren et al. (2018), we can estimate the electron temperature of the region using the temperature sensitive EIS Fe XXIV 255.10 Å / Fe XXIII 263.76 Å line pair. Emission in these lines does not extend to as high an altitude as Fe XXIV 192.04 Å emission, but is observed near the base of the plasma sheet in the early phase of the flare. Similarly to Fe XXIV 192.04 Å, the central flaring region is saturated, causing a visible diffraction 'X' for the duration of the first EIS observing sequence (Figure 4.5A). The diffraction pattern has disappeared by the later EIS rasters however, and we are able to discern the shape of the flare loops and cusp at the base of the sheet. Qualitatively assessing Figure 4.5B, we see a rise in temperature across the flare arcade with increasing height. This temperature increase is validated quantitatively in Figure 4.5C, plotting the temperature profile along the flaring region at 16:44 and 19:23 UT, the last raster of both observing sequences. We measure the temperature up to 1040″ with reasonable uncertainty, but this uncertainty increases further with altitude.

We observe that temperatures across the arcade fall between the two frames, albeit at different rates at different heights. Maximum electron temperature occurs

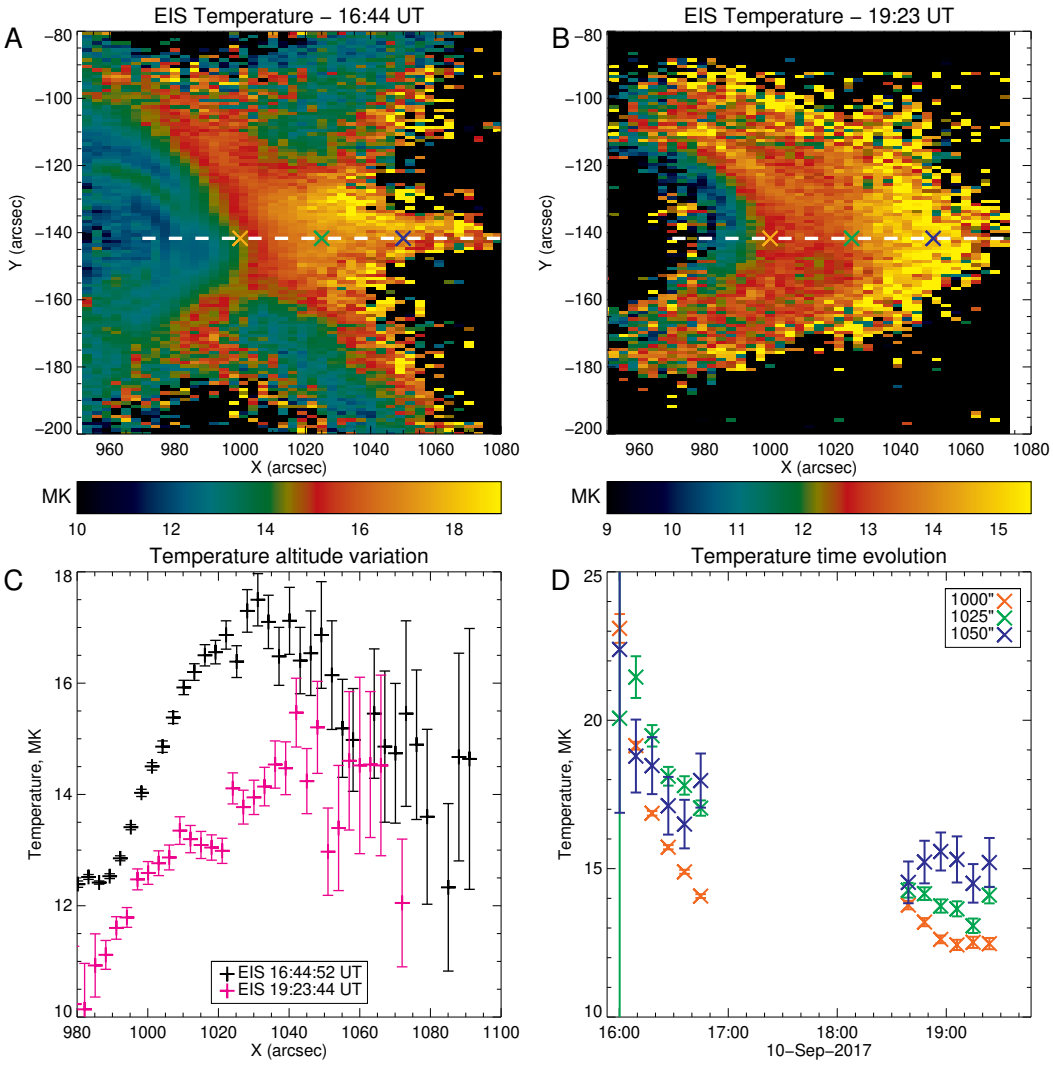

Figure 4.5: A,B: Temperature determined from the ratio of EIS Fe XXIV 255.10 Å to Fe XXIII 263.76 Å, at 10th September 2017 16:44 and 19:23 UT respectively. The dashed white line shows the cross-section slice shown in the panel C. coloured Xs mark the locations of temperature variation plotted in the panel D. C: Variation in temperature along the horizontal cross-section at 16:44 and 19:23 UT. Location of cross-section marked above. D: Variation of temperature with time, at the three locations marked in top panels.

at a projected height of $1030''$ at 16:44 UT, but around $1050 - 1060''$ at 19:23 UT, at the top of the cusp region. This observed change of temperature across the arcade profile is consistent with the heating of progressively higher loops along the LOS as the cusp grows throughout the flare's duration. The variation in temperature with time is shown further in Figure 4.5D, for the three different altitudes marked in the top frames of this figure. We see a rapid drop in temperature during the first thirty minutes of flare, only for the rate of cooling to rapidly decrease. This temperature evolution follows a similar trend to the velocity evolution seen in Figure 4.4 and in agreement with work from Warren et al. (2018), where the cooling rate of flare loops decreases with time as the densities within them decrease. As with the non-thermal velocity evolution, near constant temperatures can be seen at higher altitudes for the duration of the second EIS observing sequence.

4.4 Flare Loops

After forming due to magnetic reconnection, individual flare loops shrink rather than expand (e.g. Forbes & Acton, 1996). Therefore, the continued expansion of a flare loop arcade indicates the formation of newly reconnected loops at increasing heights as a result of ongoing reconnection. We can track this growth with IRIS and AIA observations.

At the beginning of the flare, IRIS was centered on the southern arcade and captured the edge of the primary loop tunnel as the CME erupted. A Supra-Arcade Fan (SAF) structure is observed over this southern arcade, the spectra of which are presented in Cai et al. (2019).

During the impulsive phase of the eruption, the primary flare loop tunnel (top left of Figure 4.6B) is seen to grow, as new flare loops form at progressively higher altitudes. The flare loops continue to grow well into the following day (visible in IRIS and AIA observations), despite the active region rotating further around the limb.

Figure 4.6 B and C show a cross-section through the primary flare loops, in both the earlier *large* (12:00 - 19:22 UT) and *very large* (19:44 UT onwards) IRIS

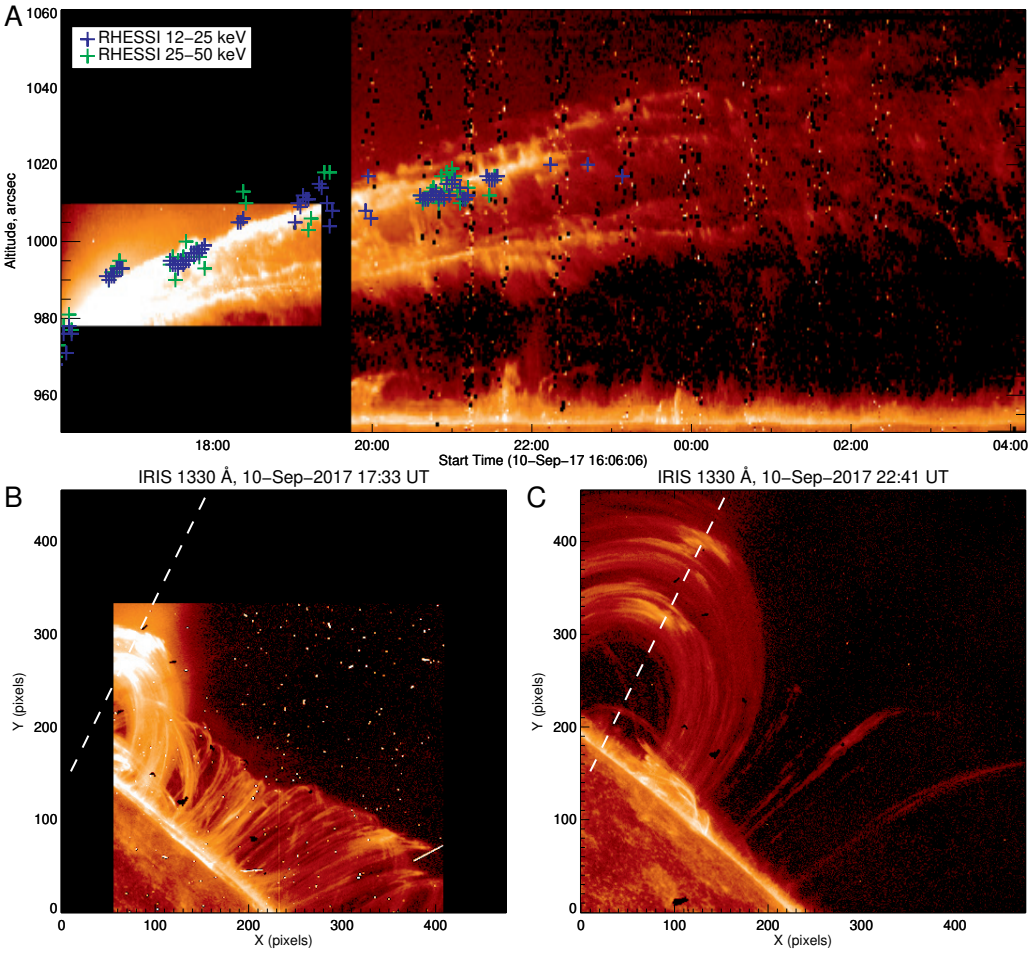

Figure 4.6: A: Height-time plot of a cross-section through the primary flare loop tunnel, as seen in IRIS 1330 Å images. The blue and green crosses mark the corresponding location of RHESSI 12–25 and 25–50 keV emission respectively. B,C: Example IRIS 1330 Å *large* and Example IRIS 1330 Å *very large* slit-jaw images with marked cross-section location (white dashed line). Context for the FOV is given in Figure 4.1. Color tables is in units of log(DN).

1330 Å slitjaw observing sequences, showing flare loops containing plasma already cooled to around 25000 K. The orientation of these frames are shown in Figure 4.1. By plotting intensity along this cross section, we produce the height–time plot shown in Figure 4.6A. From this diagram, we can see the growth of the brightest flare loops, with the formation of additional dimmer loops above. The bulk expansion of the flare loop system is fast at first, and slows to an estimated 1 km/s growth rate after $\approx$ 20:00 UT. In IRIS observations, the height of the flare loops peak around 90″ above the limb at 01:00 UT on the morning of 2017 September 11, around 9 hours after the flare onset and CME eruption.

The growth is even more remarkable considering the rotation of the active region onto the far side of the Sun, eclipsing the base of the flare loops. Using simple trigonometry with the solar rotation rate, we estimate that the rotation of the arcade over the western limb decreases the expansion speed by 10% during the time period analyzed. The bulk growth of a similar flare-loop arcade was analyzed by van Driel-Gesztelyi et al. (1997), who also found an arcade growth rate of 1 km/s in the late phase of an X-class flare.

4.4.1 RHESSI Looptop sources

According to the standard flare model, HXR emission can be produced at the flare looptops as high energy particles outflow from the reconnecting current sheet and collide with cooler plasma in the newly formed flare loops. The cartoon in Figure 2 of Chen et al. (2015) demonstrates this process, mirroring the observations in the top row of Figure 4.2 in this chapter. In Figure 4.2, the red cross shows the location of 12–25 KeV HXR emission as measured by RHESSI (Lin et al., 2002) at the time of each EIS raster, located at the top of the flare loops in each case. Above this, we see the contour of high non-thermal velocity, perhaps a signature of the reconnection outflows shown at the base of the current sheet in the cartoon of Chen et al. (2015).

The early evolution of RHESSI HXR sources with time is presented by Hayes et al. (2019). They examine the rise in 6–12 and 12–25 keV HXR signatures from the flare onset at 15:49 to 18:30 UT. In Figure 4.6, we overplot the location of 12–25 keV emission onto the IRIS height-time plot, from flare onset up to 23:00 UT. We introduce the 25–50 keV source location too, from onset to 21:30 UT. By binning the data over 120 seconds (30 spacecraft rotations), we are able to increase the signal to noise (S/N) ratio and resolve the emission source this late in the flare using the CLEAN algorithm. Binning in this way provides fewer data points, but shows a clear source of 12–25 and 25–50 keV emission 7 and 5.5 hours after the flare onset respectively.

In Figure 4.6, we see the HXR source height rising with time, at progressively slower speeds. At later times (around 20:00 UT) the X-ray point source continues

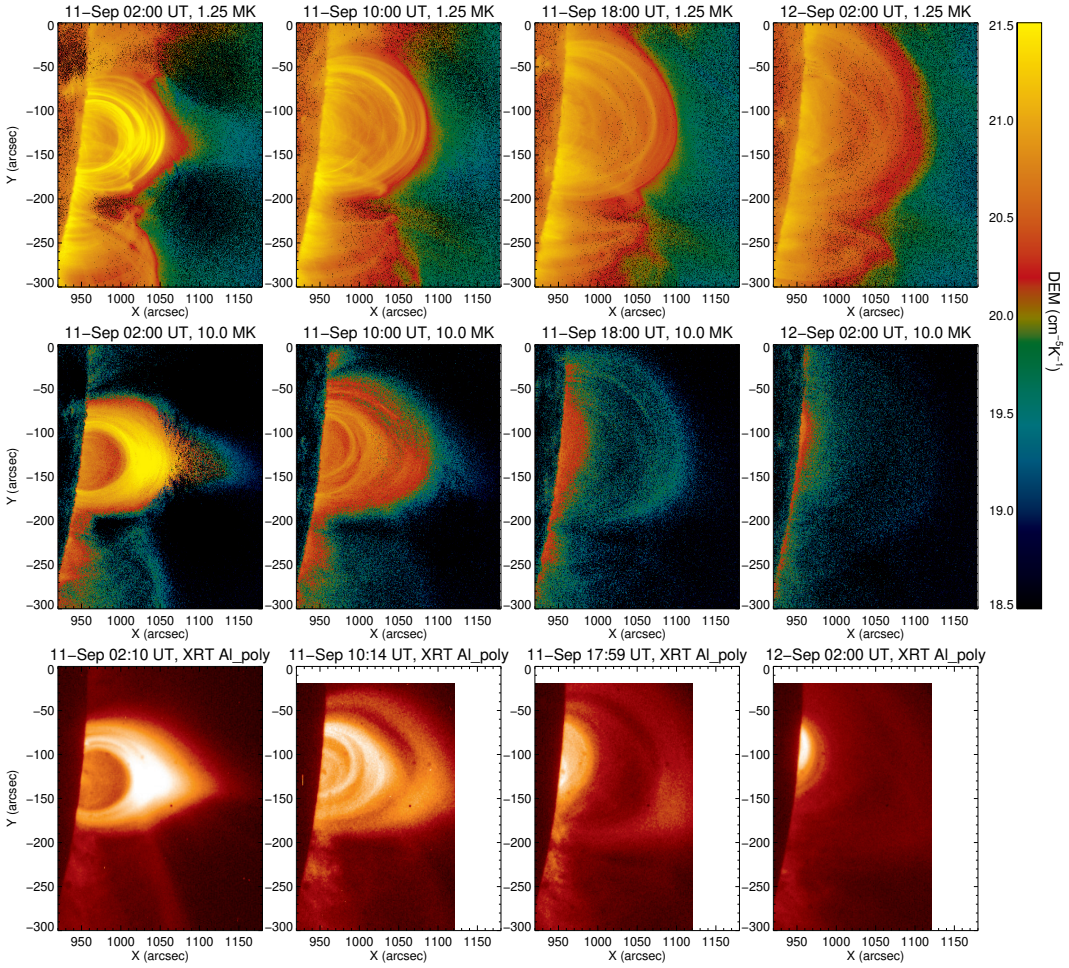

Figure 4.7: Top: Time evolution of AIA 1.25 MK DEMs. Middle: Time evolution of AIA 10 MK DEMs. Bottom: Time evolution of XRT Al poly.

to rise with the brightest flare loop, despite newer, fainter loops forming above it.

4.4.2 Continued loop growth

After the off-limb IRIS 1330 Å signal becomes too weak to track loop growth past September 11 01:00 UT, we see the loops continue to rise in AIA images. Differential Emission Measures (DEMs) can be used to track this growth at different temperatures, and Figure 4.7 shows the evolution of Emission Measure (EM) for 1.25 and 10.0 MK plasma, (constructed using the DEM code of Hannah & Kontar, 2013). The top row of Figure 4.7 shows the growth of the loops in cooler plasma, where both the primary (east-west) and southern (north-south) arcades continue to grow in height until around 12 Sep 02:00 UT – 34 hours after the flare onset. This continued growth is despite the fact that the active region is rotating further over the

western limb, meaning a structure of constant size would appear to shrink due to projection effects.

We see a similar effect with the hotter plasma too. On 11th September at 02:00 UT, 10 hours after the flare onset, the base of the plasma sheet is still visible at these high temperatures. The flare loops also have a more 'cusp-like' shape, in comparison to the relaxed lower-temperature loops (Gou et al., 2015). This cusp structure is also visible in XRT, where the Al poly observations are most sensitive to plasma at around 6.9 MK. This cusp feature seems to tilt to the south over the next 8 hours, where we see a small plasma sheet signal visible in the high temperature DEMs at 11 Sep 10:00 UT. The XRT FOV has shifted at this time, but the loop structure in these images still match those in the high temperature DEMs; visibly different to the loops seen at the same location in cooler plasma. To investigate this further, future study could investigate the flare loop cooling rate using DEMs, comparing with theoretical cooling rates. Although the EM of high temperature plasma grows weaker, there is still some plasma emitting at high temperatures on 12th Sep at 02:00 UT, as the loops reach their maximum observed height as they are eclipsed by the limb.

4.5 Polarisation Measurements

According to the standard model, the presence of a cusp would imply the existence of a reconnecting current sheet above it. As seen in Figure 4.7, there is no evidence of this in EUV images beyond around 11th September 10:00 UT. Since the EUV lines are collisionally excited, the EUV intensity falls off more rapidly with height than the infrared forbidden lines observed by CoMP which include a significant radiative contribution. Similarly, the Thomson scattered emission observed by K-Cor falls off less rapidly with height. To detect the remnants of the diffuse plasma sheet above the cusp, we turn to polarised infrared (CoMP) and white light (K-Cor) data.

Figure 4.8A shows white light polarised brightness (pB) measurements from K-Cor, time averaged over an hour from 11th September 2017 17:43 UT. K-Cor

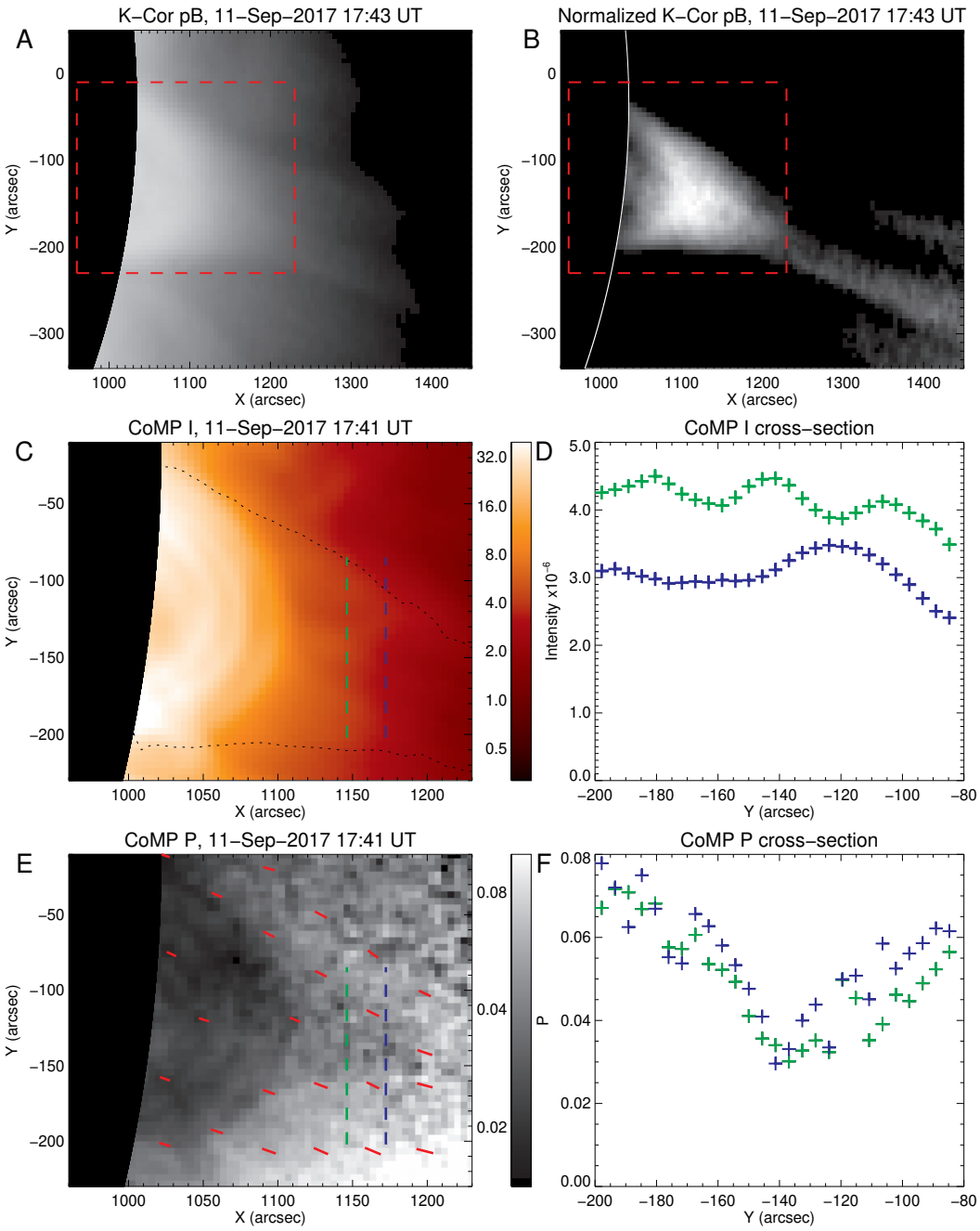

Figure 4.8: A: K-Cor polarised brightness, pB. Red dashed box shows FOV of CoMP panels. B: K-Cor pB, normalised by mean brightness at each altitude. C: CoMP 1074.7 intensity. The black dotted contour marks the location of K-Cor cusp feature in panel B. D: Cross-section of CoMP I, at locations marked in panel C with corresponding colours. E: CoMP normalised linear polarisation, $P = \sqrt{Q^2 + U^2}/I$. Red lines are polarisation vectors, with length proportional to $-1/\log(P)$. F: Cross-section of CoMP P, at locations marked in panel E with corresponding colours.

observes photospheric photons scattered by electrons in the corona and measures a variation of brightness with electron density n_e (rather than n_e^2 for EUV images) as, unlike EUV, it does not rely on collisional excitation (Landi et al., 2016). Due to this difference in density dependency, coronal brightness drops more slowly with height in white-light and infrared observations, allowing K-Cor to observe more diffuse coronal structures at much higher altitudes. Studying 4.8A, we can see the outline of the bright cusp-like feature on the limb, but it is difficult to resolve any detail. Figure 4.8B shows a processed version of this image, normalised by dividing each pixel brightness by the mean brightness at the corresponding altitude within the FOV. The plasma sheet is clearly visible and emanating from the cusp top towards the south-west. This direction was also indicated from the apparent orientation of the cusp consistent with XRT data shown in Figure 4.7. This southward deflection is interesting, given that the heliospheric current sheet is located in the northern hemisphere at this solar longitude. This deflection is then perhaps due to the over-expansion of open field above a coronal hole to the north of the flare loops (but to the south of the heliospheric current sheet). Projection effects may also contribute to this southward deflection as the flaring region rotates behind the limb. Although the plasma sheet is no longer visible in LASCO at this time, the instrument has observed a similar deflection of CMEs in the past (Kay et al., 2017).

4.5.1 Coronal Multi-channel Polarimeter

Using infrared polarisation measurements from CoMP, we can examine more closely the base of the plasma sheet structure observed by K-Cor. Linear polarisation provides unique and complementary information about source regions, enabling the study of thermal and magnetic conditions of both large-scale (Dove et al., 2011; Gibson et al., 2017) and small-scale (French et al., 2019) structures in the solar corona. For the Fe XIII emission observed by CoMP, linear polarisation (normalised by measured intensity, $P = \sqrt{U^2 + Q^2}/I$) is proportional to $P \propto 3\cos^2\theta_B - 1$ (Casini & Judge, 1999; Judge, 2007; French et al., 2019), where θ_B is the POS angle between the center of the incident solar radiation and local magnetic field. Therefore, P varies between a maximum value at $\theta_B = 0$ (i.e. a radial

field), to a minimum of zero at $\theta_B = \theta_{VV} = 54.74^\circ$, where θ_{VV} is the 'Van Vleck' angle. The maximum P value at $\theta_B = 0$ is determined by the density and temperature of the emitting plasma, and the local anisotropy of incident radiation from the solar disk. θ_B can be estimated with a 90° ambiguity through $\theta = \frac{1}{2}\arctan(U/Q)$, where θ is the polarisation angle.

In French et al. (2019) and the Chapter 3 of this thesis, CoMP observations of the 10th September flare revealed a region of low polarisation ($P \approx 0.01$), aligned with the plasma sheet in EUV. Such a small P value cannot result from depolarising particle collisions, as density effects are not sufficient. We concluded that depolarisation occured through unresolvably small variations in θ_B. Comparing the data with exploratory models using the Coronal Line Emission (CLE; Judge & Casini, 2001) code, we determined the polarisation signature is most likely a result of reconnection turbulence or plasmoid instabilities, four hours after the flare onset.

Figure 4.8 presents CoMP data from 11th September 2017, averaged over 8 images between 17:41 – 18:47 UT. The Fe XIII 1074.7 nm line observed by CoMP has a formation temperature of 1-2 MK (Judge, 2010), mapping well to the 1.25 MK EM plasma shown in Figure 4.7. The CoMP intensity (I) maps shows the flare loops above the occulting disk, which were only just visible 24 hours earlier in the 10th September observations (French et al., 2019). The K-Cor cusp shape is overlaid on CoMP I in Figure 4.8C. Unlike white light pB, CoMP I only observes the brighter flare loops with electron temperatures favorable to Fe XIII emission. Taking a cross-section in two locations above the flare loops (Figure 4.8D), we do not see any clear structure. This observation is compatible with the lack of a plasma sheet signature in CoMP I on 10th September 2017, despite its presence in EUV and CoMP P.

CoMP P is shown in Figure 4.8E. Within the bright post-flare loops we have a low linear polarisation structure, likely a result of depolarisation due to collisions with thermal electrons and protons. Although there is slight variation of P along the loops, the lack of dependency on field direction (assuming the loops trace the magnetic field), indicates a mix of θ_B along the LOS down the flare loop arcade.

Above these obvious post-flare loops, we see a subtle, darker triangle-like structure, aligned to the center of the bright cusp feature in K-Cor *pB* data. The structure is also consistent with the last EUV observations made of the plasma sheet, in 10 MK DEMs (Figure 4.7) on September 11 at 02:00 and 10:00 UT. Taking a cross-section through this darker region, we find a minimum P value of 0.03, from a maximum of 0.06 and 0.075 to the north and south of the feature respectively. Two sample cross-sections are shown in Figure 4.8F. As seen in the K-Cor data, the polarisation vectors show that the field in the region is deflected towards the south. This deflection explains the asymmetry in the P cross-section, as southwards-pointing fields are orientated further from the radial direction at the north of the plasma sheet, resulting in a lower polarisation value.

Using the density sensitive intensity ratio of Fe XIII 1079.8 to 1074.7 nm (French et al., 2019) and taking into account the contributions from radiative excitation with CLE, we estimate the density of 1-2 MK plasma above the flare loops (at $1140''$) to be 1.3×10^8 cm^{-3}. In the associated CLE calculations, we built a new plasma sheet model that includes a laminar field aligned parallel and anti-parallel to the the plasma sheet observed by K-Cor, as in the previous chapter. Using the density estimate at $1140''$, the model yields a minimum polarisation of $P \approx 0.05$ in the plasma sheet. This is greater than the minimum of $P \approx 0.03$ observed in the September 11 CoMP observations. Just as with the 10th September 2017 observations, we interpret this low P value to be a result of structured magnetic field (varying θ_B) in the LOS and POS on sub-pixel scales (French et al., 2019). The increase of polarisation between 10 and 11 September is consistent with continued presence of magnetic reconnection instabilities, embedded in a more laminar magnetic configuration as the system loses free magnetic energy.

4.6 Discussion

We have analysed previously unpublished EIS data from three hours after the flare onset at 15:44 UT. Similarly to EIS observations from the impulsive phase, we find high non-thermal velocities at the base of the plasma sheet, consistent with the

presence of sub-resolution plasmoid-modulated reconnection or turbulence (Warren et al., 2018). (Although alternative interpretations of the non-thermal velocities are possible, e.g. the sources of broadening outlined in Section 1.2.2, this interpretation is consistent with additional evidence presented in Cheng et al., 2018; French et al., 2019). These velocities, 80 km/s at 19:23 UT, are only marginally lower than the velocities early in the flare at 16:18 UT, implying that the non-thermal processes are active at a similar level at this time. As noted in Polito et al. (2015) and Polito et al. (2018a), enhanced line widths can also be produced by a rapid increase in ion temperatures. Interpreting the excess widths measured by EIS in these terms would imply an effective ion temperature in the range of 40 MK, which is more than twice the Fe XXIV peak formation temperature and electron temperatures measured using line ratios in the lower plasma sheet at this time. This assumes that ion and electron temperatures are equal in this case, which, as discussed earlier may not always be true (Kawate et al., 2016). Work by Dudík et al. (2016) and Polito et al. (2018a) demonstrates that non-equilibrium ionisation and non-thermal particle distributions may lead to ions being formed at much higher temperatures than expected, which could in turn contribute to a broader line profile. Further analysis of the line profiles and their variation with position and magnetic field orientation may help in quantifying the contribution of such effects.

These non-thermal velocities, combined with the low polarisation structure in 10th September 2017 CoMP measurements presented in French et al. (2019), suggest that significant reconnection instabilities are likely still present on 10th September 2017 at 20:00 UT. Additional observations during this period are also consistent with signatures of impulsive energy release, within the context of the standard eruptive flare model. As we look down the flare loop tunnel under the erupting flux rope (Chen et al., 2020), we see RHESSI HXR signatures at the loop tops as high energy particles from the plasma sheet above collide with the closed loops. We also find Doppler signatures in EIS measurements of down-flowing (presumably cooling) plasma along the reconnected loops, with subsequent loops forming at increasing altitudes as reconnection continues to take place.

Using RHESSI HXR, high resolution IRIS imaging, AIA and XRT, we are able to track the growth of flare loops with time from plasma with diverse thermal conditions, establishing that the flare evolution displays the classical signatures of cooler plasma in more relaxed loops, and hotter plasma in a tighter cusp shape. Although signatures of ongoing reconnection many hours after flare onset have been seen before (e.g. Savage et al., 2010), the observations here indicate that this cusp feature is still seen with a plasma sheet emanating from its looptop, up to 16 hours after the flare onset, with significant plasma still at temperatures of 10 MK. The presence of these structures, together with the persistent presence of HXR emission at high altitudes is a strong implication that fast magnetic reconnection is still occurring in this case. Observations of long-lived γ-ray emission observed by FERMI provide evidence of particle acceleration over similar timescales (12 hours, Omodei et al., 2018), consistent with this interpretation.

On even longer timescales, we examined K-Cor pB and CoMP linear polarisation measurements from over a day into the flare's evolution. At this time, K-Cor observed a much larger cusp region and apparent plasma sheet deflected towards the south (the direction of which is also seen in earlier DEM measurements). The EUV and white-light plasma sheet structure is also consistent with linear polarisation measurements from CoMP at 10th September 2017 17:41 UT, where low levels of polarisation at the base of the suspected sheet can only be accounted for by sub-pixel magnetic structure in the LOS and POS, implying the continued presence of magnetic reconnection. The fact that infrared linear polarisation measurements can detect signatures of reconnection in this way, despite no visual signatures in EUV, has exciting implications for off-limb flare observations from the DKIST CRYO-NIRSP instrument. It emphasises the need to complement EUV capabilities with optical/IR instruments capable of measuring structure from the solar surface to a few solar radii.

4.7 Conclusion

The 10th September 2017 flare has been extremely well studied, but most studies have so far focused primarily on the impulsive phase of the event. In this work we have shown that the dynamical energy release signatures and flare configuration associated with the impulsive phase of the standard eruptive flare model are still present many hours into the flare's evolution, indicating that in this case fast reconnection is likely still occurring at least 27 hours after the flare onset. This interpretation supports the results of French et al. (2019) and the previous chapter, which indicated that the presence of magnetic sub-structure within the main plasma sheet is consistent with the presence of unresolvable plasmoids and/or turbulence, only 4 hours after the flare onset. These observations suggest that there is still much to be learned from the evolution of what is quickly becoming one of the most-studied solar flares of all time.

Chapter 5

Probing Current Sheet Instabilities from Flare Ribbon Dynamics

This chapter is based on work from French et al. (2021).

5.1 Introduction

As discussed in previous sections, current sheets are notoriously difficult to observe directly, primarily due to the low density and small width of the region. Heated regions of plasma around current sheets (known as a plasma sheet) can occasionally be observed off-limb, but the rarity of their observation means that spectroscopic and multi-wavelength observations, needed to truly disentangle the energy release process (and relationship with instabilities and plasma turbulence), are rare. The 10th September 2017 plasma sheet, examined heavily during the previous two chapters of this thesis, is perhaps the most successful spectroscopic plasma sheet observation set to date, observed by multiple instruments across the entire electromagnetic spectrum. These observations facilitated insight into the nature of magnetic reconnection in the event, and providing initial evidence for the presence of turbulent or tearing-mode reconnection (Cheng et al., 2018; French et al., 2019), persisting for the flare's entire duration (French et al., 2020). Although observations of this 10th September 2017 event provided many new insights into the behaviour of current sheet dynamics, the uniqueness of such a dataset requires alternative methods to be employed to other flare observations in order to make further progress in

understanding these processes.

On-disk observations of flares are far more common than those of flares at the limb. This is because active regions can be observed for far longer durations traversing the disk than passing over the limb, providing a higher probability of observing a flaring event. Off-limb observations, particularly over the eastern limb, face additional challenges in observation planning that make observations less frequent.

Plasma sheets of on-disk flares are rarely observed, primarily due to the lack of contrast between the heated sheet structure and the bright background active region plasma. However, although we may not observe these features directly, we still expect them to be there. The field line connectivity between these reconnecting current sheets in the corona, and flare ribbon features on disk, offer a possibility for further study.

Insights into current sheet dynamics can be revealed by the behaviour of flare ribbon substructure, as magnetic reconnection accelerates particles down newly reconnected field lines into the chromosphere to mark the flare footpoints. Due to this magnetic connectivity, behaviour of flare ribbon substructure must reflect processes in the flaring current sheet region (Forbes & Lin, 2000). During a solar flare, high energy particles are accelerated from the reconnection site down the flare loops to the chromosphere, depositing energy at the magnetic footpoints to form flare ribbons (Cheng et al., 1983; Doschek et al., 1983). Due to energy transport and deposition processes between the reconnection site and chromosphere, we can never expect to trace individual pristine structures of plasma travelling between these two regions. However, flare ribbons can provide some insight into the processes occurring within the current sheet. For example, observational studies of flare ribbons have found spectroscopic signatures suggestive of waves and/or turbulence (Brosius & Daw, 2015) - consistent with the presence of either the tearing mode or Kelvin-Helmholtz instability in the current sheet (Brannon et al., 2015). These signatures of energy release in the chromosphere are detected on as fine a scale as $\sim$ 150-300 km (Graham & Cauzzi, 2015; Jing et al., 2016).

In this study, we use high-cadence (1.7 s) IRIS Slit Jaw Imager observations

to probe for the growth and evolution of key spatial scales along the flare ribbons - resulting from dynamics across the current sheet of a small solar flare on 6th December 2016. This is novel analysis, and has not been done before for flare ribbon observations. Combining analysis of spatial scale growth with Si IV non-thermal velocities, we piece together a timeline of flare onset for this confined event, and provide evidence of the tearing-mode instability triggering a cascade (to smaller scales) and inverse cascade (to larger scales) towards a power spectrum consistent with plasma turbulence.

5.2 Magnetotail Analogy

The Earth's magnetotail experiences similar cycles of energy storage and release (Akasofu, 1964; McPherron, 1970) to those observed in flares. The energy builds in the Earth's magnetotail until it reaches a point of instability, at which point the energy is explosively released through reconnection (Hones et al., 1984), causing observable phenomena such as the rapid brightening of the aurora (Akasofu & Lepping, 1977) (analogous to flare ribbon brightening on the Sun), and the formation of auroral beads (Henderson, 1994, 2009). Fourier analysis of auroral bead brightenings along the auroral arc has found that specific spatial scales grow exponentially (Rae et al., 2010; Kalmoni et al., 2015). Recently, high temporal and spatial resolution measurements of the aurora enabled the comparison of observation and theory to show that non-local effects, in the form of sheer Alfven waves, were responsible for plasma instabilities in near-Earth space (Kalmoni et al., 2018).

Although fundamentally different in their temperature, density and collisional timescales, there are distinct similarities between flare ribbons and terrestrial aurorae driven by sub-storm activity. In this study, we take inspiration from the magnetospheric work of Kalmoni et al. (2018), applying the auroral beads methodology to flare ribbons of a small solar flare, to determine whether similar evidence exists for the presence of a plasma instability at flare onset.

5.3 Observations

We present IRIS (section 2.3) observations of a confined B-class flare in the core of AR 12615 on 6th December 2016. IRIS observed with a *large sit-and-stare* Slit Jaw Imager (SJI) 1400 Å window, and a 1.7 s cadence. With just the one slit-jaw channel, this is close to the fastest cadence IRIS can observe. The SJI observations were 2x2 binned, resulting in a pixel width of $0.3327''$ or 238 km. IRIS observed the flare continuously from pre-flare to decay.

Figure 5.1 (top row) presents snapshots of the SJI 1400 Å evolution, with the field of view cropped to centre on the two flare ribbons. From hereon, the two ribbons will be denoted as the *east* (left) and *west* (right) ribbon. Examining the light curve of each region, we see the two ribbons brighten cotemporally, and although the east ribbon is significantly larger than the west, maximum intensities are comparable. Similar maximum intensities imply a similar level of energy deposition in each ribbon.

The brightest ribbon regions are also observed in the 131 Å channel of SDO-AIA (section 2.2.1). Following peak ribbon intensity, higher-altitude flare loops become visible in this channel as they fill with hotter ablated chromospheric material. The timing of these events is shown in Figure 5.1. Looking at the photospheric LOS magnetic field measurements (B) in this region from HMI (section 2.2.2), we see the flare ribbons (marked by red contour) appear either side of the polarity inversion line, adjacent to the regions of highest field strength (third row of Figure 5.1). At around $600''$ from centre disk, projection effects have begun to affect the west of the HMI observations. Although the area traced by the ribbons change throughout their evolution, the photospheric field itself does not vary on the timescales studied. Examining the LOS magnetic flux traced by the evolving (SJI 1400 Å) ribbons in the bottom-right panel of Figure 5.1, we note that the flux is equal in each ribbon throughout the flare. That is,

$$B_E A_E = B_W A_W. \tag{5.1}$$

Matching flux in each ribbon implies connection of the two via a consistent

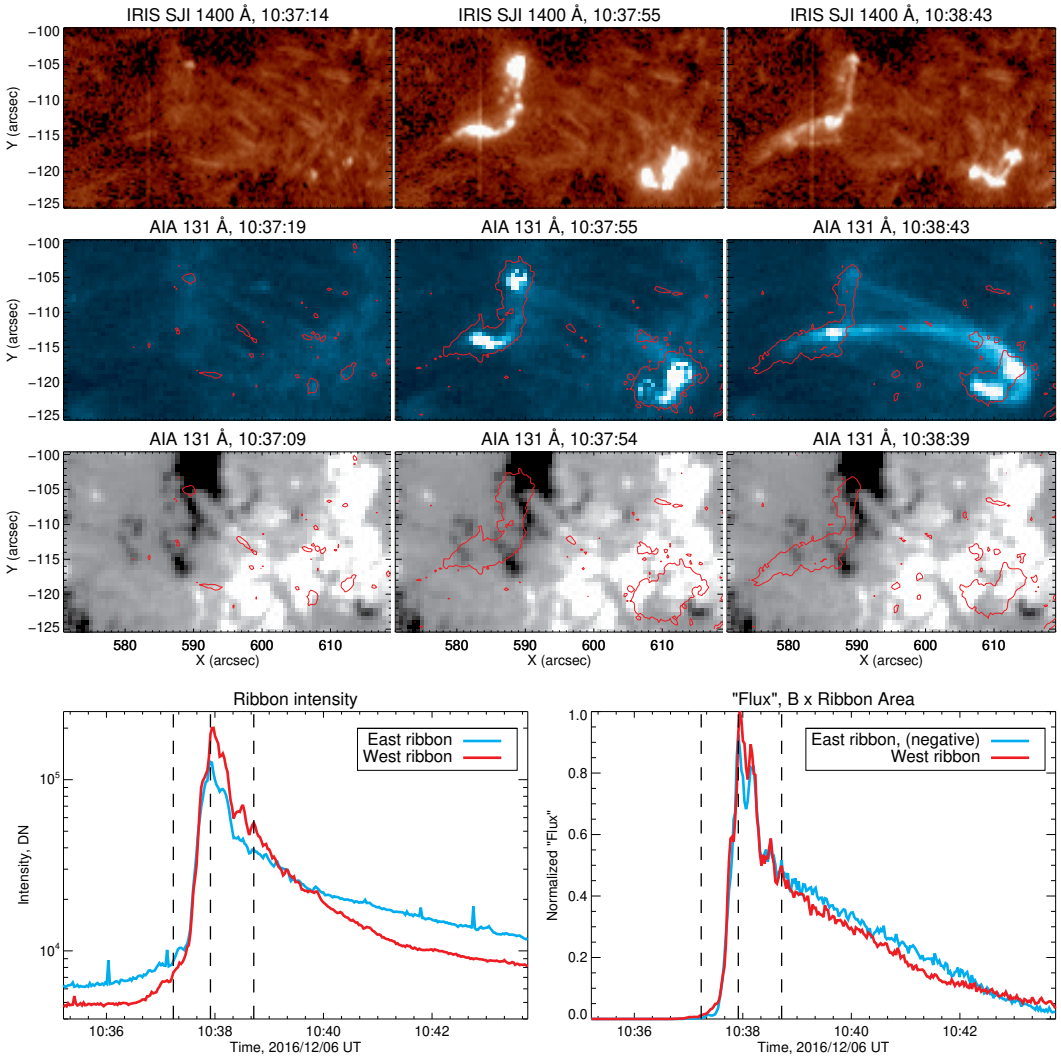

Figure 5.1: Top: Evolution of IRIS SJI 1400 Å. Second row: Evolution of AIA 131 Å, with IRIS ribbon contours to distinguish emission at high/low altitudes. Third row: Evolution of HMI LOS B field, with IRIS ribbon contours. Bottom Left: Ribbon light curve, of masked region in Fig 5.2. Vertical dashed lines mark location of above panels. Bottom Right: Ribbon area over intensity threshold, multiplied by HMI LOS field strength in each region. This is analogous to magnetic flux ($B \times A$) evolution within the bright ribbon region. East ribbon flux is multiplied by -1.

tube of flux, which does not interact significantly with any external field. We can therefore imagine this flux tube passing from one ribbon to the other, containing the reconnection regions within it. The flare is likely a result of quadrapolar reconnection (Melrose, 1997; Pikelner & Livshits, 1977), with, due to the small size of the event, footpoints of equal polarity merging together to form one ribbon feature either side of the polarity inversion line. We therefore expect the reconnecting current sheet to be somewhere between the flare loops - perhaps even those seen in AIA 131 Å. The Active Region is complex however, and other flaring configurations are possible. One other possibility considered was the circular ribbon flare (Wang & Liu, 2012), which would feature null point reconnection instead of the more-traditional laminar current sheet. In this scenario, null point reconnection still contains layers of current and thus would still be subject to instabilities (Pontin, 2011). This method does therefore not require the precise location/topology of the reconnecting current sheet to be known.

Spectral data of the flare ribbons were collected by the IRIS sit-and-stare slit, centred across the larger (east) ribbon. The position of this vertical slit can be seen as a slight enhancement in SJI image intensity. Jeffrey et al. (2018) examine the spectral evolution of this flare ribbon, finding a steep rise in the non-thermal velocity of the optically-thin Si IV 1402.77 Å line. This was interpreted as a signature of plasma turbulence, preceding the rise in Si IV intensity (marking plasma heating flare onset).

In this study, we examine the spatial and temporal evolution of the two ribbons in SJI 1400 Å observations, investigating the power spectra in the spatial domain along the ribbon to provide insight into processes across the current sheet, perpendicular to the magnetic field. We compare the power spectra at multiple spatial scales with parameters predicted by theory, and the timings of the Si IV non-thermal velocities introduced by Jeffrey et al. (2018). When studying the ribbon spatial intensity evolution, we are not restricted by the slit location and can therefore analyse both ribbons independently. Current sheet processes may also affect structure across the ribbon, in addition to the variation along the ribbon we probe in this

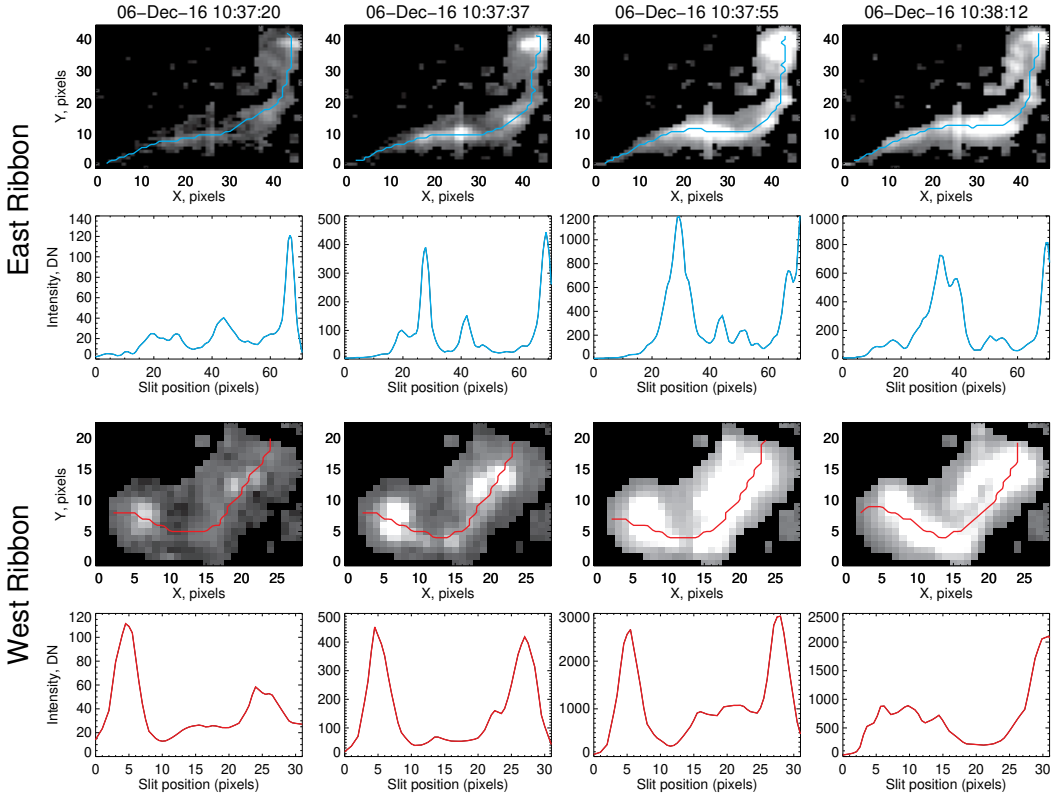

Figure 5.2: Top: Evolution snapshots of the East ribbon tracking. Second: Intensity cross-sections along the centroids of the east ribbon (marked in top row). Third: Evolution snapshots of the West ribbon tracking. Bottom: Intensity cross-sections along the centroids of the west ribbon (marked in third row).

study. Analysing these components together, along with the time-varying component, would provide the full dispersion relation, but not possible with the resolution of this data set. We therefore focus exclusively on searching for spatial scales along the flare ribbon structures.

5.4 Ribbon Power Spectrum

5.4.1 Ribbon Tracking and Intensity Processing

In order to investigate intensity variation along the flare ribbons, we developed a method to track a centroid along each flare ribbon as they evolved in space and time. This method, and all subsequent analysis, is repeated separately for both the east and west ribbon.

To begin, we produced a mask to remove all pixels never crossing an intensity

threshold (that never form part of the ribbon structure). Next, we take cross-sections perpendicular to the main ribbon structure, and locate the position of the brightest pixel at each of these cross-sections. We then take a moving average of the pixel locations from this initial estimate, producing a smooth, continuous centroid slit along the centroid of each ribbon. These centroids change as the ribbons evolve, and sample snapshots of the evolution of each ribbon are shown in Figure 5.2. The main tracking limitation is the spatial resolution, as each centroid position must still have an integer pixel position. The tracking method works effectively however, capturing the change in curvature of the ribbons as they evolve.

We measure the intensity cross-section along the ribbons, by taking the mean intensity of a 3x3 pixel area around each pixel location in the centroid slit. Measuring an average around each pixel provides a more reliable estimate of intensity along the centroid (by not relying on a single pixel measurement), and reduces the impact of higher intensities in the slit-jaw image at the sit-and-stare slit location. Intensity measurements along this centroid are not uniformly spaced, dependent on whether adjacent pixels in the centroid lay horizontal/vertical or diagonally to one other. We interpolate along this centroid to create an evenly spaced array - necessary to calculate a Fast Fourier Transform (FFT). Example cross-sections for each ribbon are shown in the second and bottom rows of Figure 5.2. Here, we have converted position along the centroid into units of Mm. The east ribbon is over twice as long as the west, with centroid slit lengths of 17 and 8 Mm respectively. The intensity signal displayed here is then processed by detrending the data with a moving average, to avoid intensity jumps between the centroid slit ends dominating the power spectrum. The moving average sizes were selected manually, to remove large general trends in the data without inadvertently subtracting the smaller variations we aim to detect. Finally, we apply a Hanning Window to the data and introduce zero padding, to preserve the power and increase the spectral resolution of the Fast Fourier Transform (FFT). The modulus of the FFT returns the power at spatial scales at intervals of L/2, L/3... L/n, where L is the length of the array in real units and n the number of data points. Zero padding therefore increases the spectral

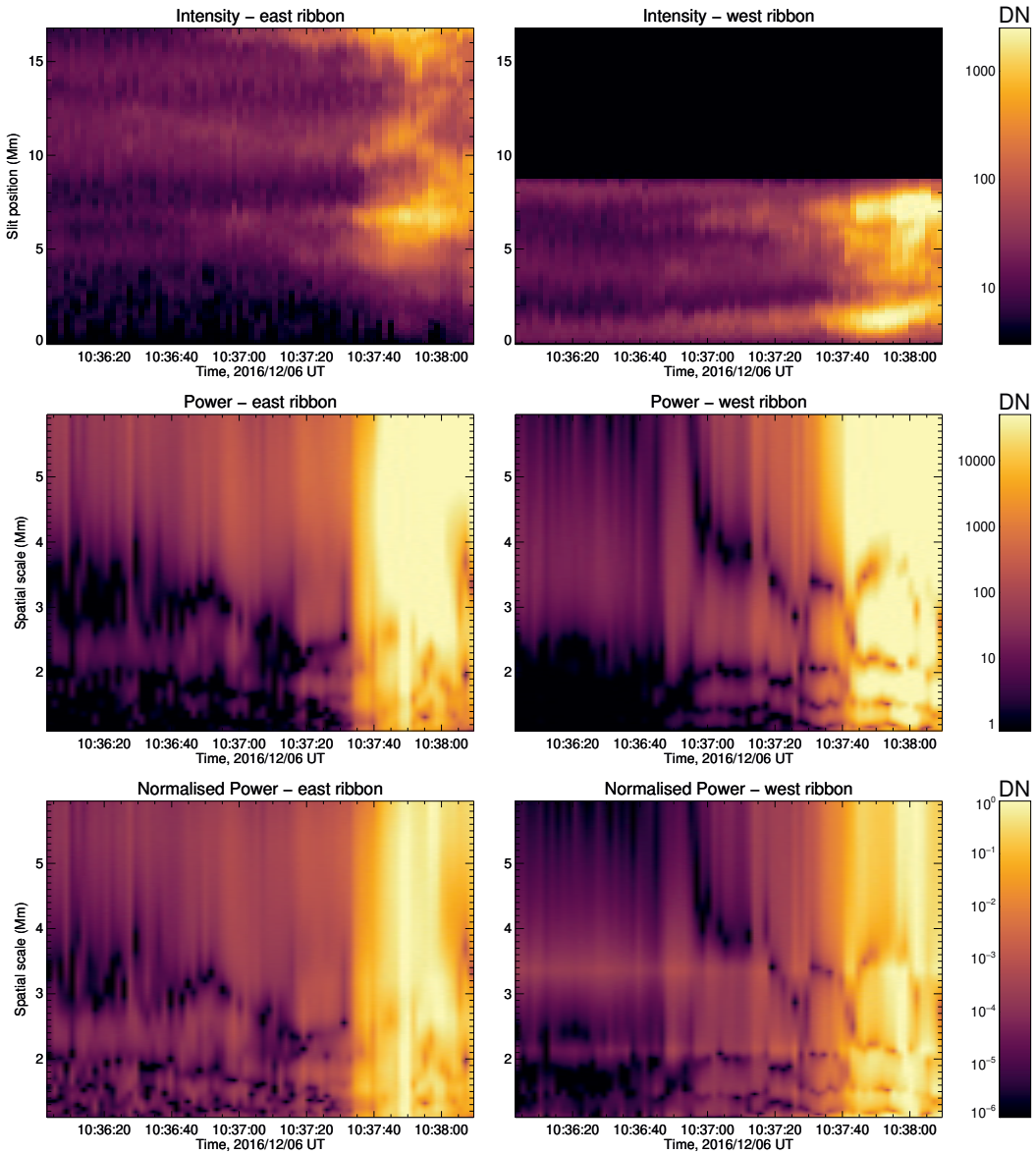

Figure 5.3: Top: Ribbon intensity stack plots for both ribbons. Middle: Spatial scale power stack plots. Bottom: Spatial scale power stack plots, normalised at each spatial scale. All y-axes in units of Mm. (0.33 arcsec).

resolution of the FFT by calculating the power at smaller intervals (n is larger), as well as minimising the effects of aliasing. Hanning windows decrease the intensity at the start and end of the data array, to avoid large 'jumps' between these data values dominating the power spectrum.

5.4.2 2D Power Spectrum

Intensity cross-sections along the ribbon centroid are measured and processed for every 1.7 s time step, producing the intensity stack plots in the top row of Figure 5.3. For each of these cross-sections (vertical slices along the stack plot), we calculate the FFT of ribbon intensity, resulting in the power spectrum in the spatial domain for each time step. This provides us with the power of different spatial scales appearing along the flare ribbon. These spatial scales (in Mm) are inverse to the dispersion relation wavenumber, k, often used in the literature. We elect to work with units of spatial scale for this study, as they are easier to picture in this instance. We combine each spatial FFT into a single stack plot, presented in the middle row of Figure 5.3 for each ribbon. Maximum power varies significantly with spatial scale, so to better see time evolution at each spatial scale we normalise the power spectrum in time, to produce the bottom panel of the same figure. Between 10:37 and 10:38 UT, we see a steep rise in power across all spatial scales, with growth rate and onset times varying across different scales. Before this time, we see consistent signals at certain spatial scales - around 2.5 Mm in the east ribbon (with a potential second, weaker peak higher around 5.5 Mm), and 2 and 3.5 Mm in the west ribbon. These signals result from the spacing between bright points in the pre-ribbon structure. This spacing can be verified by studying the intensity stack plots in the same figure, with the spacing between the bright horizontal features.

5.5 Spatial Scales and Exponential Growth

5.5.1 Flux Conservation - Spatial Scaling

If the observed spatial scales in the flare ribbons result from processes propagating down from the reconnection site, we can expect the length scales to scale with the square root of the area of the flux tube connecting the two ribbons. (Picture a wave

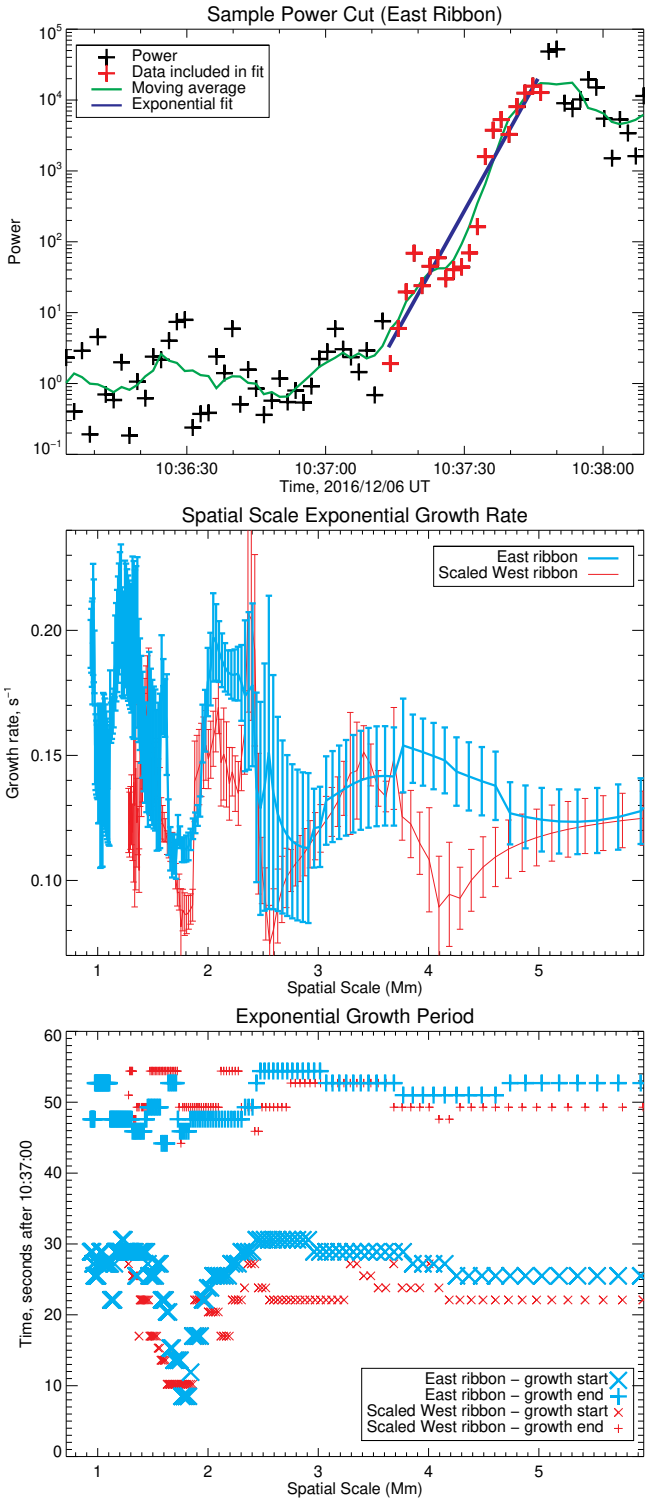

Figure 5.4: Top: Cross-section through power plot (Fig 5.3) at spatial scale of 1.75 Mm, showing exponential growth. Middle: Exponential growth rate at each spatial scale. West scales are transformed to east scales. Bottom: Start/end times of the fitted exponential period, for the east and scaled west ribbon spatial scales.

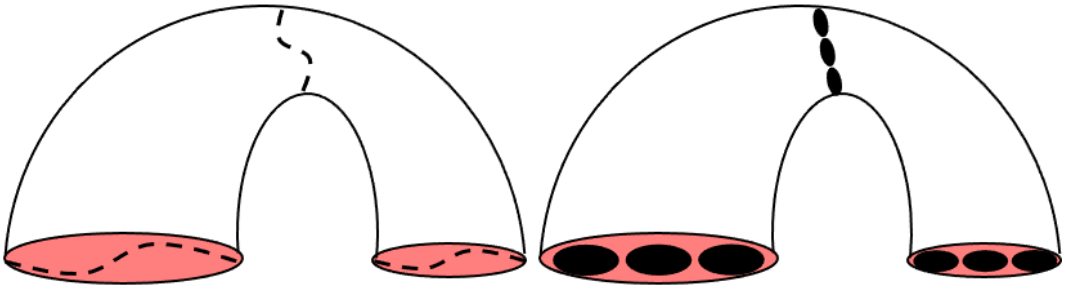

Figure 5.5: Cartoon to demonstrate how spatial scales of waves and magnetic structures will grow with an expanding / contracting tube of flux. Cartoon is not to scale, and does not necessarily resemble an increase in flux tube area from top to bottom.

with one mode, perpendicular to the magnetic field direction. As the area of the flux tube changes, the wavelength scale approximately changes by the square root of the area). Considering the flux conservation shown in Figure 5.1, we can equivalently scale the length scales through the ratios of magnetic field strength (equation 5.1). Figure 5.5 shows a quick demonstration of this, how, given that flux is conserved along the tube, waves and magnetic structure will expand and contract with the flux tube.

As magnetic conditions vary along this tube of flux, we can apply this concept to compare the spatial scales seen at each ribbon, by scaling the west ribbon scales to the 'reference frame' of the east ribbon through the square root of the ribbon area ratios. The analysis below considers the original and scaled spatial scales observed in the east and west ribbon respectively.

5.5.2 Growth with Spatial Scale

In MHD, exponential growth at multiple spatial scales is a classical signal of plasma instability (Priest, 1985). We investigate the growth at a specific spatial scale by taking a horizontal cross-section through the power spectrum in Figure 5.3 - tracking the evolution of power with time. Figure 5.4 (top panel) presents an example cross-section for a scale of 1.75 Mm in the east ribbon. The plot shows a noisy baseline power around 10^0, which sharply increases by nearly 5 orders of magnitude between 10:37:10 and 10:37:50 UT. We determine the region of exponential growth in the data moving average, and fit an exponential curve to the corresponding data

points. This provides us with an exponential growth rate and start/end times of the exponential phase.

By fitting an exponential curve for each spatial scale, we calculate the variation in the start time, duration and rate of the exponential growth of different spatial scales in each ribbon. The east ribbon growth rates are shown as the cyan curve in the middle panel of Figure 5.4. The curve shows three peaks around 1.2, 2.3 and 3.8 Mm, before tailing off at high spatial scales. The error bars in this plot assume that the algorithm determining the start/end point of exponential growth was correct within one data point. With error bars considered, the plot is continuous with no major jumps in the data. The growth rate itself varies by a factor of $\sim 2-3$, between $\sim 0.09-0.24\ s^{-1}$. The scaled west ribbon scales provide a good alignment with the east ribbon, and the locations of the three peaks match reasonably well.

We also plot the duration of exponential growth at each spatial scale for the east and west ribbon in Figure 5.4 (bottom). Examining the east ribbon data, we see exponential growth start initially at a single spatial scale (the 1.75 Mm scale plotted previously), before beginning at all other scales up to 19 seconds later. This is suggestive of a process at a specific spatial scale causing the growth at progressively shorter and longer scales through a cascade and inverse cascade. The west ribbon produces noisier data (due to fewer data points along the ribbon) - but still shows exponential growth beginning first at the same spatial scale of 1.75 Mm. The end times of exponential growth are not captured as clearly by the algorithm. Detecting key spatial scales independently in both ribbons provides confidence that the processes causing the features are likely linked - that is, they both originate from instability processes at the reconnection site.

The east ribbon does not trace the strongest photospheric field of the active region, resulting in a fairly low mean LOS field strength of 107.5 Gauss. We do not expect the magnetic field of active region loops (Brooks et al., 2021; Landi et al., 2021) to be significantly lower than this photospheric measurement. Considering again flux conservation, and that the length scales scale with the square root of the field strength ratios - the spatial scales of these processes at the reconnection site

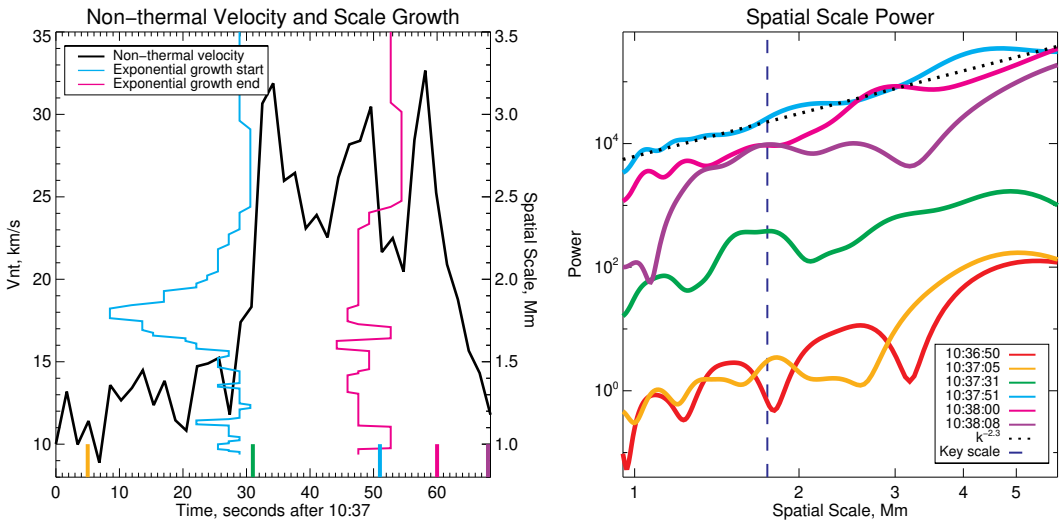

Figure 5.6: Left: Comparison between the non-thermal velocity timing, with the start and end of exponential growth at different spatial scales (in the east ribbon). Vertical ticks on the x axis mark the times shown in the right panel. Right: East ribbon spatial power spectra at key times, compared with a power-law distribution.

(in the active regions loops) will not be much larger than the scales observed in the flare ribbons (of order 1-10 Mm).

5.6 Discussion

The analysis of intensity variations along the flare ribbons provide insight into the dynamics of the reconnecting current sheet. Our analysis has provided us with observational constraints, allowing us to compare the observed parameters with those predicted by reconnection instability theory. The main constraints are -

- Exponential growth is seen across all wavelengths, with preferred scale at 1.75 Mm.
- Exponential growth rate is in the order of $\approx 0.1 - 0.2$ s^{-1}.
- Spatial scale growth times suggest a cascade and inverse cascade.

In Tenerani & Velli (2020), the authors use 2.5D simulations to study the nonlinear phase of tearing modes within a current sheet. The authors find growth beginning at a specific wave mode, before leading to growth at lower and higher modes

(higher and lower spatial scales) through a simultaneous cascade and inverse cascade. The combination of cascades to higher and lower spatial scales simultaneously comes from the interplay of magnetic island collapse and coalescence. The exponential growth rates in Tenerani & Velli (2020), ≈ 0.45 s^{-1} are also on the same order of magnitude as our observations. The specific properties of the tearing mode instability within this simulation are consistent with our observations. In particular, the cascade/inverse cascade, which we would not expect from other instability processes (such as Kelvin Helmholtz), suggests there is more at play than just turbulence. We therefore conclude that the flare ribbon spatial scale growth reflects the presence of the tearing mode instability in the current sheet.

With a higher spatial resolution, or larger flare with more data points along the ribbon - it would be possible to measure the power at further larger and smaller wavelengths. This would potentially allow for the measurement of a more complete dispersion relation, including the time variation (ω) and second k (variation across the ribbon) component, to allow further comparison with tearing mode theory.

5.6.1 Flare timeline

Assuming that exponential growth at our key spatial scale is the signature of tearing mode instability onset, we can compare this with the other observed parameters for this same event. Jeffrey et al. (2018) find that the rise in non-thermal velocity, believed to be a signature of turbulence at the flare ribbon slit location, preceded the intensity increase associated with plasma heating and flare onset. The authors note that there must be a driver for this long-lived turbulence signal. High-cadence IRIS observations of other small flares have found a similar pattern of enhanced non-thermal velocities preceding rises intensity - consistent with signatures of turbulent reconnection in the current sheet (Chitta & Lazarian, 2020). Comparing the timing of the non-thermal velocities with the growth of spatial scales in Figure 5.6 (left), we find growth at our key scale of 1.75 Mm begins some 15 seconds before the growth in non-thermal velocities. Similarly, the end of exponential growth across all spatial scale occurs a similar time frame before the drop of non-thermal velocity. This suggests that for this event, the tearing mode instability is the driver of

plasma turbulence in the region, as a result of the cascade and inverse cascade to progressively smaller and larger spatial scales.

Further evidence to support the breakdown to turbulence via a(n) (inverse) cascade can be found by examining the power spectra for specific time frames (taking a vertical cross-section through the middle row of Figure 5.3). Cross-sections at important moments are shown in Figure 5.6 (right), and are as follows:

- 10:36:50 - Large oscillations in the low-amplitude power spectra, equivalent to the harmonics of the bright points in the pre-flare ribbon region.
- 10:37:05 - Key scale of 1.75 Mm appears for the first time.
- 10:37:13 - Exponential growth begins at the key scale (shown in left panel of Figure 5.6).
- 10:37:31 - Exponential growth is well underway across all spatial scales, lead by the key 1.75 Mm scale. The non-thermal velocity begins to rise at this time.
- 10:37:51 - Power spectra have reached their peak, with all scales catching up to the key scale to produce a power law index of $\approx k^{-2.3}$.
- 10:38:00 onwards - Power law starts to break down, with a falling amplitude and local maxima/minima forming. Non-thermal velocity is also returning to background levels.

At the peak of the power spectra, the spatial scales form a power law index of approximately 2.3. A power law in this domain is a key prediction in plasma turbulence, routinely seen in in-situ measurements. In the classic Kolmogorov-like distribution of turbulence (Kolmogorov, 1941), the power law is predicted to evolve to an end-state of 5/3 - slightly lower than our observed value of ≈ 2.3. There are two likely explanations for this disparity. Firstly, it is possible that the tearing mode process did not persist for long enough to drive the power law to the predicted Kolmogorov end-state of 5.3. Or, an alternative turbulence model is a better fit

for these conditions. Tenerani & Velli (2020), for example, predict a power-law index of 2.2, when introducing a model of intermittency (Frisch et al., 1978) to the collapsing magnetic islands and beginning from a Kolmogorov state. Dong et al. (2018) also find an index of 2.2, in their simulation of a plasmoid-mediated regime.

By comparing the power spectrum and non-thermal velocity evolution with the timing of exponential growth onset, we have provided evidence for the tearing-mode instability manifesting itself before plasma turbulence - similar to that expected by simulation work, e.g. Dong et al. (2018); Tenerani & Velli (2020). As shown in Jeffrey et al. (2018), the turbulence itself precedes the ribbon intensity enhancements and flare onset. We thus have extended our knowledge of the pre-flare timeline for this single event, and provided insight into the nature of current-sheet collapse and onset of fast-reconnection via MHD instabilities in a solar flare.

5.7 Conclusion

A major open question in solar flare physics is the sequence of events that lead to the onset of the fast reconnection that is widely acknowledged to cause the impulsive energy release. Central to this question is the formation and disruption of the current sheet in which reconnection occurs. Current sheet formation can occur through a variety of processes that include large scale MHD instabilities that are a key element of eruptive flare models (e.g. Green et al., 2018, and references therein), but also as the result of MHD turbulence. The subsequent evolution of that turbulence can then lead to its disruption through the onset of the tearing mode instability, which causes the energy spectrum to steepen (Dong et al., 2018). The issue of the interplay and feedback between reconnection, turbulence and current sheet disruption is therefore complex, but critical to understanding flare onset.

For the event studied here we find evidence to support the development of the tearing mode instability prior to the first detectable signatures of turbulence, followed by the subsequent evolution of the energy spectrum to a power-law dominated regime with slope ≈ 2.3. While we cannot completely rule out the existence of turbulence prior to the tearing mode onset that we are just unable to detect with

the available data, our analysis strongly suggests current sheet formation by another mechanism, e.g. at the interface between emerging and pre-existing magnetic fields. The subsequent evolution of the instability and turbulent energy spectrum is consistent with previous work by Dong et al. (2018) and Tenerani & Velli (2020) that supports the presence of the combined effects of dynamic alignment of the magnetic islands (or plasmoids), intermittency and recursive reconnection.

In conclusion, we find that for case study presented here the flare onset is precipitated by current sheet formation, leading to the onset of the tearing mode instability and subsequent development of a turbulent cascade.

Chapter 6

General Conclusions and Future Work

6.1 General Conclusions

The work in this thesis investigated the nature of explosive energy release within solar flares. In particular, we examine the role of the tearing mode instability during the magnetic reconnection process, for case studies of two solar flares. To do this, we use spectropolarimetry, spectroscopy and imaging across the EM spectrum from a range of ground and space-based instruments.

For the first flare case study, we examine the famous 10th September 2017 X-class event. As discussed in this thesis – plasma sheets, regions of heated plasma around the reconnecting current sheet, are not easy to capture observationally, and are rarely caught in spectroscopic observations. In this regard, the 10th September 2017 flare is truly a unique dataset, observed by such a wide range of instrumentation across its evolution. Using the MLSO Coronal Multi-channel Polarimeter (CoMP), we found a spatially-broad signal of low linear polarisation across the flare's plasma sheet, aligned with the bright structure in EUV emission. By comparing these observations to forward-modelled emission of simple empirical models, we found the low polarisation signature to be compatible with the existence of sub-pixel magnetic field structure, consistent with that expected by magnetic tearing or reconnection-induced turbulence within the plasma sheet. We also find that this po-

larisation signal is long lived, still visible some 24 hours after flare onset, far beyond its visibility in EUV. This finding implies that these critical plasma sheet structures can be visible in IR linear polarisation, even with no clear structure in EUV. We therefore expect plasma sheet observations in IR polarisation to be far more numerous than in EUV. As discussed in the below Future Work section, this work is highly relevant to observations from Daniel K. Inouye Solar Telescope (DKIST) – a 4m aperture solar telescope which recently started science observations. With a higher spatial and temporal resolution, linear polarisation measurements from the instrument may be able to further reveal the presence/location of magnetic substructure (associated with reconnection and turbulent processes) within solar flares.

The presence of the tearing-mode instability in the late-phase of the 10th September 2017 flare is also supported by non-thermal velocity measurements by Hinode/EIS. We found these signals, and other observational signatures of ongoing fast reconnection, to be incredibly long lived in this event. This includes DEM measurements, which find significant contributions from 10 MK plasma over 10 hours from flare onset. This picture of ongoing reconnection supports long-lived γ-ray observations over similar timescales (12 hours, Omodei et al., 2018). This late-phase presence of observable phenomena expected during the impulsive phase of flares, differs wildly from our understanding of the characteristic phases of an eruptive solar flare.

Finally, we diverted our attention away from the X-class event, moving onto a small B-class flare on 6th December 2016. Unlike the 10th September 2017 event, this smaller flare occurred on disk, and thus does not contain a clearly visible plasma sheet region in which reconnection is likely taking place. We do however, utilise the connection between the reconnection site and the chromospheric footpoints – which mark the flare ribbons. Motivated by a study of auroral beads in the terrestrial magnetosphere, we used Fast Fourier Transforms to search for the timing and growth of spatial scales appearing within the flare ribbons. Preceding any significant onset in IRIS Si IV intensity or non-thermal velocity (relating to flare onset and signatures of turbulence), we detected initial growth of a single spatial scale, before detecting

subsequent growth at progressively larger and smaller spatial scales. By demonstrating that the spatial scale evolution relates to a region of the corona connected to the two ribbons, we interpreted the scale growth as evidence of the current sheet collapsing at a specific spatial scale, before producing a cascade and inverse cascade to other scales. This, combined with observed growth rates, match what previous simulation work (e.g. Tenerani & Velli, 2020) predict from the tearing mode instability during reconnection dynamics. The relative timing of the cascade and inverse cascade with the non-thermal velocities suggests that the tearing mode instability is inducing the plasma turbulence observed through the non-thermal velocities. Finally, we are able to validate this link further by detecting a spatial scale power-law domain of ≈ 2.3, close to turbulent power laws observed in 2.5D simulation work of plasmoid-mediated regimes.

Although reconnecting current sheet regions are elusive, we have developed novel techniques to probe the nature of magnetic processes within these crucial regions. For the two flares (of vastly different magnitudes), studied within this thesis, we determine that the tearing mode instability plays a role in the breakdown of ideal-MHD needed to cause fast reconnection within these events. The methodology used in this thesis can be pushed further, as observations from next-generation instrumentation start to become available.

6.2 Future Work

The narrow current sheet is the primary site of magnetic reconnection, causing the magnetic topological changes which subsequently release energy to power flares and accelerate associated CMEs. As we have determined in this thesis, current sheets are notoriously difficult to observe, and creative methods are therefore needed to investigate these regions and processes within them. With DKIST and Solar Orbiter beginning science operations, we are equipped better than ever to study the dynamics of magnetic reconnection within solar eruptions and build on proven methodology from this thesis in the future. Below I discuss how DKIST and Solar Orbiter quadrature observations could build on proven methodology developed

within this thesis. I provide two cases – one for eruptions at disk centre, and one for eruptions at the limb.

• **Case 1: Limb flares**

The coronal Fe XIII lines observed by CoMP, will also be observed by the DKIST/Cryo-NIRSP instrument, with a much higher spatial sampling (albeit over a small field of view). The differences between these instruments are outlined in Table 6.1. The longevity of these polarised plasma sheet structures suggest that Cryo-NIRSP has a good chance of seeing them at the limb. Before this data becomes available, the under-explored existing set of CoMP flare observations should be used to learn more about these structures. Recently, the new UCoMP has resumed observations, so it may also provide additional valuable flare data.

Instrument	Aperture	Observed Parameters	FOV	Pixel Size
CoMP	20cm	Stokes I, Q, U	1.03 - 1.5 $R_\odot$	4.35 $''$
Cryo-NIRSP	4m	Stokes I, Q, U, V	$240 \times 180''$	0.5 $''$

Table 6.1: Comparison between CoMP and DKIST/Cryo-NIRSP instruments

With its higher spatial resolution, Cryo-NIRSP linear polarisation measurements can provide further insight to the sub-pixel dynamics of current sheets, and combined with circular polarisation, they could reveal the evolution of the guide field and the larger-scale active region fields during the eruption. In order to fully utilise Cryo-NIRSP in this way, comparisons to advanced MHD models are needed.

Solar Orbiter observations at or around quadrature would enhance this dataset further. Using extrapolations of magnetogram measurements from the Polarimetric and Helioseismic Imager (PHI) instrument, with flare ribbon observations from the Extreme Ultraviolet Imager (EUI) and Spectral Imaging of the Coronal Environment (SPICE) instruments, Solar Orbiter observations would help build a 3D view of the erupting structure and current sheet.

• **Case 2: On-disk flares** In Chapter 5 I discuss how the connection between the flare ribbons and current sheet can be used to provide insight into flare dynamics. We used IRIS Si IV imaging and spectroscopy to study the flare ribbons of a small, confined flare. Prior to DKIST data becoming available, this work could be

extended to additional IRIS datasets, to explore how the relationship between turbulence and plasma instabilities varies between confined/eruptive flares of various sizes and configurations.

The DKIST Visible Broadband Imager (VBI) instrument will have the temporal resolution to deepen this analysis, with a much higher spatial resolution – allowing the exploration of smaller scales produced up in the reconnecting corona. In addition to this, VBI will be able to observe the flare ribbons at multiple heights in the chromosphere, to reveal how flare energy transport and deposition varies throughout the solar atmosphere. As described in Chapter 5 and French et al 2021, by combining analysis of flare ribbon spatial scales with knowledge of the coronal magnetic conditions, we can calculate the physical scales over which magnetic fields begin to tear during reconnection in the solar corona. This is possible by combining polarimetric DKIST observations with Solar Orbiter at quadrature. Magnetic inversions of the Visible Spectro-Polarimeter (VISP) polarimetric scans and associated extrapolations will be able to reveal the pre/post eruptive magnetic configuration of the active region, whilst the Solar Orbiter Spectrometer Telescope for Imaging X-rays (STIX) and EUI/SPICE instruments can observe the reconnection site and coronal plasma dynamics respectively. This type of observations will allow us to simultaneously study the dynamics of the flare ribbons and current sheets, and their impact on eruption evolution. Furthermore, with its 2D imaging capabilities, the DKIST Diffraction Limited Near Infrared Spectropolarimeter (DL-NIRSP) has the ability to record the spatially co-temporal evolution of magnetic field structure within the flare ribbons.

To fully understand the evolution of energy release and deposition processes throughout the solar atmosphere during an eruption, we must use advanced models to fully interpret the DKIST and Solar Orbiter observations. The synergy of next-generation observations and modelling should enable significant steps in understanding the dynamics and triggers of magnetic reconnection during solar eruptions.

Bibliography

Akasofu, S. I. 1964, *P*lanet. Space Sci., 12, 273

Akasofu, S. I., & Lepping, R. P. 1977, *P*lanet. Space Sci., 25, 895

Alfvén, H. 1942, *N*ature, 150, 405

Antonucci, E., Gabriel, A. H., & Dennis, B. R. 1984, *A*strophys. J., 287, 917

Antonucci, E., Rosner, R., & Tsinganos, K. 1986, *A*strophys. J., 301, 975

Arnaud, J., & Newkirk, G., J. 1987, *A*stron. Astrophys., 178, 263

Aulanier, G., Démoulin, P., Schrijver, C. J., et al. 2013, *A*stron. Astrophys., 549, A66

Aulanier, G., Janvier, M., & Schmieder, B. 2012, *A*stron. Astrophys., 543, A110

Benz, A. O. 2016, Living Reviews in Solar Physics, 14, 2

Benz, A. O. 2017, Living Reviews in Solar Physics, 14, 2

Biskamp, D. 1986, Physics of Fluids, 29, 1520

Boerner, P., Edwards, C., Lemen, J., et al. 2012, *S*olar Phys., 275, 41

Brannon, S. R., Longcope, D. W., & Qiu, J. 2015, *A*strophys. J., 810, 4

Brooks, D. H., Warren, H. P., & Landi, E. 2021, *A*strophys. J. Lett., 915, L24

Brosius, J. W., & Daw, A. N. 2015, *A*strophys. J., 810, 45

Bruzek, A. 1964, *A*strophys. J., 140, 746

Cai, M. X., Portegies Zwart, S., Kouwenhoven, M. B. N., & Spurzem, R. 2019, *M*on. Not. Roy. Astron. Soc., 489, 4311

Carbone, V., Veltri, P., & Mangeney, A. 1990, Physics of Fluids A, 2, 1487

Carmichael, H. 1964, NASA Special Publication, 50, 451

Casini, R., & Judge, P. G. 1999, *A*strophys. J., 522, 524

Chandrasekhar, S. 1961, Hydrodynamic and hydromagnetic stability

Charvin, P. 1965, Annales d'Astrophysique, 28, 877

Chen, B., Bastian, T. S., Shen, C., et al. 2015, Science, 350, 1238

Chen, B., Yu, S., Reeves, K. K., & Gary, D. E. 2020, *A*strophys. J. Lett., 895, L50

Cheng, C. C., Oran, E. S., Doschek, G. A., Boris, J. P., & Mariska, J. T. 1983, *A*strophys. J., 265, 1090

Cheng, X., Li, Y., Wan, L. F., et al. 2018, *A*strophys. J., 866, 64

Chevalier, R. A., & Lambert, D. L. 1969, *S*olar Phys., 10, 115

Chitta, L. P., & Lazarian, A. 2020, *A*strophys. J. Lett., 890, L2

Collett, E. 2005, Field Guide to Polarization, Vol. FG05, doi:10.1117/3.626141

Culhane, J. L., Harra, L. K., James, A. M., et al. 2007, *S*olar Phys., 243, 19

Daughton, W., Roytershteyn, V., Karimabadi, H., et al. 2011, Nature Physics, 7, 539

De Pontieu, B., Title, A. M., Lemen, J. R., et al. 2014, *S*olar Phys., 289, 2733

Del Zanna, G. 2013, *A*stron. Astrophys., 555, A47

Del Zanna, G., Dere, K. P., Young, P. R., & Landi, E. 2021, *A*strophys. J., 909, 38

Del Zanna, G., & Mason, H. E. 2018, Living Reviews in Solar Physics, 15, 5

Dong, C., Wang, L., Huang, Y.-M., Comisso, L., & Bhattacharjee, A. 2018, *P*hys. Rev. Let., 121, 165101

Doschek, G. A., Cheng, C. C., Oran, E. S., Boris, J. P., & Mariska, J. T. 1983, *A*strophys. J., 265, 1103

Doschek, G. A., McKenzie, D. E., & Warren, H. P. 2014, *A*strophys. J., 788, 26

Dove, J. B., Gibson, S. E., Rachmeler, L. A., Tomczyk, S., & Judge, P. 2011, *A*strophys. J. Lett., 731, L1

Dudík, J., Polito, V., Janvier, M., et al. 2016, *A*strophys. J., 823, 41

Fejer, J. A. 1964, Physics of Fluids, 7, 499

Fleishman, G. D., Gary, D. E., Chen, B., et al. 2020, Science, 367, 278

Forbes, T. G., & Acton, L. W. 1996, *A*strophys. J., 459, 330

Forbes, T. G., & Lin, J. 2000, Journal of Atmospheric and Solar-Terrestrial Physics, 62, 1499

French, R. J., Judge, P. G., Matthews, S. A., & van Driel-Gesztelyi, L. 2019, *A*strophys. J. Lett., 887, L34

French, R. J., Matthews, S. A., Jonathan Rae, I., & Smith, A. W. 2021, *A*strophys. J., 922, 117

French, R. J., Matthews, S. A., van Driel-Gesztelyi, L., Long, D. M., & Judge, P. G. 2020, *A*strophys. J., 900, 192

Frisch, U., Sulem, P. L., & Nelkin, M. 1978, Journal of Fluid Mechanics, 87, 719

Furth, H. P., Killeen, J., & Rosenbluth, M. N. 1963, Physics of Fluids, 6, 459

Gabriel, A. H., & Mason, H. E. 1982, in Applied Atomic Collision Physics, Volume 1: Atmospheric Physics and Chemistry, Vol. 1, 345–397

Gary, G. A. 2001, *S*olar Phys., 203, 71

Gibson, S., Kucera, T., White, S., et al. 2016, Frontiers in Astronomy and Space Sciences, 3, 8

Gibson, S. E., Dalmasse, K., Rachmeler, L. A., et al. 2017, *A*strophys. J. Lett., 840, L13

Golub, L., Deluca, E., Austin, G., et al. 2007, *S*olar Phys., 243, 63

Gou, T., Liu, R., & Wang, Y. 2015, *S*olar Phys., 290, 2211

Graham, D. R., & Cauzzi, G. 2015, *A*strophys. J. Lett., 807, L22

Green, L. M., Török, T., Vršnak, B., Manchester, W., & Veronig, A. 2018, *S*pace Sci. Rev., 214, 46

Hannah, I. G., & Kontar, E. P. 2013, *A*stron. Astrophys., 553, A10

Harra, L. K., Matthews, S., Culhane, J. L., et al. 2013, *A*strophys. J., 774, 122

Hayes, L. A., Gallagher, P. T., Dennis, B. R., et al. 2019, *A*strophys. J., 875, 33

Henderson, M. G. 1994, PhD thesis, UNIVERSITY OF CALGARY (CANADA).

—. 2009, Annales Geophysicae, 27, 2129

Hinode Review Team, Al-Janabi, K., Antolin, P., et al. 2019, *P*ub. Astron. Soc. Japan, 71, R1

Hirayama, T. 1974, *S*olar Phys., 34, 323

Hones, E. W., J., Baker, D. N., Bame, S. J., et al. 1984, *G*eophys. Res. Lett., 11, 5

Janvier, M., Aulanier, G., Bommier, V., et al. 2014, *A*strophys. J., 788, 60

Janvier, M., Aulanier, G., Pariat, E., & Démoulin, P. 2013, *A*stron. Astrophys., 555, A77

Jeffrey, N. L. S., Fletcher, L., Labrosse, N., & Simões, P. J. A. 2018, Science Advances, 4, 2794

Jing, J., Xu, Y., Cao, W., et al. 2016, Scientific Reports, 6, 24319

Judge, P. G. 2007, *A*strophys. J., 662, 677

—. 2010, *A*strophys. J., 708, 1238

Judge, P. G., & Casini, R. 2001, in Astronomical Society of the Pacific Conference Series, Vol. 236, Advanced Solar Polarimetry – Theory, Observation, and Instrumentation, ed. M. Sigwarth, 503

Judge, P. G., Low, B. C., & Casini, R. 2006, *A*strophys. J., 651, 1229

Kahler, S. 1977, *A*strophys. J., 214, 891

Kalmoni, N. M. E., Rae, I. J., Watt, C. E. J., et al. 2015, Journal of Geophysical Research (Space Physics), 120, 8503

—. 2018, Nature Communications, 9, 4806

Karpen, J. T., Antiochos, S. K., & DeVore, C. R. 2012, *A*strophys. J., 760, 81

Kawate, T., Keenan, F. P., & Jess, D. B. 2016, *A*strophys. J., 826, 3

Kay, C., Gopalswamy, N., Xie, H., & Yashiro, S. 2017, *S*olar Phys., 292, 78

Kolmogorov, A. 1941, Akademiia Nauk SSSR Doklady, 30, 301

Kontar, E. P., Brown, J. C., Emslie, A. G., et al. 2011, *S*pace Sci. Rev., 159, 301

Kopp, R. A., & Pneuman, G. W. 1976, *S*olar Phys., 50, 85

Kowal, G., Falceta-Gonçalves, D. A., Lazarian, A., & Vishniac, E. T. 2020, *A*strophys. J., 892, 50

Kulsrud, R. M. 2011, Physics of Plasmas, 18, 111201

Kuridze, D., Mathioudakis, M., Morgan, H., et al. 2019, *A*strophys. J., 874, 126

Laitinen, T. V., Janhunen, P., Pulkkinen, T. I., Palmroth, M., & Koskinen, H. E. J. 2006, Annales Geophysicae, 24, 3059

Landi, E., Habbal, S. R., & Tomczyk, S. 2016, Journal of Geophysical Research (Space Physics), 121, 8237

Landi, E., Li, W., Brage, T., & Hutton, R. 2021, *A*strophys. J., 913, 1

Landi Degl'Innocenti, E., & Landolfi, M. 2004, 307, doi:10.1007/978-1-4020-2415-3

Lemen, J. R., Title, A. M., Akin, D. J., et al. 2012, *S*olar Phys., 275, 17

Li, Y., Xue, J. C., Ding, M. D., et al. 2018, *A*strophys. J. Lett., 853, L15

Lin, R. P., Dennis, B. R., Hurford, G. J., et al. 2002, *S*olar Phys., 210, 3

Litvinenko, Y. E. 1996, *A*strophys. J., 462, 997

Liu, R. 2013, *M*on. Not. Roy. Astron. Soc., 434, 1309

Long, D. M., Harra, L. K., Matthews, S. A., et al. 2018, *A*strophys. J., 855, 74

Longcope, D., Unverferth, J., Klein, C., McCarthy, M., & Priest, E. 2018, *A*strophys. J., 868, 148

Loureiro, N. F., Schekochihin, A. A., & Cowley, S. C. 2007, Physics of Plasmas, 14, 100703

Lyot, B. 1939, *M*on. Not. Roy. Astron. Soc., 99, 580

Masuda, S., Kosugi, T., Hara, H., Tsuneta, S., & Ogawara, Y. 1994, *N*ature, 371, 495

McPherron, R. L. 1970, *J*. Geophys. Res., 75, 5592

Melrose, D. B. 1997, *A*strophys. J., 486, 521

Michalke, A. 1964, Journal of Fluid Mechanics, 19, 543

Mihalas, D., & Winkler, K.-H. A. 1986, Radiation Hydrodynamics in Stars and Compact Objects, Vol. 255, doi:10.1007/3-540-16764-1

Morgan, H., & Druckmüller, M. 2014, *S*olar Phys., 289, 2945

Morosan, D. E., Carley, E. P., Hayes, L. A., et al. 2019, Nature Astronomy, 3, 452

Narukage, N., Sakao, T., Kano, R., et al. 2011, *S*olar Phys., 269, 169

Omodei, N., Pesce-Rollins, M., Longo, F., Allafort, A., & Krucker, S. 2018, *A*strophys. J. Lett., 865, L7

Orrall, F. Q., Rottman, G. J., Fisher, R. R., & Munro, R. H. 1990, *A*strophys. J., 349, 656

Parker, E. N. 1957, *J*. Geophys. Res., 62, 509

Peach, G. 1981, Advances in Physics, 30, 367

Petschek, H. E. 1964, Magnetic Field Annihilation, Vol. 50, 425

Pikelner, S. B., & Livshits, M. A. 1977, *S*oviet Astron., 21, 601

Polito, V., Dudík, J., Kašparová, J., et al. 2018a, *A*strophys. J., 864, 63

Polito, V., Galan, G., Reeves, K. K., & Musset, S. 2018b, *A*strophys. J., 865, 161

Polito, V., Reeves, K. K., Del Zanna, G., Golub, L., & Mason, H. E. 2015, *A*strophys. J., 803, 84

Pontin, D. I. 2011, Advances in Space Research, 47, 1508

Priest, E. R. 1985, Reports on Progress in Physics, 48, 955

Rae, I. J., Watt, C. E. J., Mann, I. R., et al. 2010, Journal of Geophysical Research (Space Physics), 115, A10222

Savage, S. L., McKenzie, D. E., Reeves, K. K., Forbes, T. G., & Longcope, D. W. 2010, *A*strophys. J., 722, 329

Schou, J., Scherrer, P. H., Bush, R. I., et al. 2012, *S*olar Phys., 275, 229

Seaton, D. B., Bartz, A. E., & Darnel, J. M. 2017, *A*strophys. J., 835, 139

Shaikh, D., & Zank, G. P. 2010, *M*on. Not. Roy. Astron. Soc., 402, 362

Shen, C., Kong, X., Guo, F., Raymond, J. C., & Chen, B. 2018, *A*strophys. J., 869, 116

Shibata, K., Masuda, S., Shimojo, M., et al. 1995, *A*strophys. J. Lett., 451, L83

Stanier, A., Daughton, W., Le, A., Li, X., & Bird, R. 2019, Physics of Plasmas, 26, 072121

Stark, J. 1914, Annalen der Physik, 348, 965

Sturrock, P. A. 1968, in Structure and Development of Solar Active Regions, ed. K. O. Kiepenheuer, Vol. 35, 471

Svestka, Z. 1989, *S*olar Phys., 121, 399

Sweet, P. A. 1958, in Electromagnetic Phenomena in Cosmical Physics, ed. B. Lehnert, Vol. 6, 123

Tenerani, A., & Velli, M. 2020, *M*on. Not. Roy. Astron. Soc., 491, 4267

Tomczyk, S., Card, G. L., Darnell, T., et al. 2008, *S*olar Phys., 247, 411

van Driel-Gesztelyi, L., & Green, L. M. 2015, Living Reviews in Solar Physics, 12, 1

van Driel-Gesztelyi, L., Wiik, J. E., Schmieder, B., et al. 1997, *S*olar Phys., 174, 151

Wang, H., & Liu, C. 2012, *A*strophys. J., 760, 101

Warren, H. P., Brooks, D. H., Ugarte-Urra, I., et al. 2018, *A*strophys. J., 854, 122

Warren, H. P., Ugarte-Urra, I., & Landi, E. 2014, *A*strophys. J. Suppl., 213, 11

Woods, M. M. 2019, PhD thesis, University College London, UK

Young, P. R., O'Dwyer, B., & Mason, H. E. 2012, *A*strophys. J., 744, 14

Young, P. R., Del Zanna, G., Mason, H. E., et al. 2007, *P*ub. Astron. Soc. Japan, 59, S857

Yu, S., Chen, B., Reeves, K. K., et al. 2020, *A*strophys. J., 900, 17